République Algérienne Démocratique et Populaire
Ministère de l'Enseignement Supérieur et de la Recherche Scientifique
المـــدرســـة الوطنيـــة العليـــا للأشغـال العموميـة
فرنســيس جانســون
École Nationale Supérieure des Travaux Publics
Francis Jeanson

Thesis

For the obtention of the State Engineer Diploma

Branch : Public Works
Specialty : Basic Infrastructures

T h e m e

Population Based Structural Health Monitoring Framework Using Optimal Sensor Placement And Pseudo-Transfer Learning

Presented by :
Mr. DAHEL Ihab

Supervised by :
Dr. LARBI H. Selma

Promotion 2025 / 2026

ACKNOWLEDGEMENTS

بسم الله الرحمن الرحيم

All praise and gratitude belong first and foremost to **Allah**, whose grace placed me among capable and generous people at every stage of this journey, and without whose guidance none of this work would have been possible.

My deepest gratitude goes to my **parents**, whose unwavering support, patience, and carefully chosen words have always pointed me toward a meaningful path. To my **sister**, who found the time to listen, across fields and disciplines, to everything I was building: your curiosity and encouragement meant more than you know.

I owe an immeasurable and deeply felt debt of gratitude to my supervisor, **Dr. Larbi Selma**, for whom words will always fall short. What she gave me goes far beyond this thesis. Over three years of working together on advanced research topics, every single day was more insightful than the one before: new ideas, new connections, new ways of seeing problems that I would simply not have found without her. She did not just supervise a project; she shaped the way I think. She opened doors, introduced me to people and possibilities well ahead of where I would have arrived on my own, and did all of this with a generosity of spirit and a genuine care that I have rarely encountered. Her belief in me, sustained across years and not just this final chapter, is something I will carry with profound gratitude for the rest of my career. I would not be here without her.

I am equally grateful, and deeply inspired, by **Dr. Raouf Bencherif**, whom Dr. Larbi graciously brought into this work. Dr. Bencherif is, to me, a true idol: a person whose career path, intellectual rigour, and ability to move fluently between foundational theory and real-world engineering practice represent exactly the kind of scientist and engineer I aspire to become. But what struck me most profoundly was something simpler and, in many ways, rarer: how genuinely accessible he makes himself. Here is a person at a remarkable stage of his career, with demands on his time that most of us cannot fully imagine, and yet he is the kind of person you can simply walk up to and talk to about science. Not just politely, but with real depth and real enthusiasm. Every conversation felt like a transmission: knowledge passed freely, from someone who has it, to someone who needs it, with no barrier in between. That kind of openness is not a given at any level of expertise; it is a deliberate choice, a reflection of character, and a model of what true teaching looks like. His insight sharpened this thesis considerably, and his example will stay with me far longer.

Sincere thanks are also due to the administrative and pedagogical staff of **ENSTP**, and in particular to the researchers and doctoral students of the **LTPiTE** laboratory, who welcomed us at any hour with open doors and open minds. A heartfelt thank you also goes to the administrative staff of the **DIB department**, who made so many things easier with patience and professionalism. I owe them a sincere apology for my absences during the training period at ENSTP. I can only say, with full honesty, that every one of those hours was invested in what I love most: research, reading, and working to connect concepts across different fields. That restlessness, that compulsion to keep exploring, is itself a gift from Dr. Larbi, and I hope the work produced in those hours speaks for itself.

What people like Dr. Larbi and Dr. Bencherif created around us was something rare and precious: a stress-free environment in which curiosity was never judged and learning had no ceiling. They gave us the freedom to love what we do deeply, and that love does not feel like something we chose so much as something that was cultivated in us by people who genuinely cared. That is what true teachers and true mentors do, and I cannot express it enough. Special thanks to **Prof. Lfekir**, whose conversations helped me develop a genuine sense of what research truly is: how to read across disciplines, how to connect ideas from different fields, and how to embrace an inherently multidisciplinary way of thinking. That orientation has become a part of how I see the world.

My warmest thanks go to my friends and classmates **Anissa** and **Ikram**. Sharing this journey with them has been one of its greatest gifts. Whether commuting together across the city to reach our supervisors, exchanging ideas late into the day, or simply being present for one another through the uncertainties of research, their friendship, dedication, and good spirit made every step lighter and more meaningful. I am truly grateful to have walked this path alongside them.

I close these acknowledgements not with a farewell but with a pledge. I am deeply grateful for this opportunity, and I do not take it lightly. I commit to continuing to work hard, to staying curious, and to carrying forward the spirit of generosity that **Dr. Larbi Selma** and **Dr. Raouf Bencherif** showed me so freely. They gave without expecting anything in return, and the least I can do is aspire, one day, to offer the same to someone who needs it as much as I did. That is how knowledge should travel: openly, generously, and from one passionate person to the next. This is only the beginning.

Abstract

Algeria's mass-housing programs use identical reinforced concrete buildings, making traditional Structural Health Monitoring (SHM) economically unfeasible. This thesis develops a Population-Based SHM (PBSHM) framework. A Ground+9-story ($G+9$) reference building (RPA 2024, BAEL 91/99) is analyzed. A Genetic Algorithm determines an Optimal Sensor Placement (OSP), identifying 20 sensors using the Modal Assurance Criterion (MAC) matrix. Inter-structure variations are modeled as Gaussian noise. A dual-branch Denoising Autoencoder (DAE) reconstructs sensor fields and predicts damage, achieving a coefficient of determination (R^2) >0.93 and Mean Squared Error (MSE) <0.02, validating scalable deployment.

Keywords: Population-Based SHM, Denoising Autoencoder, Optimal Sensor Placement (OSP), Modal Assurance Criterion (MAC), Flexibility-Based Damage Indicator, Coefficient of Determination (R^2), RPA 2024, Seismic Monitoring.

ملخص

تستخدم برامج الإسكان الجماعي في الجزائر مباني متطابقة من الخرسانة المسلحة، مما يجعل المراقبة الهيكلية (SHM) التقليدية غير مجدية اقتصادياً. تطور هذه الأطروحة إطاراً للمراقبة الهيكلية القائمة على مجتمع المباني (PBSHM). تم تحليل مبنى مرجعي مكون من طابق أرضي وتسعة طوابق ($G+9$) (RPA 2024، BAEL 91/99). يحدد خوارزمي جيني الوضع الأمثل للمستشعرات (OSP)، باختيار ٠٢ مستشعراً باستخدام معيار الضمان المودي (MAC). تُنمذج الفروق بين المباني كضوضاء غاوسية. يعيد مشفر تشويش ذاتي (DAE) بناء حقول القياسات ويتنبأ بالتلف، محققاً معامل تحديد (R^2) >0.93 ومتوسط خطأ تربيعي (MSE) <0.02، مما يؤكد قابليته للتطبيق واسع النطاق.

الكلمات المفتاحية: المراقبة الهيكلية السكانية (PBSHM)، مشفر التشويش (DAE)، الوضع الأمثل للمستشعرات (OSP)، معيار الضمان المودي (MAC)، مؤشر التلف بالمرونة، معامل التحديد (R^2)، RPA 2024، المراقبة الزلزالية.

Résumé

Les programmes de logements de masse en Algérie utilisent des bâtiments identiques en béton armé, rendant la Surveillance Santé Structurale (SHM) traditionnelle économiquement irréalisable. Cette thèse développe un cadre de SHM Basée sur la Population (PBSHM). Un bâtiment de référence Rez-de-chaussée+9 étages ($G+9$) (RPA 2024, BAEL 91/99) est analysé. Un Algorithme Génétique détermine un Placement Optimal des Capteurs (OSP), identifiant 20 capteurs via le Critère d'Assurance Modale (MAC). Les variations inter-structures sont modélisées comme un bruit gaussien. Un Auto-Encodeur Débruiteur (DAE) reconstruit les champs de capteurs et prédit les dommages, atteignant un coefficient de détermination (R^2) $>0,93$ et une Erreur Quadratique Moyenne (MSE) $<0,02$, validant un déploiement à grande échelle.

Mots-clés : Surveillance basée sur la population (PBSHM), Auto-encodeur débruiteur (DAE), Placement optimal de capteurs (OSP), Critère d'Assurance Modale (MAC), Indicateur de dom-

mage par flexibilité, Coefficient de détermination (R^2), RPA 2024, Surveillance sismique.

Contents

List of Figures

List of Tables

1 GENERAL INTRODUCTION

Algeria's northern coastline has long been one of the most densely inhabited and economically vital corridors in North Africa. The tell region, stretching along the Mediterranean from Annaba in the east to Oran in the west, concentrates the vast majority of the country's population, industrial activity, and critical infrastructure. At its heart lies the capital, Algiers, a metropolis of over five million inhabitants whose urban fabric has expanded relentlessly across the rugged terrain of the Mitidja plain and the surrounding Sahel hills. What makes this concentration particularly consequential is its geological setting. The northern Algerian seaboard sits directly above the convergent boundary between the African and Eurasian tectonic plates, a collision zone that has generated destructive earthquakes throughout recorded history. The devastating earthquake of El Asnam in 1980, which reached a magnitude of 7.3 and claimed more than 2,500 lives, and the catastrophic Boumerdes earthquake of May 2003, which struck at a magnitude of 6.8 and killed nearly 2,300 people while leaving hundreds of thousands homeless, are among the most painful reminders of this ongoing seismic hazard. These events, and the many moderate tremors that punctuate the region's history, make it clear that northern Algeria is not simply an area of elevated risk on a hazard map. It is a territory where the interaction between a dense, growing urban population and an active tectonic environment produces a challenge of the first order for engineers and public authorities alike.

It is precisely within this context that national housing programs such as AADL, LPP, and LPA have taken on an enormous practical importance. Faced with a chronic housing deficit and rapid population growth, the Algerian state has responded by constructing residential buildings on a massive scale, relying on industrialised, standardised typologies to achieve the necessary pace and volume. This approach, sometimes described informally as a "copy-paste" model, produces vast urban estates across the northern tell where a handful of proven structural designs are replicated across large plots of land, generating districts composed of hundreds of nominally identical reinforced concrete blocks (see Figure I.1). The efficiency of this strategy is undeniable from a construction standpoint, but it creates a situation that is structurally and organisationally unique: a built environment consisting of thousands of structurally similar buildings, all exposed to the same seismic hazard, and all potentially requiring rapid assessment in the aftermath of a major earthquake.

This mass standardisation brings with it a challenge that conventional structural monitoring approaches are simply not equipped to handle. Traditional Structural Health Monitoring (SHM) paradigms treat every building as an isolated, unique entity requiring a dedicated, densely instrumented sensor network calibrated specifically to that structure. This approach makes sense for a single landmark bridge or a critical industrial facility, but it becomes economically and logistically untenable when applied at the scale of a residential district. Instrumenting every building in a given estate with high-density sensor arrays would require investments of a magnitude that no public authority could justify. Yet the alternative, relying solely on post-earthquake visual inspections carried

(a) (b)

Figure I.1: Aerial views of typical Algerian mass-housing developments (e.g., AADL programs) **a)** during construction and **b)** upon completion. These dense, highly repetitive structural typologies constitute strongly homogeneous populations, necessitating scalable, fleet-level Structural Health Monitoring rather than isolated, building-specific diagnostics.

out building by building, is equally problematic. Following a major seismic event, the urgency of identifying which structures are safe, which require evacuation, and which are at immediate risk of collapse is extreme. Evaluating thousands of buildings sequentially in that context delays emergency responses, prolongs uncertainty, and costs lives. Decision-makers therefore need something that neither traditional SHM nor manual inspection can provide: a scalable framework capable of inferring the structural condition of an entire network of buildings from limited, efficiently distributed data.

Population-Based Structural Health Monitoring (PBSHM) offers a conceptually coherent answer to this need. Rather than treating each building as an isolated case, PBSHM frames the monitoring problem at the level of an entire population of structures that share common physical characteristics. Algerian mass housing estates are, in this sense, a near-ideal real-world instantiation of what the PBSHM literature refers to as a "strongly homogeneous population." The buildings within a given district are built from the same structural system, follow the same geometric layout, and respond to dynamic excitations according to the same underlying mechanical principles. They do, of course, differ from one another in subtle ways: minor variations in material properties arise from batch-to-batch differences in concrete and steel, construction tolerances introduce small geometric deviations, local soil conditions vary from one plot to the next, and environmental factors such as temperature and humidity affect each structure differently over time. The key insight of PBSHM is that these differences, rather than being a problem to be eliminated, can be explicitly modelled as statistical variability within the population. By learning the shared physical rules of the population, rather than calibrating separately to each individual building, diagnostic knowledge can then be transferred across the entire fleet.

Translating this conceptual framework into a practical monitoring system requires two concrete decisions: choosing a mathematical baseline that represents the population, and designing an instrumentation strategy that is both physically sound and financially realistic. The baseline adopted in this thesis is a standard $G+9$ reinforced concrete shear-wall building located in Staoueli, within the suburban belt of Algiers. This structure, representative of the typology deployed across AADL estates throughout the region, serves as the reference model from which the statistical properties of the broader population are derived. The variabilities that distinguish one building from another within such a population arise from many independent sources simultaneously, and their combined effect on the structure's dynamic characteristics can therefore be rigorously described as additive Gaussian noise, in accordance with the Central Limit Theorem. This statistical grounding transforms what might otherwise be treated as an uncontrolled source of uncertainty into a formally tractable modelling assumption.

Building on this foundation, the thesis proposes an integrated artificial intelligence pipeline designed to address both the instrumentation cost problem and the data quality challenge. On the instrumentation side, a Genetic Algorithm is used to identify a sparse but optimally distributed sensor network that preserves the maximum diagnostic information about the structure while using only a fraction of the sensors that a conventional dense array would require. On the data processing side, a Denoising Autoencoder (DAE) with a dual-branch architecture is trained to operate on the incomplete and noise-corrupted signals produced by these sparse sensors. The choice of a denoising autoencoder is not incidental. Its defining capability, the reconstruction of clean signals from corrupted or partial inputs, corresponds directly to the physical problem at hand: the inter-structure variability within the population manifests in the sensor data as additive noise, and the DAE is specifically structured to suppress that noise while retaining the damage-relevant information. In doing so, the network simultaneously reconstructs the full spatial sensor field across the structure and produces an accurate prediction of damage severity in the critical structural zones, all from a minimal and economically viable instrumentation setup.

The primary objective of this thesis is therefore to develop and validate a scalable, physically grounded, and noise-robust SHM pipeline tailored to the realities of standardised reinforced concrete residential buildings in high-density seismic zones. The remainder of this document is organised as follows. Section 2 provides a critical review of the literature, tracing the evolution from vibration-based monitoring to optimal sensor placement and Population-Based SHM. Section 3 details the structural design, numerical modelling, and dynamic analysis of the baseline $G+9$ building. Section 4 focuses on the design of the optimal sensor network and the extraction of flexibility-based damage features. Finally, Section 5 presents the architecture, training methodology, and validation results of the Denoising Autoencoder, demonstrating its capacity to transfer diagnostic knowledge across a simulated building population.

2 LITERATURE REVIEW

2.1 Introduction

The safety and longevity of civil infrastructure depend on our ability to detect and quantify structural damage before it leads to failure. Structural Health Monitoring (SHM) addresses this need by deploying sensor networks, acquiring structural responses, and applying inference algorithms to provide engineers with continuous information about structural integrity [1, 2].

This chapter traces the evolution of the field through four connected challenges that together motivate the approach adopted in the present thesis. Section 2.2 reviews the physical origins of SHM and the transition from visual inspection to vibration-based monitoring. Section 2.3 examines the flexibility matrix as the bridge that connects dynamic measurements back to physical stiffness reductions. Section 2.4 addresses the practical impossibility of instrumenting every degree of freedom and the Optimal Sensor Placement methods that resolve it. Finally, Section 2.5 confronts the scalability challenge of monitoring entire fleets of structures, introducing Population-Based SHM and transfer learning as the enabling framework for the present work.

2.2 The Physical Challenge: From Visual Inspection to Vibration-Based Monitoring

For most of the history of civil engineering, structural assessment relied on periodic visual inspections and localised non-destructive evaluation techniques such as ultrasonic testing, acoustic emission, and radiography [1]. While these methods provided useful diagnostic information, they were limited by human subjectivity, discontinuous temporal coverage, and an inability to assess the global state of a structure or detect internal degradation that is not visible from the surface.

The recognition of these limitations drove the development of vibration-based condition monitoring during the late 1980s and 1990s. The underlying physical principle is straightforward: the dynamic behaviour of any structure is governed by its mass, stiffness, and damping properties. When damage occurs, whether through cracking of concrete, corrosion of reinforcement, or delamination in composites, the result is a localised reduction in stiffness. This stiffness change, in turn, alters the structure's natural frequencies, mode shapes, and damping ratios [3, 4]. By measuring these modal parameters over time, engineers can in principle detect damage without direct physical access to the damaged region.

This idea led to a systematic way of thinking about what "damage detection" means. Rytter [3] proposed a four-level classification that has since become standard in the field: Level 1 asks whether damage exists (detection), Level 2 asks where it is located (localisation), Level 3 asks how severe it is (quantification), and Level 4 asks how much service life remains (prognosis). Each successive level requires richer data and more sophisticated inference, and much of the SHM literature can be understood as the effort to climb from one level to the next.

Early researchers focused on shifts in natural frequencies as the primary damage indicator. Frequencies are easy to measure and are sensitive to changes in global stiffness. However, for complex civil structures, frequency-based methods proved insufficient. Natural frequencies are global quantities: a small, localised stiffness reduction may shift a frequency by less than the measurement noise, and environmental factors such as temperature and traffic loading can produce frequency variations that are larger than the damage signal itself [3]. This meant that while vibration data clearly carried damage information, the raw modal parameters alone could not reliably tell an engineer where damage was located or how much stiffness had been lost. The field needed a derived quantity that could connect dynamic measurements directly back to physical stiffness, and this is precisely what the flexibility matrix provides.

2.3 The Interpretability Challenge: The Flexibility Matrix as a Bridge to Stiffness

The most natural quantity to examine for damage is the stiffness matrix itself, since structural damage manifests directly as a stiffness reduction. However, assembling the stiffness matrix from vibration measurements is notoriously difficult. The stiffness matrix is dominated by high-order, high-frequency modes that carry very little energy under ambient loading conditions, making their accurate extraction practically impossible [5, 6].

Pandey and Biswas [5] showed that this difficulty can be sidestepped by working with the flexibility matrix instead. The flexibility matrix is the mathematical inverse of the stiffness matrix, and it can be assembled from mode shapes and natural frequencies through the relation

$$\mathbf{F} = \Phi\Lambda^{-1}\Phi^{\mathsf{T}} = \sum_{r=1}^{m} \frac{1}{{}_r^{2}}\,\phi_r\phi_r^{\mathsf{T}}, \tag{II.1}$$

where $_r$ is the r-th circular natural frequency, ϕ_r is the corresponding mass-normalised mode shape vector, and m is the number of retained modes. The key property is the inverse-squared frequency weighting $_r^{-2}$: as the mode number increases, the natural frequency grows rapidly, so each successive mode contributes less and less to the sum. This means that the flexibility matrix converges quickly using only the first few low-frequency modes [5, 7, 8]. In other words, the flexibility matrix acts as a natural low-pass filter, amplifying the contribution of the low-frequency modes that are most reliably measured and suppressing the noisy high-frequency modes that are difficult to extract.

This convergence property is what makes the flexibility matrix practically useful. Operational Modal Analysis (OMA), which identifies modal parameters from ambient vibration alone (wind, traffic, micro-tremors) without requiring controlled excitation, delivers the natural frequencies and mode shapes needed to compute the flexibility matrix. Because OMA works best for low-frequency modes, and because the flexibility matrix needs only low-frequency modes, the two methods are naturally complementary [5, 9].

To detect damage, Pandey and Biswas proposed comparing the flexibility matrix of a potentially damaged structure against a healthy baseline:

$$\Delta\mathbf{F} = \mathbf{F}_{\text{damaged}} - \mathbf{F}_{\text{healthy}}. \tag{II.2}$$

They demonstrated that the columns of $\Delta\mathbf{F}$ show peaks at the degrees of freedom where stiffness has been reduced [5]. Because the flexibility matrix is the inverse of the stiffness matrix, a local stiffness reduction maps directly to a local increase in flexibility. This connection is physically transparent, which is a significant advantage over purely statistical indicators that may detect anomalies without explaining their mechanical origin.

Subsequent work extended and validated this approach in several directions. Altunisik et al. [4] compared modal flexibility against modal curvature as competing damage indicators on beam structures with multiple cracks, showing that flexibility-based methods provide more consistent localisation across different damage patterns. Li et al. [7] introduced a generalised flexibility matrix with an alternative weighting function that improves robustness when only very few modes are available, while still requiring the same OMA-compatible input data. Peng et al. [8] provided a comprehensive review of both static and dynamic flexibility approaches, confirming that flexibility-based indicators remain widely used despite the rise of data-driven methods.

The flexibility matrix thus provides the interpretability that raw modal parameters lack: it translates frequency and mode shape changes into stiffness changes that have direct physical meaning. However, there is a practical constraint that must be addressed before this approach can be deployed on real structures. Computing the flexibility matrix at a set of degrees of freedom requires mode shape measurements at those same degrees of freedom. For a finite element model of a real structure, the number of degrees of freedom can reach into the tens of thousands, and instrumenting every one of them with a sensor is economically and logistically impossible. This creates a hardware bottleneck that motivates the next topic.

2.4 The Hardware Bottleneck: Optimal Sensor Placement

A realistic SHM deployment must extract as much information as possible from a limited number of sensors. A large civil structure may have thousands of degrees of freedom in its finite element model, but practical budgets, physical access, weight constraints, and wiring limitations restrict the sensor count to tens or at most a few hundred. Choosing which degrees of freedom to instrument is therefore a critical design decision. A poor sensor layout can lead to spatial aliasing, where physically distinct mode shapes appear identical in the measurements, or to loss of sensitivity in regions where damage is most likely to occur [10].

This design problem is known as Optimal Sensor Placement (OSP). Given n candidate sensor locations and a budget of $m \ll n$ sensors, the objective is to select the subset of m locations that maximises the information content of the acquired data. The number of possible configurations grows combinatorially, making exhaustive search intractable for any realistic structure [11, 12].

To compare candidate sensor configurations, two objective functions have become standard in the literature. The first is derived from the Fisher Information Matrix (FIM), which quantifies how much information the measurements at a given sensor set carry about the unknown modal parameters. Maximising the determinant of the FIM, known as D-optimality, is equivalent to minimising the uncertainty in modal identification [10, 13]. The second is the Modal Assurance Criterion (MAC), which measures the geometric distinguishability between mode shapes as observed by the sensor set. An ideal sensor configuration produces a MAC matrix that is close to the identity, meaning that every target mode is linearly independent from every other mode at the measurement locations. When the off-diagonal MAC values are large, distinct modes become indistinguishable and the monitoring system loses spatial resolution [10, 14]. Many modern OSP formulations combine both criteria to ensure that the selected sensors are both informative for parameter estimation and capable of resolving individual modes [15].

Because the search space is combinatorial, Genetic Algorithms (GAs) have become one of the most widely used optimisation strategies for OSP. A sensor configuration is encoded as a chromosome, with each gene representing whether a sensor is placed at a given degree of freedom. An initial population of random configurations is evaluated against a fitness function, typically based on the MAC or FIM, and then evolved through selection, crossover, and mutation to produce increasingly better configurations [16, 17]. Liu et al. [16] proposed a decimal encoding scheme with forced mutation to prevent premature convergence in spatial lattice structures. Jung et al. [18] applied GA-based OSP to flexible aerospace structures, demonstrating effective placement using modal strain energy. Downey et al. [17] introduced an adaptive gene-pool learning mechanism that identifies Pareto-optimal trade-offs between sensor count and information content. Nasr et al. [19] compared GA-based approaches against simulated annealing for OSP, finding that GAs generally provided more consistent results across different structural configurations.

A practical limitation of most OSP formulations is that the number of sensors is treated as a fixed input. In reality, the sensor count is itself a design variable that should be optimised alongside placement. Cherid et al. [11] addressed this directly in the context of the Oued Dib cable-stayed bridge in Algeria. Starting from over 36,000 degrees of freedom in a 3D finite element model, they applied accessibility constraints and FIM-based pre-screening to reduce the candidate set to a manageable size, then ran a modified GA that could add or remove sensors during evolution. The algorithm converged to 47 optimally placed sensors, and the resulting network was shown to capture sufficient modal information for damage detection and localisation using an artificial neural network. This simultaneous optimisation of sensor number and placement serves as a direct reference for the approach adopted in the present thesis.

With optimally placed sensors providing reliable mode shape estimates at a reduced set of degrees of freedom, the flexibility matrix can be computed from sparse measurements, and the flexibility change $\Delta\mathbf{F}$ can serve as a damage-sensitive feature vector. The pipeline from vibration measurements through optimal sensing to physically interpretable features is now complete. The remaining challenge is classification: given a flexibility feature vector, the system must decide whether damage is present, where it is located, and how severe it is. For simple structures with a small number of damage scenarios, classical statistical methods can handle this task. But for complex structures with many possible damage locations and severity levels, the classification problem demands more powerful pattern recognition, which leads to machine learning and, ultimately, deep learning.

2.5 The Scalability Challenge: Machine Learning and Population-Based SHM

The integration of machine learning into SHM has followed the broader trajectory of the field: from classical methods such as support vector machines and artificial neural networks that operated on hand-crafted features, to deep learning architectures that can learn representations directly from raw or minimally processed data [1, 20, 2]. The specific choice of architecture depends on the nature of the problem being solved. Autoencoders, for instance, are designed to compress high-dimensional data onto a lower-dimensional latent manifold and reconstruct it, which makes them useful for anomaly detection: a model trained on healthy data produces large reconstruction errors when presented with damaged data [9]. Recurrent architectures address the challenge of temporal memory in time-series data, allowing models to capture how structural responses evolve over time. Denoising autoencoders go a step further by learning representations that are robust to input corruption, which makes them particularly suited to environments where sensor noise, signal dropout, and measurement uncertainty are significant [21]. This last property is directly relevant to the present thesis, where the monitoring system must operate reliably under noisy conditions and with potentially incomplete sensor coverage.

Regardless of the architecture, however, all supervised deep learning approaches share a fundamental requirement: they need large quantities of labelled training data. In SHM, labelled damage data means pairs of (measurement, known damage state), where the damage state includes the location and severity of any structural degradation. Obtaining such data is extremely difficult in practice [22, 23]. Deliberately damaging an operational structure to generate training examples is dangerous and economically unacceptable. Controlled laboratory experiments can provide some labelled data, but laboratory specimens rarely capture the full complexity of real structures. Finite element simulations offer a scalable alternative, but models inevitably contain simplifications that limit their fidelity. The result is that a deep learning model trained on data from one specific structure will typically fail to generalise to a different structure, or even to the same structure under different environmental or operational conditions.

This data scarcity problem is the central bottleneck that prevents deep learning from reaching its full potential in SHM. The response from the research community has been to move beyond the traditional paradigm of treating each structure as an isolated, unique entity.

Population-Based Structural Health Monitoring (PBSHM) addresses this bottleneck by considering groups of structures that share functional or geometric similarities, and by transferring diagnostic knowledge across members of the group. Importantly, the motivation for PBSHM extends beyond merely solving the data scarcity problem; it provides the strategic framework required to monitor entire fleets of infrastructure, such as wind farms, networks of bridges along commercial corridors, or large residential areas in seismic zones, at scale. The theoretical foundations for this approach have been developed in a series of papers by researchers at the University of Sheffield. Bull et al. [24] introduced the concept of *homogeneous populations*, which are collections of nominally identical structures such as a fleet of aircraft of the same type or a set of wind turbines from the same production line. Each real structure in the population is viewed as a "participant" that deviates slightly from an idealised mathematical "Form". These deviations arise from numerous independent sources: manufacturing tolerances, material property scatter, local soil conditions, and fluctuating environmental and operational variations such as temperature, humidity, and loading patterns. Because these sources are multiple, independent, and individually small, their combined effect on extracted dynamic features can be approximated as additive Gaussian noise through the Central Limit Theorem [24]. This is an important insight: it means that the population problem for a strongly homogeneous group of structures can be reduced to a Form plus some statistical deviations around it. In practical terms, it provides a theoretical justification for generating population-wide training data from a single baseline finite element model by adding stochastic perturbations that mimic the natural variability within the population.

For populations that are not homogeneous, the problem is more complex. Gosliga et al. [25] developed the mathematical machinery to handle *heterogeneous populations*, where structures differ in geometry, material, or configuration. They proposed decomposing structures into Irreducible Element (IE) models and representing the resulting topology as Attributed Graphs, where nodes correspond to joints and edges correspond to structural members. This graph-based representation enables the use of graph matching algorithms and Graph Neural Networks to quantify structural similarity even between radically different structures.

Part III of the series [26] addresses the core question of how to map functional data from a data-rich "source" structure to a data-poor "target" structure. It defines the mathematical formulations required for domain adaptation within heterogeneous feature spaces, showing that neural networks with joint domain adaptation can translate dynamic structural data across different domains. Part IV [27] conceptualises the global population of structures as existing in an abstract space, with feature data forming sections of a vector bundle over this space, providing a geometric framework for understanding when and why transfer should succeed. Part V [28] translates these ideas into a software ecosystem with a relational database, a network layer for maintaining similarity relationships, and a framework layer for executing transfer learning operations.

Transfer learning is the practical mechanism that makes PBSHM operational. When labelled data are abundant on a source structure but scarce on a target structure, transfer learning provides a way to reuse the knowledge encoded in a model trained on the source [22]. For homogeneous populations, simple fine-tuning is often sufficient: the lower layers of a pretrained network, which capture general structural features, are kept fixed while only the final layers are retrained with a small amount of target data [22, 29]. For heterogeneous populations, direct fine-tuning may fail because the source and target feature spaces are structurally incompatible, and domain adaptation techniques are needed to align the data distributions of the two domains [26, 30].

Several extensions have been proposed to make transfer learning more practical. Poole et al. [23] developed an active transfer learning framework that sequentially selects the most informative target-domain data points for labelling, minimising the cost of physical inspections while maximising predictive performance. Dardeno et al. [31] explored the use of intermediate structures as stepping stones for transfer when the source and target are too dissimilar for direct adaptation. In the aerospace domain, Brennan et al. [32] demonstrated that the PBSHM framework extends naturally to aircraft components, and Tsialiamanis et al. [33] validated graph neural network-based population inference on heterogeneous truss populations with varying material properties and environmental conditions.

The present thesis implements exactly this pipeline, with a specific focus on the intersection of PBSHM theory and machine learning architecture design. As established by the Central Limit Theorem for strongly homogeneous populations, the multitude of structural, environmental, and operational variabilities can be abstracted as additive Gaussian noise around a baseline Form. The core scientific contribution of this thesis is to explicitly link this population-level abstraction to the mechanics of a Denoising Autoencoder (DAE). Because the DAE is fundamentally designed to learn representations that are robust to input corruption, it does not merely filter out measurement noise; it effectively learns to ignore the structural and environmental deviations that define the population. By training the DAE on a baseline finite element model with carefully injected noise and dropout, the network achieves a form of "pseudo-transfer learning." The latent space learned during training on a fully instrumented source structure can therefore be directly reused for a target structure with sparser instrumentation, effectively transferring diagnostic knowledge within a homogeneous population without requiring classical domain adaptation.

2.6 Summary

The literature reviewed in this chapter follows a progression driven by successive practical limitations. Vibration-based methods overcame the subjectivity and spatial limitations of visual inspection, but raw modal parameters lacked the physical interpretability needed for damage localisation. The flexibility matrix resolved this by providing a direct, physically transparent link between dynamic measurements and stiffness reductions, one that converges with only a few low-frequency modes. However, computing the flexibility matrix at useful spatial resolution requires mode shape measurements at many degrees of freedom, which led to the development of optimal sensor placement methods that extract maximum information from a limited sensor budget. Even with good sensors and interpretable features, supervised machine learning models remain constrained by the scarcity of labelled damage data, which Population-Based SHM and transfer learning address by sharing diagnostic knowledge across populations of related structures.

Together, these four elements, the physical basis of vibration-based monitoring, the flexibility matrix as the damage indicator, optimal sensor placement as the measurement strategy, and population-based transfer learning as the inference framework, define the conceptual architecture of the present thesis. The chapters that follow develop each element computationally and apply them to a reinforced concrete building under the Algerian seismic context.

3 STRUCTURAL DESIGN AND SIZING

3.1 Project Description and General Views

Building upon the theoretical framework established in the preceding chapter, this structure was selected as the primary baseline for the analysis and development of our proposed methodology. The specimen is an G+9 reinforced concrete building located in Staoueli, Algiers, featuring a ground floor, a mezzanine level ("Entres-Sol"), and four basement levels. Geometrically, the building reaches a total elevation of 33.66 m from the foundation base to the roofline, utilizing a consistent story height of 3.06 m for all levels.

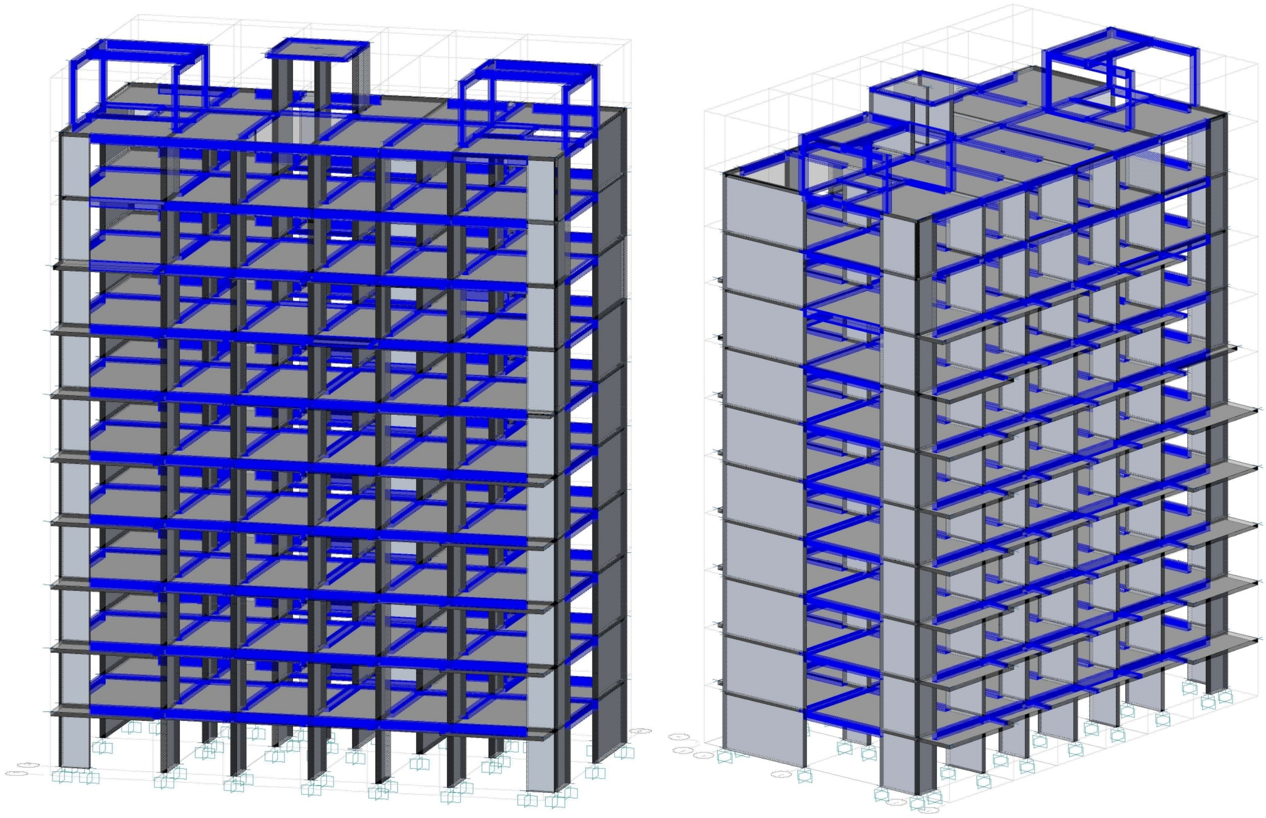

Figure III.1: 3D view of the chosen baseline structure from two different angles

The stability of the structure is primarily ensured by a system of reinforced concrete shear walls (voiles), which are strategically distributed to resist lateral seismic forces. Specifically, the plan layout features 2 lines of shear walls oriented along the X-direction and 7 lines distributed along the Y-direction. For the purposes of this study, the elastic sizing of the structural elements is performed exclusively for the superstructure; the mezzanine and basement levels were not considered within the scope of this work.

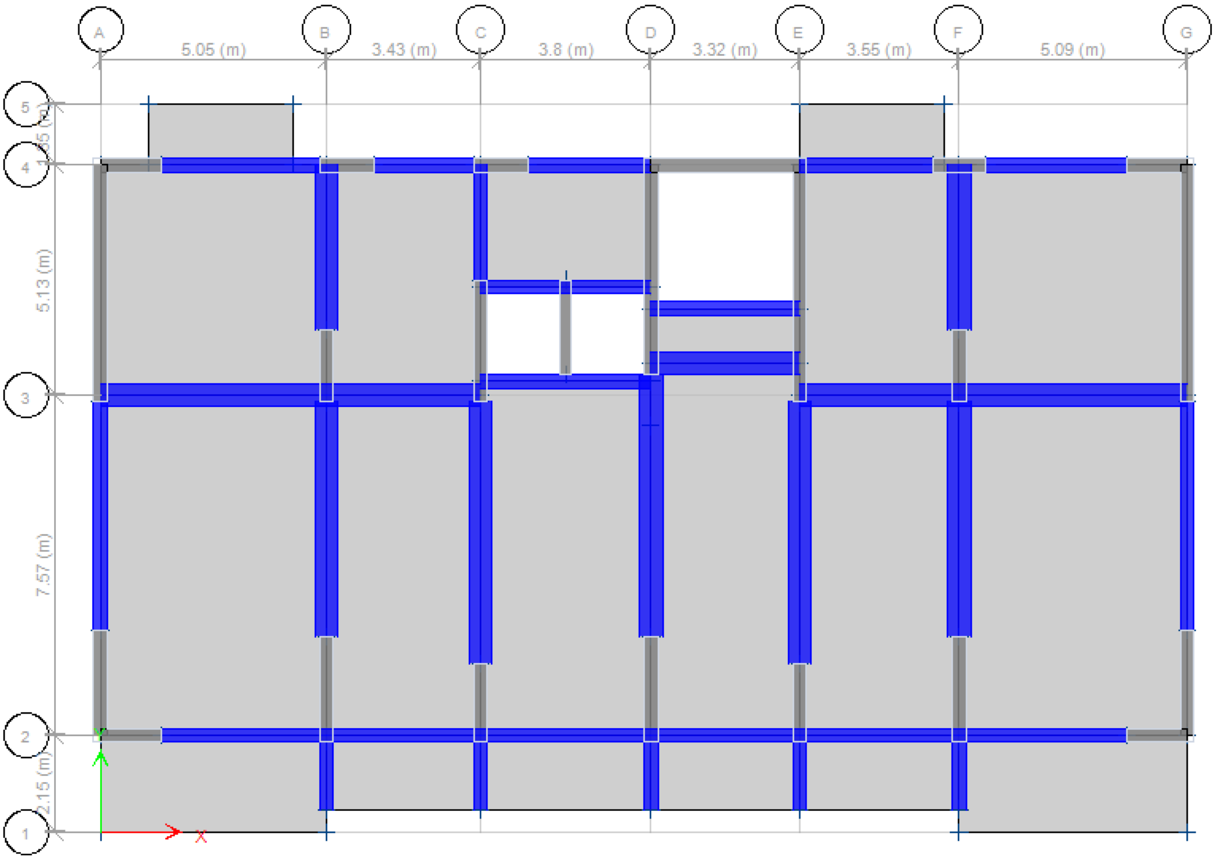

Figure III.2: Typical floor plan of the baseline structure

3.2 Materials Characteristics

To maintain a high level of structural performance for the baseline model, the following material properties were adopted in accordance with the project specifications.

3.2.1 Concrete (C30/37)

The concrete utilized is a class $C30/37$, characterized by the mechanical properties summarized in the table below:

Table III.1: Mechanical properties of C30/37 concrete.

Property	**Value**
Compressive strength at 28 days (f_{c28})	30 MPa
Modulus of Elasticity (E)	$33,000$ MPa
Poissonâ€™s Ratio (ν)	0.2
Specific Weight	25 kN/m^3
Shear Modulus (G)	$13,750$ MPa
Thermal Expansion Coefficient (α)	1.0×10^{-5} 1/°C

3.2.2 Steel Reinforcement (B500B)

High-adherence longitudinal and transverse reinforcement of nuance $B500B$ is employed, with the following design criteria:

Table III.2: Reinforcement characteristics and concrete cover.

Parameter	**Value**
Elastic Limit (f_e)	500 MPa
Concrete Cover - Foundations	5 cm
Concrete Cover - Columns and Beams	3 cm

3.3 Codes, Standards, and Software

The structural sizing and safety verifications follow the prevailing Algerian technical regulations and international standards:

- **RPA 2024**: Algerian Seismic Code for seismic demand evaluation and structural safety.
- **CBA 93**: Algerian code for the design and calculation of reinforced concrete structures.

- **BAEL 91 Revised 99**: Technical rules for the design of reinforced concrete structures based on limit state philosophy.
- **ETABS V22**: Integrated software for 3D structural analysis and design, used for modal and dynamic response spectrum analysis.

3.4 Load Analysis

The evaluation of the loads applied to the structure is a critical step in the elastic sizing process. For this analysis, the loads are classified into three main static load cases to be integrated into the ETABS model:

- **G0 (DEAD)**: This represents the self-weight of the structural elements (slabs, beams, columns, shear walls, and stair structural plates). It is calculated automatically by ETABS using the formula: Cross-Sectional Area $\times$ Length $\times$ $\gamma_{concrete}$, where the specific weight of reinforced concrete is taken as $\gamma_{concrete} = 25$ kN/m^3.
- **G1 (SUPER DEAD)**: This includes all superimposed dead loads, such as floor finishes, screed, masonry walls, and insulation. The structural self-weight is explicitly excluded from these manual calculations.
- **Q (LIVE)**: This represents the live loads depending on the usage of the specific area (residential, commercial, or accessible/inaccessible roofs).

3.4.1 Superimposed Dead Loads - G1 (SUPER DEAD)

The superimposed dead loads for the different levels and structural components are detailed in the tables below (see Tables III.3, III.4, III.5, and III.6).

Table III.3: Superimposed dead loads for the current residential floors.

Current Floor (Residential)	
Component	**Load (kN/m²)**
Cement mortar screed ($t = 4$ cm)	0.80
Ceramic tile coating ($t = 2$ cm)	0.70
Partition walls	1.00
Plaster ceiling coating	0.20
Total G1	**2.70**

Table III.4: Superimposed dead loads for the inaccessible terrace.

Inaccessible Terrace	
Component	**Load (kN/m²)**
Gravel protection ($t = 5$ cm)	1.00
Multilayer waterproofing complex	0.12
Sloping layer (average thickness 10 cm)	2.20
Expanded polystyrene thermal insulation ($t = 4$ cm)	0.16
Vapor barrier	0.02
Plaster ceiling coating	0.20
Total G1	**3.70**

Table III.5: Superimposed dead loads for the stair flights and landings.

Stairs - Flight	
Component	**Load (kN/m²)**
Concrete step	2.12
Porcelain stoneware + laying mortar (horizontal), $t = 9$ mm	0.60
Porcelain stoneware + laying mortar (vertical), $t = 9$ mm	0.60
Cement coating ($t = 1.5$ cm)	0.27
Total G1	**3.59**
Stairs - Landing	
Porcelain stoneware + laying mortar (horizontal), $t = 9$ mm	0.60
Laying mortar ($t = 2$ cm)	0.40
Cement coating ($t = 1.5$ cm)	0.27
Total G1	**1.27**

Table III.6: Superimposed dead loads for the exterior masonry walls.

Exterior Masonry Walls (Double Wall)	
Component	**Load (kN/m²)**
Sprayed interior plaster coating ($t = 2$ cm)	0.36
Hollow brick ($t = 10$ cm)	0.90
Polystyrene ($t = 4$ cm)	0.00
Hollow brick ($t = 10$ cm)	0.90
Exterior cement coating ($t = 2$ cm)	0.20
Total G1	**2.36**

For the reinforced concrete parapet (acroterion) at the terrace level, a linear load of 1.75 **kN/ml** is applied.

3.4.2 Live Loads - Q (LIVE)

The live loads are determined according to the building's destination and the functional requirements of each space, as summarised in Table III.7:

Table III.7: Live loads assigned to various areas of the structure.

Usage / Space	**Load Q (kN/m²)**
Current Floor - Residential	1.50
Current Floor - Commercial	5.00
Common Areas and Stairs	2.50
Inaccessible Terrace	1.00

3.5 Seismic Analysis

3.5.1 Selection of the calculation method

For the seismic analysis of the present G+9 reinforced concrete building, the **Modal Response Spectrum Analysis**, as prescribed in (§ 4.3) of RPA 2024, has been selected for the following reasons:

- **Regulatory Applicability :** Unlike the Equivalent Static Method (§4.2), which is restricted to regular configurations, the Modal Response Spectrum Analysis is applicable to all building types and is systematically retained for this study given the building's characteristics
- **Building Height and Seismic Zone :** With a total height of 33.66 m, higher vibration modes beyond the fundamental are expected to contribute to the seismic response. The modal analysis explicitly captures these contributions by requiring sufficient modes to achieve at least 90% mass participation (§4.3.3)

3.5.2 Modal Analysis and Mass Participation

The modal analysis of the structure yielded the natural periods, mode shapes, and mass participation ratios presented in Table III.8. A total of 11 modes were extracted to capture the dynamic behavior of the building.

Table III.8: Modal analysis results: periods and mass participation factors

Mode	Period (sec)	Translational		Cumulative		Rotational	
		U_X	U_Y	$\sum U_X$	$\sum U_Y$	R_Z	$\sum R_Z$
1	0.849	**0.6559**	0.0003	**0.6559**	0.0003	0.0691	0.0691
2	0.643	0.0017	**0.6603**	0.6576	**0.6606**	0.0045	0.0736
3	0.468	0.0809	0.0052	0.7385	0.6658	**0.5980**	0.6716
4	0.241	0.1312	0.0000	0.8697	0.6658	0.0171	0.6887
5	0.140	0.0121	0.0916	0.8818	0.7574	0.0004	0.6891
6	0.138	0.0058	0.0975	0.8876	0.8549	0.0035	0.6926
7	0.119	0.0177	0.0029	**0.9053**	0.8578	0.1048	0.7974
8	0.110	0.0315	0.0000	0.9368	0.8578	0.0125	0.8099
9	0.096	0.0009	0.0023	0.9377	0.8602	0.0639	0.8738
10	0.072	0.0258	0.0000	0.9634	0.8602	0.0004	0.8742
11	0.061	0.0000	0.0590	0.9634	**0.9192**	0.0026	0.8768
Note: Bold values indicate dominant participation per mode and cumulative masses meeting the 90% requirement.							

Fundamental period. The fundamental period is $T_1 = 0.849$ s (Mode 1, predominantly U_X with 65.59% participation). Mode 2 ($T_2 = 0.643$ s) is predominantly U_Y (66.03%), and Mode 3 ($T_3 = 0.468$ s) is predominantly torsional R_Z (59.80%).

Mass participation. Per §4.3.3 of RPA 2024, cumulative mass participation reaches 90.53% in U_X at Mode 7 and 91.92% in U_Y at Mode 11, satisfying the 90% requirement in both translational directions.

Mode shapes. Modes 1–3 dominate the response: U_X-dominant (Mode 1), U_Y-dominant (Mode 2), and R_Z-dominant (Mode 3). Higher modes (4–11) exhibit coupled behavior contributing to the remaining mass.

Compliance. The analysis satisfies all criteria of §4.3.3: 90% mass participation achieved in both horizontal directions, minimum 3 modes per direction exceeded, and all modes with $> 5\%$ participation included.

3.5.3 Structural Classification According to RPA 2024

The seismic classification of the studied structure is carried out in accordance with the provisions of RPA 2024. This classification aims to determine the structural regularity of the building and to identify the type of seismic resisting system.

The classification process is performed through three main stages. First, the structural parameters required for the verification are determined from the numerical model of the building. Second, the regularity of the structure is examined both in plan and in elevation according to the criteria defined by the seismic code. Finally, the structural system responsible for resisting horizontal seismic forces is identified.

Determination of Structural Parameters The prescribed verifications requires the determination of several global parameters describing the lateral behavior of the structure. These parameters include the Torsion radii r_x, r_y and the Massive radius of gyration in plan l_s as well as the story masses and stiffnesses. They are derived from displacements and rotations in the major axes from the analysis of the threeâ€“dimensional numerical model subjected to controlled lateral loading.

for each story i, the numerical model provides the horizontal displacements of the center of mass in the two principal directions of the structure, denoted respectively by $\mathbf{u_{x,G,i}}$ and $\mathbf{u_{y,G,i}}$. In addition, the analysis yields the rotational components of the floor about the three orthogonal axes, denoted by $\theta_{x,i}$, $\theta_{y,i}$ and $\theta_{z,i}$. The rotations $\theta_{x,i}$ and $\theta_{y,i}$ correspond to the rotations of the floor about the horizontal axes, while $\theta_{z,i}$ represents the torsional rotation of the floor about the vertical axis.

These quantities describe the global deformation state of the structure when subjected to horizontal loading. And they are completed by the story seismic masses M_i. These masses account for the weight due to permanent loads and that of any fixed equipment, combined with 30% of the applied live loads [34].

The structural response presented above is obtained by applying a lateral load distribution proportional to the story masses of the structure. The underlying principle of this method is based on the relationship between inertial forces and ground acceleration during seismic excitation [35, 36]. For a multi-degree-of-freedom structural system subjected to a horizontal ground acceleration a_g, the equation of motion takes the form

$$\mathbf{M}\ddot{\mathbf{u}} + \mathbf{C}\dot{\mathbf{u}} + \mathbf{K}\mathbf{u} = -\mathbf{M}\mathbf{r}\, a_g(t)$$

where $\mathbf{M}$, $\mathbf{C}$, and $\mathbf{K}$ are the mass, damping, and stiffness matrices respectively, and $\mathbf{r}$ is the influence vector [35]. When a structure is subjected to a horizontal ground acceleration a, the inertial force acting on the mass of story i can be expressed as

$$F = M_i \cdot a$$

where M_i is the seismic mass associated with the considered story.

In order to obtain a loading pattern independent of the actual seismic intensity, a unit ground acceleration is assumed:

$$a = 1\ m \cdot s^{-2}$$

the inertia forces become,

$$F = M_i$$

Thus, the resulting load pattern corresponds to a system of horizontal forces at each floor level that are numerically equal to the story masses. This loading configuration represents the static deformation of the structure under the inertia forces generated by a rigid-body ground acceleration of unit magnitude. Because the acceleration is uniform over the height of the building, the resulting displacement field reflects only the stiffness distribution of the structural system [35, 36].

The static analysis performed under the unit acceleration load pattern provides the displacement and rotation of the center of mass of each floor together with the corresponding story masses. The results are summarized in Table III.9

Table III.9: Structural response to unit acceleration loading

Story	X Direction		Y Direction		Torsion	Mass Properties	
	$\mathbf{u_{x,G,i}}$ (mm)	$\theta_{x,i}$ (rad)	$\mathbf{u_{y,G,i}}$ (mm)	$\theta_{y,i}$ (rad)	$\theta_{z,i}$ (rad)	**Mass (kg)**	$\mathbf{I_{O,i}(t/m^2)}$
10	18747.205	0.555565	11986.896	-0.071350	0.107241	350159	23102
9	17418.508	0.503085	10587.098	-0.064464	0.095535	364111	26740
8	15987.330	0.447503	9166.346	-0.057132	0.083440	400433	29961
7	14187.764	0.387865	7710.728	-0.049264	0.070948	402608	30284
6	12181.982	0.324154	6241.767	-0.040879	0.058156	406334	30791
5	9998.111	0.257352	4795.953	-0.032160	0.045308	412036	31635
4	7641.213	0.189480	3421.698	-0.023429	0.032786	415752	31788
3	5273.097	0.123731	2171.374	-0.015126	0.021140	412036	31635
2	3001.546	0.065027	1117.703	-0.007851	0.011102	412036	31635
1	1070.058	0.020396	351.684	-0.002411	0.003620	412036	31635

Note: The table reports the horizontal displacements of the centres of mass and the rotational components of each floor obtained from the unit acceleration loading case. These values are subsequently used to compute interstorey deformations, storey stiffness, torsional eccentricities, and torsional radii required for the structural regularity verification.

Once the structural response to the unit acceleration load pattern has been obtained, the inter-story deformations are computed for each floor i as the difference between the displacement and rotation of floor i and the floor immediately below $(i-1)$ [35]:

$$\Delta \mathbf{u}_{x,G,i} = \mathbf{u}_{x,G,i} - \mathbf{u}_{x,G,i-1}, \qquad \Delta \mathbf{u}_{y,G,i} = \mathbf{u}_{y,G,i} - \mathbf{u}_{y,G,i-1}$$

$$\Delta \theta_{x,i} = \theta_{x,i} - \theta_{x,i-1}, \qquad \Delta \theta_{y,i} = \theta_{y,i} - \theta_{y,i-1}$$

$$\Delta \theta_{z,i} = \theta_{z,i} - \theta_{z,i-1}$$

The natural eccentricity components $e_{0x,i}$ and $e_{0y,i}$ are then derived from the relative translation and rotation of the floors [35, 37]:

$$e_{0x,i} = \frac{\Delta \mathbf{u}_{y,G,i}}{\Delta \theta_{z,i}}, \quad e_{0y,i} = \frac{\Delta \mathbf{u}_{x,G,i}}{\Delta \theta_{z,i}}$$

These quantities represent the horizontal distance between the center of mass of floor i and the projection of the stiffness center from the floor below. They quantify the inherent torsional offset of the story. Under the rigid diaphragm assumption, each floor possesses three degrees of freedom (two translations and one rotation about the vertical axis) and translational motion is coupled with torsional rotation through this eccentricity [35].

The radius of gyration of the floor mass, denoted l_s, is obtained from the mass distribution of the story. It is defined as [35]

$$l_s = \sqrt{\frac{\mathbf{I_{O,i}}}{M_i}}$$

Where $\mathbf{I_{O,i}}$ is the mass moment of inertia of floor i with respect to the vertical axis.

Next, the displacement of the stiffness center $\Delta \mathbf{u}_{x,C,i}$ and $\Delta \mathbf{u}_{y,C,i}$ are computed by removing the torsional contribution due to the natural eccentricity from the measured inter-story translations [37]:

$$\Delta \mathbf{u}_{x,C,i} = \Delta \mathbf{u}_{x,G,i} - e_{0y,i} \cdot \Delta \theta_{z,i}$$

$$\Delta \mathbf{u}_{y,C,i} = \Delta \mathbf{u}_{y,G,i} - e_{0x,i} \cdot \Delta \theta_{z,i}$$

Finally, the torsional radii in the two principal directions are given by [34, 35]

$$r_{x,i} = \sqrt{\frac{\Delta \mathbf{u}_{y,C,i}}{\Delta \theta_{z,i}}}, \quad r_{y,i} = \sqrt{\frac{\Delta \mathbf{u}_{x,C,i}}{\Delta \theta_{z,i}}}$$

The resulting inter-story deformations, natural eccentricities, stiffness-center displacements, and torsional radii obtained from the analysis are summarized in Tables III.10 and III.11.

Table III.10: Interstorey deformation components obtained from the unit acceleration analysis

Floor	X Direction		Y Direction		Torsion
	$\Delta \mathbf{u}_{\mathbf{x},\mathbf{C},\mathbf{i}}$ (mm)	$\Delta\theta_{x,i}$ (rad)	$\Delta \mathbf{u}_{\mathbf{y},\mathbf{C},\mathbf{i}}$ (mm)	$\Delta\theta_{y,i}$ (rad)	$\Delta\theta_{z,i}$ (rad)
10	1328.697	0.052480	1399.798	-0.006886	0.011706
9	1431.178	0.055582	1420.752	-0.007332	0.012095
8	1799.566	0.059638	1455.618	-0.007868	0.012492
7	2005.782	0.063711	1468.961	-0.008385	0.012792
6	2183.871	0.066802	1445.814	-0.008719	0.012848
5	2356.898	0.067872	1374.255	-0.008731	0.012522
4	2368.116	0.065749	1250.324	-0.008303	0.011646
3	2271.551	0.058704	1053.671	-0.007275	0.010038
2	1931.488	0.044631	766.019	-0.005440	0.007482
1	1070.058	0.020396	351.684	-0.002411	0.003620

Note: Interstorey translational and rotational deformations obtained from the unit acceleration analysis. These values correspond to the relative displacement and rotation between two consecutive floors and constitute the basis for the evaluation of the torsional parameters of the structure.

Table III.11: Derived torsional parameters of the structure

Floor	$\mathbf{L_s}$ (m)	Natural Eccentricity		Stiffness Centre		Torsional Radii	
		$\mathbf{e}_{\mathbf{0x},\mathbf{i}}$ (m)	$\mathbf{e}_{\mathbf{0y},\mathbf{i}}$ (m)	$\Delta \mathbf{u}_{\mathbf{x},\mathbf{C},\mathbf{i}}$ (mm)	$\Delta \mathbf{u}_{\mathbf{y},\mathbf{C},\mathbf{i}}$ (mm)	$\mathbf{r}_{\mathbf{x},\mathbf{i}}$ (m)	$\mathbf{r}_{\mathbf{y},\mathbf{i}}$ (m)
10	8.123	0.588	4.483	1328.462	1399.794	10.94	10.65
9	8.570	0.606	4.595	1430.923	1420.748	10.84	10.88
8	8.650	0.630	4.774	1799.281	1455.613	10.79	12.00
7	8.673	0.655	4.981	2005.465	1468.956	10.72	12.52
6	8.705	0.679	5.199	2183.524	1445.808	10.61	13.04
5	8.762	0.697	5.420	2356.530	1374.249	10.48	13.72
4	8.744	0.713	5.646	2367.745	1250.318	10.36	14.26
3	8.762	0.725	5.848	2271.208	1053.666	10.25	15.04
2	8.762	0.727	5.965	1931.222	766.015	10.12	16.07
1	8.762	0.666	5.634	1069.943	351.682	9.86	17.19

Note: The table summarizes the torsional parameters derived from the deformation field of the structure. The radius of gyration L_s is obtained from the mass properties of each floor, while the natural eccentricities and torsional radii are determined from the relationship between interstorey translations and torsional rotations. These parameters are required for the verification of torsional regularity according to the seismic design provisions.

Classification of the Building According to its Configuration The structural configuration of the building is examined in accordance with the regularity criteria defined by RPA 2024, both in plan and in elevation. The purpose of this classification is to determine whether the structure qualifies as regular or irregular, which directly affects the applicable analysis method and the value of the behavior coefficient.

Plan Regularity The plan regularity of the building is assessed against four criteria (**a1–a4**) prescribed by RPA 2024 [34].

Criterion a1 – Symmetry of mass and stiffness distribution. As evidenced by the floor plan shown in Figure III.2, the building does not present a sensibly symmetric layout with respect to either principal axis, neither in the distribution of masses nor in the distribution of lateral stiffness. Criterion **a1** is therefore **not observed**.

Criterion a2 – Eccentricity between the centre of mass and the centre of rigidity. According to Commentaire 5 of RPA 2024 [34], for a shear-wall bracing system to be considered regular in plan, the structural eccentricities e_{0x} and e_{0y} must satisfy simultaneously at every level:

$$\begin{cases} e_{0x} \leq 0.30\,r_x \\ r_x \geq l_s \end{cases} \qquad \text{and} \qquad \begin{cases} e_{0y} \leq 0.30\,r_y \\ r_y \geq l_s \end{cases}$$

The verification ratios derived from the torsional parameters computed in Table III.11 are summarized in Table III.12.

Table III.12: Verification of plan regularity criterion a2 – eccentricity ratios per floor

Floor	$\mathbf{e_{0x,i}/0.30\,r_{x,i}}$	$\mathbf{e_{0y,i}/0.30\,r_{y,i}}$	$\mathbf{l_{s,i}/r_{x,i}}$	$\mathbf{l_{s,i}/r_{y,i}}$
10	0.18	**1.40**	0.743	0.762
9	0.19	**1.41**	0.791	0.788
8	0.19	**1.33**	0.801	0.721
7	0.20	**1.33**	0.809	0.693
6	0.21	**1.33**	0.821	0.668
5	0.22	**1.32**	0.836	0.639
4	0.23	**1.32**	0.844	0.613
3	0.24	**1.30**	0.855	0.583
2	0.24	**1.24**	0.866	0.545
1	0.23	**1.09**	0.889	0.510

The ratio $e_{0y,i}/0.30\,r_{y,i}$ exceeds unity at every floor level, meaning the condition $e_{0y} \leq 0.30\,r_y$ is never satisfied. Criterion **a2** is therefore **not observed**.

Criterion a3 – Compactness of the floor plan. The principal plan dimensions of the building are:

$$L_x = 24.24 \text{ m}, \qquad L_y = 16.20 \text{ m}$$

The aspect ratio satisfies:

$$0.25 \leq \frac{L_x}{L_y} = \frac{24.24}{16.20} = 1.50 \leq 4$$

The floor plan presents no significant re-entrant corners or projections exceeding 25% of the total building dimension in either direction. Criterion **a3** is therefore **observed** (see Figure III.3).

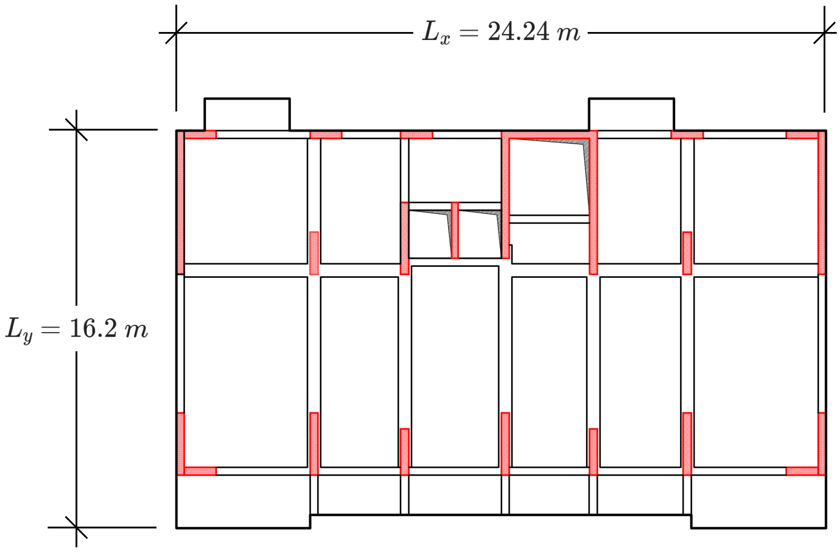

Figure III.3: Floor plan dimensions used for criterion a3 verification

Criterion a4 – In-plane rigidity of floor diaphragms. The opening areas measured on the structural drawings are:

$$\text{Total floor area} = 361.58\ \text{m}^2$$
$$\text{Opening area (typical stories)} = 18.64\ \text{m}^2$$
$$\text{Opening area (terrace level)} = 23.96\ \text{m}^2$$

The governing ratio is:

$$\frac{\text{Opening area}}{\text{Total area}} \times 100 = \frac{23.96}{361.58} \times 100 = 6.62\% < 15\%$$

Criterion **a4** is therefore **observed**.

The plan regularity assessment is summarised in Table III.13.

Table III.13: Summary of plan regularity criteria

Crit.	Condition	Status
a1	Sensible symmetry of mass and stiffness distribution	**Not Observed**
a2	Eccentricity $e_0 \leq 0.30\,r$ and $r \geq l_s$ at every floor	**Not Observed**
a3	Aspect ratio $L_x/L_y \leq 4$; no projections $> 25\%$	**Observed**
a4	Floor openings $< 15\%$ of total floor area	**Observed**
Conclusion		**NOT Regular**

Since criteria **a1** and **a2** are not satisfied, the building is classified as **plan irregular** according to RPA 2024 [34].

Elevation Regularity The elevation regularity of the building is assessed against four criteria (**b1–b4**) prescribed by RPA 2024 [34].

Criterion b1 – Continuity of vertical load-bearing elements. All shear walls are continuous from the foundation to the roof without interruption. Criterion **b1** is therefore **observed**.

Criterion b2 – Progressive variation of stiffness and mass. The normalized stiffness and mass profiles along the building height are plotted in Figure III.4. Both profiles decrease monotonically from the base to the top without abrupt discontinuities. Criterion **b2** is therefore **observed**.

Criterion b3 – Mass-to-stiffness ratio between successive stories. The condition to be satisfied at every pair of successive stories is:

$$0.75 \leq \left| \frac{(M/K)_i}{(M/K)_{i-1}} \right| \leq 1.25$$

where M is the seismic mass of the given story and K is its lateral stiffness, estimated directly from the numerical model as the ratio of the story shear force to its corresponding inter-story drift:

$$K_i = \frac{V_i}{\Delta_i}$$

The computed mass-to-stiffness ratios are presented in Table III.14.

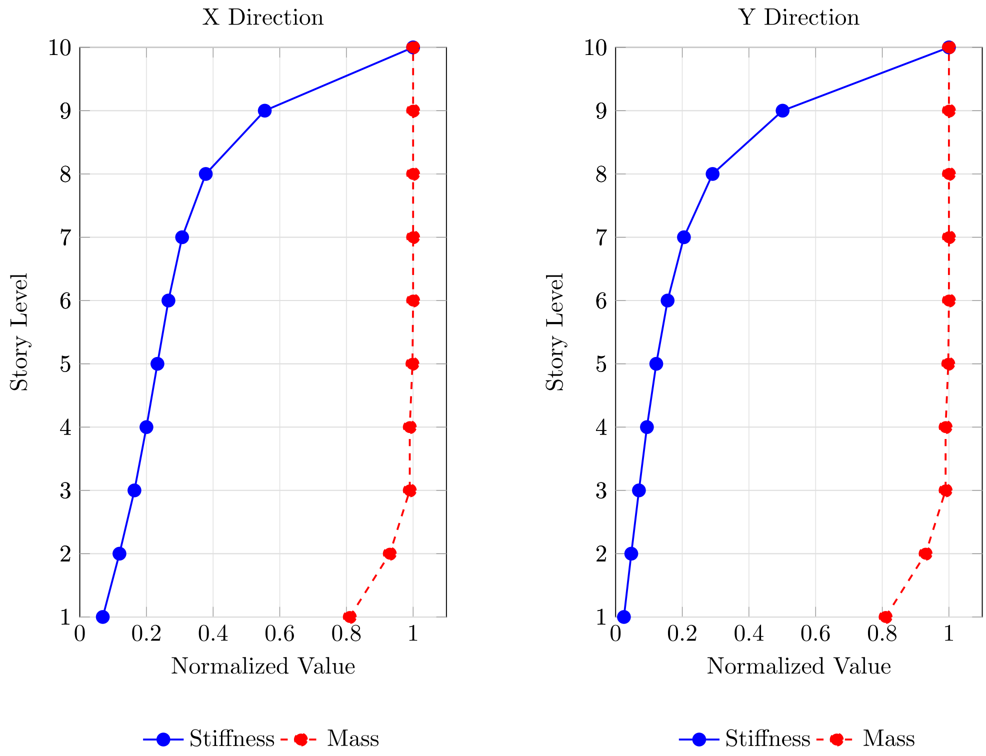

Figure III.4: Normalized stiffness and mass profiles along the building height

Table III.14: Verification of elevation regularity criterion b3 – mass-to-stiffness ratios between successive stories

Floor	M/K X	M/K Y	Ratio X	Ratio Y
10	1.30	1.21	**1.65**	**1.78**
9	0.79	0.68	**1.25**	**1.36**
8	0.63	0.50	1.21	**1.35**
7	0.52	0.37	1.16	**1.28**
6	0.45	0.29	1.12	**1.26**
5	0.40	0.23	1.14	**1.35**
4	0.35	0.17	**1.25**	**1.42**
3	0.28	0.12	**1.47**	**1.71**
2	0.19	0.07	**1.73**	**1.75**

Note: Values outside the interval [0.75, 1.25] indicate violation of criterion b3. All story pairs exceed the 1.25 upper bound in at least one direction.

The ratio exceeds the admissible upper bound of 1.25 in both directions at most floor levels. Criterion **b3** is therefore **not observed**.

Criterion b4 – Setbacks in elevation. The building has no setbacks in elevation; all floors share the same plan outline from the ground level to the rooftop. Criterion **b4** is therefore **observed**.

The elevation regularity assessment is summarized in Table III.15.

Table III.15: Summary of elevation regularity criteria

Crit.	Condition	Status
b1	Continuity of all vertical bracing elements to the foundation	**Observed**
b2	Monotonic decrease of stiffness and mass from base to top	**Observed**
b3	M/K ratio between successive stories within $\pm 25\%$	**Not Observed**
b4	No abrupt setbacks; plan dimensions vary $\leq 20\%$ per story	**Observed**
Conclusion		**NOT Regular**

Since criterion **b3** is not satisfied, the building is classified as **elevation irregular** according to RPA 2024 [34].

Identification of the Lateral Force-Resisting System and Justification of the Behavior Coefficient As shown in Fig. III.2, lateral loads are resisted exclusively by the shear walls distributed throughout the structure. To quantify this, the shear resistance provided by the walls is evaluated by comparing the shear force at the base of the walls to the total base shear, as summarized in Table III.16.

Table III.16: Shear force distribution: wall base vs. total base shear

Direction	Wall Base Shear (kN)	Total Base Shear (kN)	Percentage
X	9663.10	9663.10	100%
Y	12662.44	12662.44	100%

In both principal directions, the shear force resisted by the vertical structural walls reaches 100% of the total base shear, thus greatly exceeding the 65% threshold required by the RPA 2024 definition for a shear wall braced system. This confirms that the structure fully satisfies the criterion.

Furthermore, the absence of a core or core-like bracing system ("effet noyau") is verified by checking the conditions of equation (3.17) of RPA 2024 [34]. As demonstrated in Table III.12, the ratios l_s/r_x and l_s/r_y are both less than unity, meaning that r_x and r_y are superior to l_s (see Table III.11 also). This configuration does NOT satisfy the condition required for a core-type system, as equation (3.17) requires both radii to be less than l_s to qualify as an "effet noyau". Therefore, the criteria are not met, confirming that the structure does not behave as a core-braced system.

Consequently, according to Table 4.3 of RPA 2024 [34], the bracing system of the present building corresponds to system entry:

5 Shear wall braced system $\boxed{R = 4.5^{(b)}}$

3.5.4 Design Spectrum

Quality Factor It is defined as [34]:

$$Q_f = 1 + \sum_{q=1}^{i} P_q$$

where P_q are penalty increments associated with the absence of specific lateral force-resisting system quality measures defined in Category (b) weightings [34]. The relevant criteria and their assessment are as follows:

- **q1** – Observed plan irregularity (see Table III.13): $P_{q1} = 0.05$.
- **q2** – Observed elevation irregularity (see Table III.15): $P_{q2} = 0.20$.
- **q3** – Verified by inspection of the typical floor plan (Figure III.2): condition is satisfied, $P_{q3} = 0$.

The quality factor is therefore:

$$Q_f = 1 + \sum P_q = 1 + 0.05 + 0.20 + 0 = \boxed{1.25}$$

Seismic Parameters and Design Spectrum The design spectrum $S_{ad}(T)/g$ is constructed from the seismic parameters determined for the site and the structure [34]. The adopted values are summarized in Table III.17.

Table III.17: Seismic parameters adopted for the design spectrum

Parameter	Symbol	Value
Peak ground acceleration coefficient	A	0.30 (Zone IV)
Site coefficient	S	1.30 (Site S3)
Importance factor	I	1.20 (Group 1B)
Behavior coefficient	R	4.50 (Shear walls)
Quality factor	Q_f	1.25

The design spectrum is defined by the piecewise function [34]:

$$\frac{S_{ad}}{g}(T) = \begin{cases} A \cdot I \cdot S \left[\frac{2}{3} + \frac{T}{T_1}\left(2.5\,\frac{Q_f}{R} - \frac{2}{3}\right)\right] & 0 \leq T < T_1 \\ A \cdot I \cdot S \left[2.5\,\frac{Q_f}{R}\right] & T_1 \leq T < T_2 \\ A \cdot I \cdot S \left[2.5\,\frac{Q_f}{R}\right] \cdot \left[\frac{T_2}{T}\right] & T_2 \leq T < T_3 \\ A \cdot I \cdot S \left[2.5\,\frac{Q_f}{R}\right] \cdot \left[\frac{T_2 \cdot T_3}{T^2}\right] & T_3 \leq T < 4\,\mathrm{s} \end{cases} \tag{III.1}$$

The resulting design spectrum is plotted in Figure III.5.

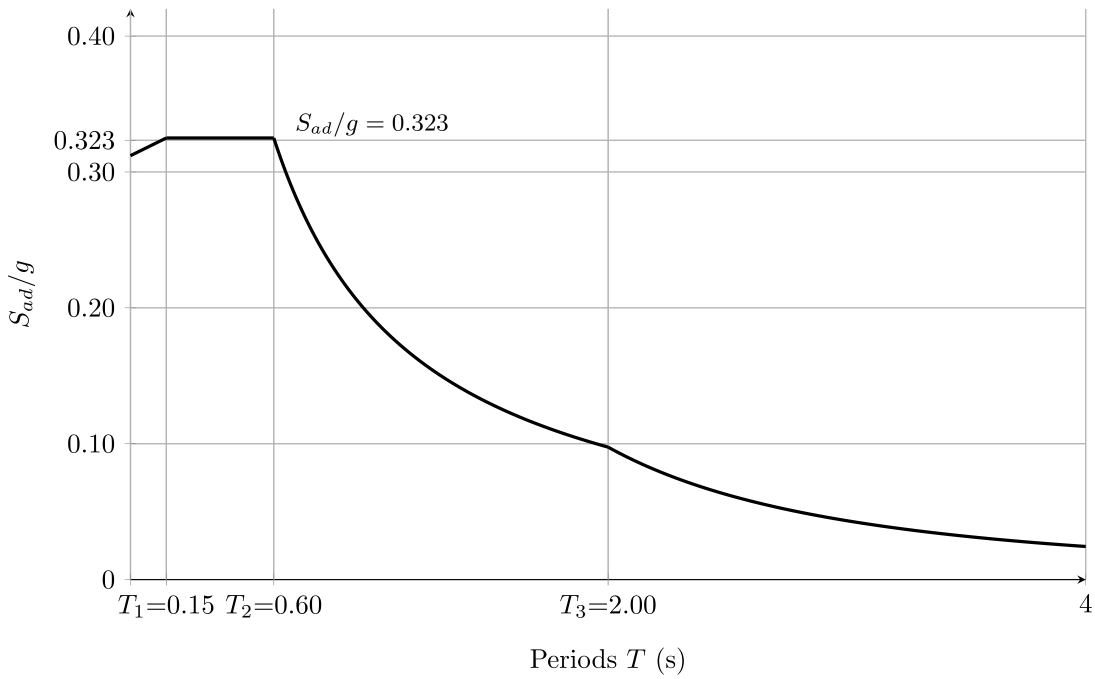

Figure III.5: Design spectrum $S_{ad}(T)/g$ according to RPA 2024

3.5.5 Seismic Base Shear Verification

According to §4.3.5 of RPA 2024 [34], the base shear obtained from the response spectrum analysis must not be less than 80% of the base shear calculated using the equivalent static force method (Eq. 4.1):

$$V = \lambda \cdot \frac{S_{ad}}{g}(T_0) \cdot W \tag{III.2}$$

Determination of the Fundamental Period The fundamental periods obtained from the modal analysis (Table III.8) are:

$$T_{0,x} = 0.849\,\text{s}, \quad T_{0,y} = 0.643\,\text{s}$$

These values must be compared with the empirical period estimated from RPA 2024 formula:

$$T_{empirical} = C_T \cdot (h_N)^{3/4}$$

where:

- $C_T = 0.075$ (coefficient for the shear wall bracing system)
- $h_N = 33.66\,\text{m}$ (total height of the structure from the base)

$$T_{empirical} = 0.075 \cdot (33.66)^{3/4} = 1.05\,\text{s}$$

According to RPA 2024, the numerical periods must not exceed the empirical period by more than 30%:

$$T_{0,x} = 0.849\,\text{s} < 1.3 \cdot T_{empirical} = 1.365\,\text{s} \quad \text{(OK)}$$

Determination of the Parameters

Correction Factor λ: Given that $T_1 = 0.15\,\text{s}$, $T_2 = 0.60\,\text{s}$, and $T_3 = 2.00\,\text{s}$ (see Table III.17), and since $T_0 < 2 \cdot T_2$ and the building has more than two stories, $\lambda = 0.85$.

Seismic Weight W: According to RPA 2024 [34], the seismic weight is calculated as:

$$W = \sum_{i=1}^{n} W_i \quad \text{with} \quad W_i = W_{Gi} + \Psi \cdot W_{Qi}$$

For Case 1 (Table 4.2 [34]), $\Psi = 0.3$. From the numerical model:

$$W = 50370.856\,\text{kN}$$

Design Spectral Acceleration: Both $T_{0,x}$ and $T_{0,y}$ lie between T_2 and T_3 (see Table III.17 and Eq. III.1). Therefore, the design spectral acceleration is given by:

$$\frac{S_{ad}}{g}(T) = A \cdot I \cdot S \cdot \left(2.5 \times \frac{Q_f}{R}\right) \cdot \frac{T_2}{T}$$

This yields:

$$\frac{S_{ad}}{g}(T_{0,x}) = 0.230$$
$$\frac{S_{ad}}{g}(T_{0,y}) = 0.303$$

Base Shear Verification The static base shear is calculated using Eq. III.2:

$$V_{static,x} = \lambda \cdot \frac{S_{ad}}{g}(T_{0,x}) \cdot W = 0.85 \times 0.230 \times 50370.856 = 9837.72\,\mathrm{kN}$$
$$V_{static,y} = \lambda \cdot \frac{S_{ad}}{g}(T_{0,y}) \cdot W = 0.85 \times 0.303 \times 50370.856 = 12970.37\,\mathrm{kN}$$

The 80% requirement (§4.3.5) gives the minimum allowable base shear from the response spectrum analysis:

$$V_{min,x} = 0.8 \times V_{static,x} = 7870.18\,\mathrm{kN}$$
$$V_{min,y} = 0.8 \times V_{static,y} = 10376.30\,\mathrm{kN}$$

The base shear obtained from the response spectrum analysis (Table III.16) is:

$$V_{dyn,x} = 9663.10\,\mathrm{kN}$$
$$V_{dyn,y} = 12662.44\,\mathrm{kN}$$

The verification is summarized in Table III.18.

Table III.18: Base shear verification summary

Direction	**V$_{static}$ (kN)**	**0.8 × V$_{static}$ (kN)**	**V$_{dyn}$ (kN)**	**Verification**
X	9837.72	7870.18	9663.10	**OK**
Y	12970.37	10376.30	12662.44	**OK**

In both directions, the dynamic base shear exceeds the minimum required threshold, thus satisfying the RPA 2024 §4.3.5 requirement.

3.5.6 Inter-story Drift Verification

In accordance with § 5.10 of RPA 2024 [34], two drift checks are required: a *non-collapse* check (§ 5.10.1) and a *damage limitation* check (§ 5.10.2).

Non-collapse verification (§ 5.10.1). The inelastic inter-story drift Δ_k, obtained from the elastic displacement δ_{ek} via (§ 4.5.2, Eqn. (4.15)):

$$\delta_k = \frac{R}{Q_F}\,\delta_{ek} \tag{III.3}$$

$$\Delta_k = \delta_k - \delta_{k-1} \tag{III.4}$$

must satisfy the limit of Table 5.2 of [34]. For a *BÃ¢timent en BÃ©ton ArmÃ©*:

$$\Delta_k \leq \overline{\Delta}_k = 0.0150\,h_k \tag{III.5}$$

With $h_k = 3040$ mm, this gives $\overline{\Delta}_k = 45.6$ mm.

Damage limitation verification (§ 5.10.2, Eqn. (5.13)). For buildings with ductile non-structural elements, the reduced drift must satisfy:

$$\nu_A \cdot \Delta_k \leq 0.0075\,h_k \tag{III.6}$$

where $\nu_A = 0.5$ is the importance-reduction coefficient (§ 1.2). With $h_k = 3040$ mm, the allowable reduced drift is $0.0075 \times 3040 = 22.8$ mm. The structure is analyzed with $R = 4.5$ and $Q_F = 1.25$. The verification results for both principal directions are summarized in Tables III.19 and III.20.

Table III.19: Elastic and inelastic floor displacements ($R = 4.5$, $Q_F = 1.25$)

Floor	**Elastic Displacement (mm)**		**Inelastic Displacement (mm)**	
	$\delta_{x,ek}$	$\delta_{y,ek}$	$\delta_{x,k}$	$\delta_{y,k}$
10	62.889	54.386	226.400	195.790
9	57.874	47.660	208.346	171.576
8	52.555	40.865	189.198	147.114
7	45.843	33.944	165.035	122.198
6	38.570	27.051	138.852	97.384
5	30.927	20.402	111.337	73.447
4	22.979	14.246	82.724	51.286
3	15.359	8.811	55.292	31.720
2	8.410	4.389	30.276	15.800
1	2.851	1.314	10.264	4.730

Table III.20: Inter-story drift verification

Floor	Inter-story Drift Δ_k (mm)		Reduced Drift $\nu_A \Delta_k$ (mm)	
	$\Delta_{x,k}$	$\Delta_{y,k}$	$\nu_A \Delta_{x,k}$	$\nu_A \Delta_{y,k}$
10	19.523	24.217	9.761	12.109
9	20.383	24.484	10.192	12.242
8	24.358	24.779	12.179	12.389
7	26.204	24.628	13.102	12.314
6	27.767	23.695	13.883	11.848
5	28.235	22.021	14.117	11.011
4	27.353	19.444	13.676	9.722
3	24.750	15.815	12.375	7.907
2	19.753	11.005	9.877	5.503
1	10.109	4.752	5.054	2.376

Note: All inelastic drifts Δ_k remain below $\overline{\Delta}_k = 45.6$ mm (non-collapse, Table 5.2), and all reduced drifts $\nu_A \Delta_k$ remain below 22.8 mm (damage limitation, Eqn. (5.13)) at every level and in both directions, satisfying § 5.10.1 and § 5.10.2 of [34].

3.5.7 P-Δ Effect Verification

Per § 5.9 of RPA 2024 [34], second-order (P-Δ) effects may be neglected at all levels of a building provided the inter-story stability index θ_k, defined as:

$$\theta_k = \frac{P_k \cdot \Delta_k}{V_k \cdot h_k} \leq 0.10 \tag{III.7}$$

is satisfied at every level. When $0.10 \leq \theta_k \leq 0.20$, P-Δ effects can no longer be neglected and all seismic action effects obtained from a first-order elastic analysis must be amplified by the factor $\dfrac{1}{1-\theta_k}$. Beyond that, any level for which $\theta_k \geq 0.20$ renders the structure potentially unstable, necessitating a complete redesign.

The total gravity load P_k acting above level k combines the permanent and live loads of all floors from level k to the roof:

$$P_k = \sum_{i=k}^{n} (G_i + \psi \cdot Q_i) \tag{III.8}$$

where G_i and Q_i are respectively the characteristic permanent and live loads at level i, and ψ is the load combination coefficient. The story shear $V_k = \sum_{i=k}^{n} F_i$ represents the cumulative lateral seismic force above level k, decreasing from base to roof, while Δ_k is the inelastic inter-story drift already established in Eqn. (III.4). The stability index θ_k is evaluated independently in both principal directions x and y. The required input quantities and resulting θ_k values are reported in Tables III.21 and III.22.

Table III.21: Cumulative gravity loads and story shears for P-Δ verification

Floor	Gravity Load P_k (kN)	Story Shear (kN)	
		$V_{x,k}$	$V_{y,k}$
10	5 400.019	2 024.207	2 878.402
9	10 018.592	3 568.204	5 029.640
8	14 981.607	4 924.610	6 877.038
7	19 965.954	6 053.338	8 388.352
6	24 986.836	7 011.085	9 647.127
5	30 063.640	7 844.625	10 688.228
4	35 140.444	8 550.291	11 513.362
3	40 217.248	9 106.460	12 128.134
2	45 294.052	9 486.133	12 514.447
1	50 370.856	9 663.103	12 662.439

Table III.22: P-Δ stability index verification

Floor	Inter-story Drift Δ_k (mm)		Stability Index θ_k (%)	
	$\Delta_{x,k}$	$\Delta_{y,k}$	$\theta_{x,k}$	$\theta_{y,k}$
10	19.523	24.217	1.71	1.49
9	20.383	24.484	1.88	1.60
8	24.358	24.779	2.44	1.78
7	26.204	24.628	2.84	1.93
6	27.767	23.695	3.26	2.02
5	28.235	22.021	3.56	2.04
4	27.353	19.444	3.70	1.95
3	24.750	15.815	3.60	1.73
2	19.753	11.005	3.10	1.31
1	10.109	4.752	1.73	0.62
Note: All stability indices satisfy $\theta_k \leq 0.10$ (10%) in both directions at every level; P-Δ effects are therefore negligible and no amplification factor is required per § 5.9 of [34].				

3.6 Structural Element Design

3.6.1 Load Combinations

In accordance with the limit state design philosophy adopted by RPA 2024 [34], seismic action is treated as an accidental action owing to its brief duration. The seismic action is characterised by three simultaneously acting components: two horizontal components, E_x and E_y, acting along two orthogonal directions in the plane of the structure, and one vertical component, E_z, acting along the vertical axis of the structure.

Ultimate Limit State (ULS) and Serviceability Limit State (SLS). The conventional static load combinations are defined in accordance with CBA 93 [**cba93**] and BAEL 91/99 [**bael91**]:

$$\text{ULS:} \quad 1.35\,G + 1.5\,Q \tag{III.9}$$

$$\text{SLS:} \quad G + Q \tag{III.10}$$

Seismic Combinations. The horizontal components of the seismic action are assumed independent but represented by the same response spectrum. Seismic actions are combined with permanent and variable actions through the following expressions (§ 5.2 of RPA 2024 [34]):

$$\begin{cases} G + \psi Q + E_1 \\ G + \psi Q + E_2 \end{cases} \tag{III.11}$$

where G denotes the characteristic permanent loads, Q the characteristic variable loads (unweighted), and $\psi = 0.4$ the load combination coefficient for residential occupancy (Table 4.2 of RPA 2024 [34]). The directional combination of horizontal components is:

$$\begin{cases} E_1 = \pm E_x \pm 0.3\,E_y \\ E_2 = \pm 0.3\,E_x \pm E_y \end{cases} \tag{III.12}$$

The sign of each component is taken as the most unfavourable for the effect under consideration. For the seismic combinations, the material safety coefficients are reduced to $\gamma_b = 1.15$ for concrete and $\gamma_s = 1.0$ for steel, reflecting the accidental nature of the seismic action. The design combinations applied to each structural element are summarised in Table III.23.

Table III.23: Design load combinations used for structural element sizing.

Combination	Expression	Application
ULS (gravity)	$1.35\,G + 1.5\,Q$	Midspan moments; slabs
SLS	$G + Q$	Deflection & stress checks
Seismic comb. 1	$G + 0.3\,Q + (\pm E_x \pm 0.3\,E_y)$	Support moments; shear walls
Seismic comb. 2	$G + 0.3\,Q + (\pm 0.3\,E_x \pm E_y)$	Support moments; shear walls

3.6.2 Slab Design – Critical Panel ($l_x \times l_y = 5.09 \times 7.57$ m, $e = 20$ cm)

The critical slab panel selected for design is the largest panel on the typical floor, with clear dimensions $l_x \times l_y = 5.09\,\text{m} \times 7.57\,\text{m}$ and a thickness $e = 20$ cm. The panel position within the structural plan is indicated in Figure III.6.

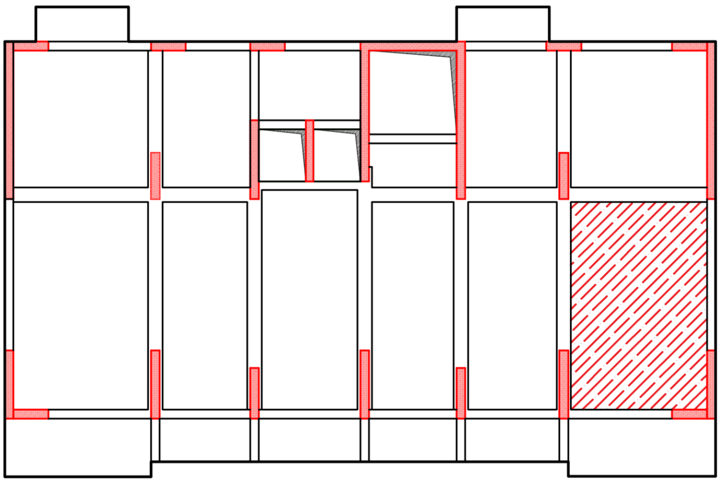

Figure III.6: Floor plan showing the location of the critical slab panel.

The design follows the lump-sum moment method (*mÃ©thode forfaitaire*) of BAEL 91/99, applicable to uniformly distributed loads. The cross-section is designed in simple bending for a $b = 1000$ mm wide strip.

Panel Classification.

$$\alpha = \frac{l_x}{l_y} = \frac{5.09}{7.57} = 0.673 \tag{III.13}$$

Since $0.4 \leq \alpha = 0.673 \leq 1$, the panel acts as a **two-way slab**, carrying loads in both principal directions.

Design Loads. The self-weight of the 20 cm slab is $0.20 \times 25 = 5.00$ kN/m^2. Together with the superimposed dead load, the total permanent load is $G = 5.00 + 2.70 = 7.70$ kN/m^2, and the live load is $Q = 1.50$ kN/m^2. The design intensities are summarised in Table III.24:

$$P_u = 1.35\,G + 1.5\,Q = 1.35 \times 7.70 + 1.5 \times 1.50 = 12.64\,\text{kN/m}^2 \tag{III.14}$$

$$P_{ser} = G + Q = 7.70 + 1.50 = 9.20\,\text{kN/m}^2 \tag{III.15}$$

Table III.24: Design loads for the critical slab panel.

G **(kN/m^2)**	Q **(kN/m^2)**	P_u **(kN/m^2)**	P_{ser} **(kN/m^2)**
7.70	1.50	12.64	9.20

Bending Coefficients. The coefficients μ_x and μ_y are extracted from the BAEL 91/99 tables as a function of α, using $\nu = 0$ for stress resultants and $\nu = 0.2$ for deformation checks. By linear interpolation at $\alpha = 0.673$ (see Table III.25):

Table III.25: BAEL 91/99 bending coefficients for the critical slab panel.

State	α	μ_x	μ_y
ULS ($\nu = 0$)	0.673	0.0607	0.0341
SLS ($\nu = 0.2$)	0.673	0.0677	0.0618

Isostatic and Design Moments. The isostatic moments are obtained from $M_0 = \mu \cdot P \cdot l_x^2$. Continuity with adjacent panels is accounted for by the BAEL 91/99 *forfaitaire* coefficients: $0.75\,M_0$ at midspan and $0.50\,M_0$ at supports, as detailed in Table III.26.

Table III.26: Design moments for the critical slab panel (isostatic: $M_{0x}^u = 19.89$ kN·m, $M_{0y}^u = 11.17$ kN·m).

Position	**Coeff.**	**Direction**	M^u **(kN·m)**	M^{ser} **(kN·m)**
Midspan	0.75	x	14.92	12.11
Midspan	0.75	y	8.38	11.06
Support	0.50	$x\,\&\,y$	9.95	8.07

Shear Forces.

$$V_{max,x} = \frac{P_u \cdot l_x \cdot l_y}{2\,l_y + l_x} = \frac{12.64 \times 5.09 \times 7.57}{2 \times 7.57 + 5.09} = 24.07\,\text{kN/m} \tag{III.16}$$

$$V_{max,y} = \frac{P_u \cdot l_x}{3} = \frac{12.64 \times 5.09}{3} = 21.44\,\text{kN/m} \tag{III.17}$$

Reinforcement Design (ULS – Pure Bending). Section geometry: $b = 1000$ mm, $h = 200$ mm, $d = 180$ mm (cover $c' = 20$ mm), $f_{bu} = 0.85 \times 30/1.5 = 17.0$ MPa, $\sigma_s = 500/1.15 = 435$ MPa (Table III.27).

Table III.27: ULS reinforcement for the critical slab panel ($b = 1000$ mm, $h = 200$ mm, $d = 180$ mm; moments in kN·m, areas in cm²/m).

Position	**Dir.**	M_u	μ_u	α	z **(mm)**	$A_{s,req}$ **(cm²/m)**	$A_{s,prov}$
Midspan	x	14.92	0.027	0.034	177.5	1.93	$5\emptyset 8 = 2.51$
Midspan	y	8.38	0.015	0.019	178.6	1.08	$5\emptyset 8 = 2.51$
Support	$x\&y$	9.95	0.018	0.023	178.4	1.28	$5\emptyset 8 = 2.51$

Minimum Reinforcement and Bar Diameter. Per BAEL 91/99 with $f_e = 500$ MPa:

$$A_{y,min} = 6h \times 10^{-3} \cdot b = 6 \times 0.20 \times 10^{-3} \times 1000 = 1.20\,\text{cm}^2/\text{m} \tag{III.18}$$

$$A_{x,min} = \frac{3-\alpha}{2} A_{y,min} = \frac{3-0.673}{2} \times 1.20 = 1.40\,\text{cm}^2/\text{m} \tag{III.19}$$

All provided areas ($A_s = 2.51$ cm^2/m) satisfy both minima. The bar diameter is limited to $\emptyset \leq h/10 = 20$ mm; adopted $\emptyset = 8$ mm.

Bar Spacing. For lightly cracked members (BAEL 91/99, Art. A.7.2.4.2):

$$S_{tx} \leq \min(3h;\, 33\,\text{cm}) = 33\,\text{cm} \quad \Rightarrow \quad S_{tx} = 20\,\text{cm} \tag{III.20}$$

$$S_{ty} \leq \min(4h;\, 45\,\text{cm}) = 45\,\text{cm} \quad \Rightarrow \quad S_{ty} = 20\,\text{cm} \tag{III.21}$$

Shear Verification (BAEL 91/99, Art. A.5.2.2).

$$\tau_u = \frac{V_{max}}{bd} = \frac{24.07 \times 10^3}{1000 \times 180} = 0.134\,\text{MPa} \;\leq\; \bar{\tau}_u = \min\left(\frac{0.15\, f_{c28}}{\gamma_b};\, 4\,\text{MPa}\right) = 3.0\,\text{MPa} \quad \checkmark \tag{III.22}$$

Transverse reinforcement is **not required**.

SLS Stress Verification. Neutral axis depth from cracked-section equilibrium ($A'_s = 0$, $\eta = 15$, $A_s = 2.51\,\text{cm}^2/\text{m}$):

$$\frac{b}{2} x_0^2 - \eta A_s (d - x_0) = 0 \;\Rightarrow\; x_0 = 33.3\,\text{mm} \tag{III.23}$$

$$I = \frac{b x_0^3}{3} + \eta A_s (d - x_0)^2 = 9.33 \times 10^{-5}\,\mathrm{m}^4 \tag{III.24}$$

$$\sigma_{bc} = \frac{M_{ser}^{+} \cdot x_0}{I} = \frac{12.11 \times 10^{-3} \times 0.0333}{9.33 \times 10^{-5}} = 4.32\,\mathrm{MPa} \;\leq\; 0.6 f_{c28} = 18\,\mathrm{MPa} \quad \checkmark \tag{III.25}$$

The adopted reinforcement layout is shown in Figure III.7.

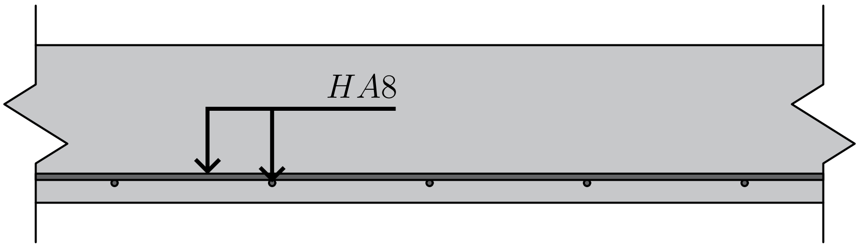

Figure III.7: Adopted reinforcement cross-section for the critical slab panel (5∅8/m in both directions, $e = 20$ cm).

3.6.3 Beam Design – Critical Beam ($b \times h = 30 \times 45$ cm^2, Story 7, Axis Y / Axis A)

The beam selected for design is identified as the most critically loaded element in the Y-direction, located at Story 7 along structural axis A (see Figure III.8). Its cross-section is $b \times h = 30 \times 45$ cm^2. Internal forces were extracted from the ETABS model for each governing combination, and the reinforcement areas were determined using the *BealR* software by SOCOTEC (rectangular RC sections in simple or combined bending per BAEL 91 [**bael91**]).

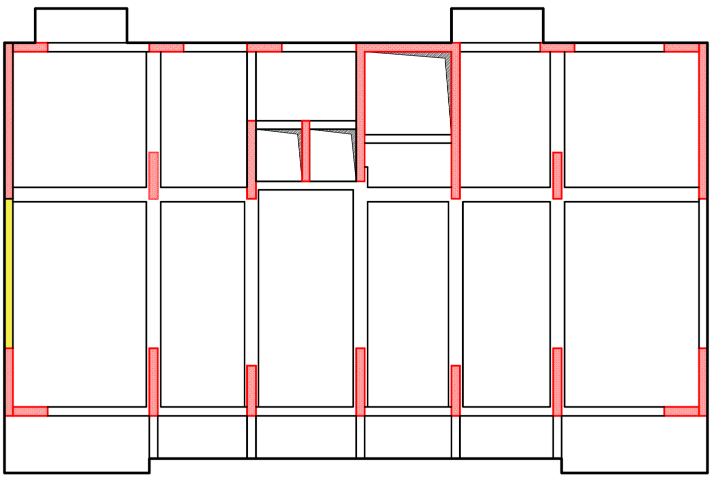

Figure III.8: Floor plan showing the location of the critical beam highlighted with yellow (Story 7, axis A see figure III.2 for the full floor plan).

Critical Zone Length (Ductility Requirements). Per Article 7.5.2 of RPA 2024 [34], the critical length at each beam-column interface is:

$$l_{cr} = 1.5\,h = 1.5 \times 45 = 67.5\,\text{cm} \tag{III.26}$$

Specific detailing rules apply within this zone and in the current zone beyond it.

Governing Solicitations. Two distinct combination types control the design at each critical cross-section. The ULS gravity combination ($1.35G + 1.5Q$) governs the sagging midspan moment, whereas the seismic combinations ($G + 0.3Q + E_i$), with reduced material coefficients ($\gamma_b = 1.15$, $\gamma_s = 1.0$), govern the support moments in both hogging and sagging senses. The governing solicitations are summarised in Table III.28.

Table III.28: Governing solicitations for the critical beam (30×45 cm^2, Story 7, Axis Y/A).

Section	M_u (kN·m)	Governing combination	V_u (kN)
At support – hogging (top)	-402.4	Seismic: $G+0.3Q+E_i$	-171.68
At support – sagging (bot.)	$+340.0$	Seismic: $G+0.3Q+E_i$	$+110.18$
At midspan – sagging (bot.)	$+39.27$	ULS: $1.35G+1.5Q$	$+62.88$
ULS support (gravity only): $M^- = -74.32$ kN·m. SLS: $M^-_{sup} = -54.37$ kN·m, $M^+_{mid} = +44.72$ kN·m.			

Longitudinal Reinforcement – BealR Results. The required steel areas computed by BealR are reported in Table III.29. Note that BealR applies the reduced seismic material coefficients ($\gamma_b = 1.15$, $\gamma_s = 1.0$) automatically for the seismic combinations and standard coefficients ($\gamma_b = 1.5$, $\gamma_s = 1.15$) for the ULS gravity case.

Table III.29: BealR (SOCOTEC) results for longitudinal reinforcement per loading case ($b = 0.3$ m, $h = 0.45$ m, $c' = 0.04$ m).

Section	M_u (kN·m)	A_s^{sup} (cm^2)	A_s^{inf} (cm^2)	y_0 (m)
Midspan (ULS gravity)	$+39.27$	0	2.26	0.02
Support (seismic, hogging)	-402.4	25.9	0.14	0.24
Support (seismic, sagging)	$+340.0$	0	20.58	0.19

RPA 2024 Reinforcement Limits and Adopted Bars. The governing area at each face is obtained by taking the maximum over all loading cases. Per Article 7.5.2 of RPA 2024 [34]:

- **Minimum total ratio:** $A_{s,min}^{RPA} = 0.5\%\,bh = 0.005 \times 300 \times 450 = 6.75$ cm^2 (on any section).
- **Maximum ratio (current zone):** $A_{s,max} = 4\%\,bh = 54.0$ cm^2.

- **Maximum ratio (lap zones):** $A_{s,max} = 6\% \, bh = 81.0$ cm^2.
- At least two $\emptyset 12$ bars are required continuously on both top and bottom faces along the full beam length.
- A minimum of one quarter of the maximum support top-steel area ($A_r \geq A_{s,sup}/4$) is extended over the full span.

Governing areas at each face, applied minima, and adopted bars are presented in Table III.30.

Table III.30: Governing areas, minima, and adopted longitudinal reinforcement for the critical beam (30×45 cm^2, Story 7, Axis Y/A).

Section (face)	$A_{s,gov}$ **(cm^2)**	$A_{s,min}^{RPA}$ **(cm^2)**	$A_{s,design}$ **(cm^2)**	**Bars adopted**	$A_{s,prov}$ **(cm^2)**
Support – top	25.90	6.75	25.90	`4HA25 + 4HA16`	`27.91`
Support – bottom	20.58	6.75	20.58	`4HA25 + 4HA16`	`27.91`
Midspan – bottom	2.26	6.75	6.75	`4HA16`	`8.04`

Transverse Reinforcement. The selected transverse reinforcement configuration is summarized in Table III.31. The stirrup diameter is bounded by (BAEL 91/99 and RPA 2024):

$$\emptyset_t \leq \min\left(\frac{h}{35}; \frac{b}{10}; \emptyset_l\right) = \min(12.9\,\text{mm};\ 30\,\text{mm};\ \emptyset_l) \quad \Rightarrow \quad \text{adopted: } \emptyset_t = 10\,\text{mm} \tag{III.27}$$

The minimum area at spacing s_t is (RPA 2024, Art. 7.5.2): $A_t \geq 0.003\, s_t\, b$.

Table III.31: Transverse reinforcement for the critical beam (30×45 cm^2).

Zone	**Spacing rule**	s_t **(cm)**	$A_{t,min}$ **(cm^2)**	**Bars adopted**
Critical (nodal)	$\min\left(\frac{h}{4}; 24\emptyset_t; 175\,\text{mm}; 6\emptyset_l\right)$	7	0.63	2 cadres $\emptyset 10$ (3.14 cm^2)
Current zone	$\frac{h}{2} = 22.5\,\text{cm}$	15	1.35	2 cadres $\emptyset 10$ (3.14 cm^2)

Shear Verification (BAEL 91/99). The governing shear is taken from the seismic combination: $V_u = 171.68$ kN.

$$\tau_u = \frac{V_u}{b\,d} = \frac{171.68 \times 10^3}{300 \times 410} = 1.40\,\text{MPa} \ \leq \ \bar{\tau}_u = \min\left(\frac{0.15\, f_{c28}}{\gamma_b}; 4\,\text{MPa}\right) = 3.0\,\text{MPa} \quad \checkmark \tag{III.28}$$

SLS Stress Verification. The SLS bending moments are $M_{ser}^{-} = 54.37$ kN·m at the support and $M_{ser}^{+} = 44.72$ kN·m at midspan (Table III.28). The admissible concrete and steel stresses per BAEL 91/99 are:

$$\bar{\sigma}_{bc} = 0.6\,f_{c28} = 18\,\text{MPa}, \qquad \bar{\sigma}_s = \min\!\left(\tfrac{2}{3}f_e;\ 110\sqrt{\eta\,f_{tj}}\right) = \min(333;\ 215.7) = 215.7\,\text{MPa} \tag{III.29}$$

where $f_{tj} = 0.6 + 0.06\,f_{c28} = 2.4$ MPa and $\eta = 1.6$ (HA bars).

At the support ($A_s^{top} = 25.9$ cm^2, $A_s^{bot} = 20.58$ cm^2, doubly reinforced, $d = 410$ mm, $d' = 40$ mm, $\eta = 15$):

Neutral axis depth from cracked-section equilibrium:

$$\frac{b}{2}x_0^2 + \eta A_s^{bot}(x_0 - d') - \eta A_s^{top}(d - x_0) = 0 \;\Rightarrow\; x_0 = 104.7\,\text{mm} \tag{III.30}$$

$$I = \frac{bx_0^3}{3} + \eta A_s^{bot}(x_0 - d')^2 + \eta A_s^{top}(d - x_0)^2 = 3.858 \times 10^{-3}\,\text{m}^4 \tag{III.31}$$

$$\sigma_{bc} = \frac{M_{ser}^{-} \cdot x_0}{I} = \frac{54.37 \times 10^{-3} \times 0.1047}{3.858 \times 10^{-3}} = 1.48\,\text{MPa} \;\leq\; 18\,\text{MPa} \quad \checkmark \tag{III.32}$$

$$\sigma_s = \frac{\eta\,M_{ser}^{-} \cdot (d - x_0)}{I} = \frac{15 \times 54.37 \times 10^{-3} \times 0.3053}{3.858 \times 10^{-3}} = 64.6\,\text{MPa} \;\leq\; 215.7\,\text{MPa} \quad \checkmark \tag{III.33}$$

At midspan ($A_s^{bot} = 6.75$ cm^2, singly reinforced, $d = 410$ mm):

$$\frac{b}{2}x_0^2 - \eta A_s^{bot}(d - x_0) = 0 \;\Rightarrow\; x_0 = 52.3\,\text{mm} \tag{III.34}$$

$$I = \frac{bx_0^3}{3} + \eta A_s^{bot}(d - x_0)^2 = 1.310 \times 10^{-3}\,\text{m}^4 \tag{III.35}$$

$$\sigma_{bc} = \frac{M_{ser}^{+} \cdot x_0}{I} = \frac{44.72 \times 10^{-3} \times 0.0523}{1.310 \times 10^{-3}} = 1.78\,\text{MPa} \;\leq\; 18\,\text{MPa} \quad \checkmark \tag{III.36}$$

$$\sigma_s = \frac{\eta\,M_{ser}^{+} \cdot (d - x_0)}{I} = \frac{15 \times 44.72 \times 10^{-3} \times 0.3577}{1.310 \times 10^{-3}} = 183.2\,\text{MPa} \;\leq\; 215.7\,\text{MPa} \quad \checkmark \tag{III.37}$$

Both sections satisfy the SLS stress conditions; no adjustment to the adopted reinforcement is required.

The adopted reinforcement cross-sections for the beam at support and at midspan are illustrated in Figure III.9.

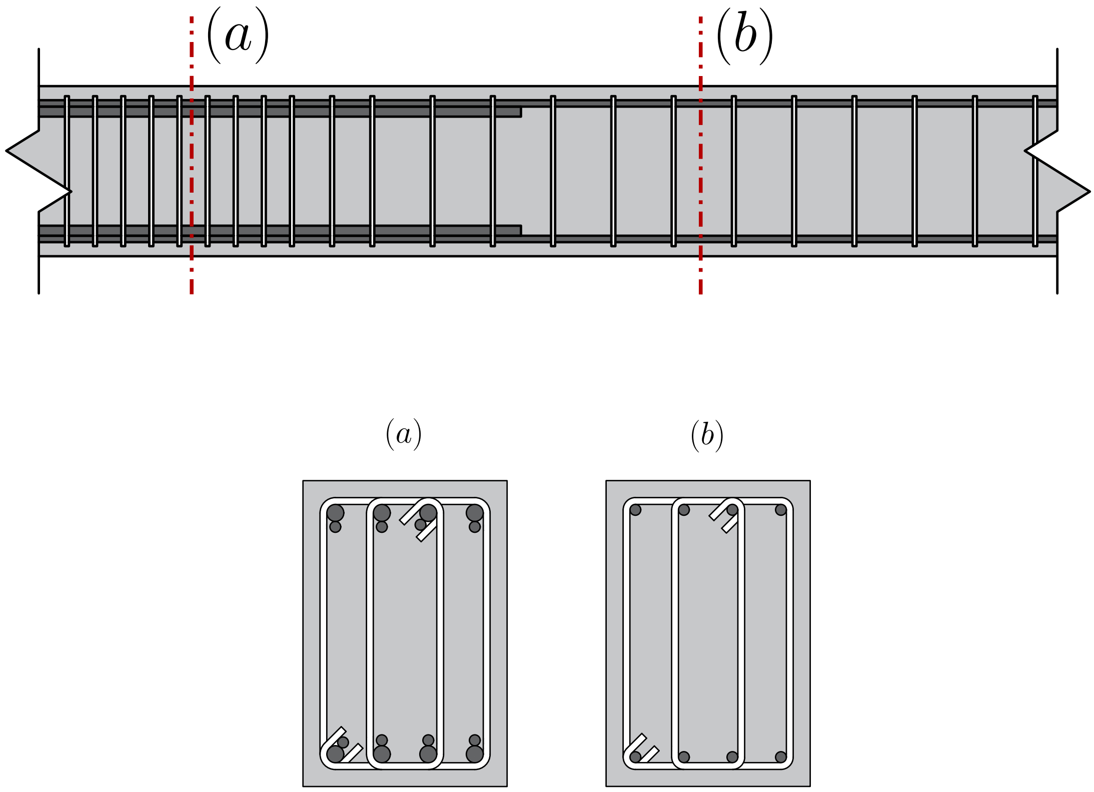

Figure III.9: Reinforcement detailing for the critical beam (30×45 cm^2). The support section is heavily reinforced with 4HA25 + 4HA16 at both the top and bottom. At midspan, the primary bottom reinforcement consists of 4HA16. Transverse reinforcement comprises 2 Ø10 stirrups (cadres).

3.6.4 Shear Wall Design Example

For the purpose of this design example, three identical shear walls that experience nearly equal moments, shear, and axial forces were selected. The dimensions of these shear walls are $l_w = 2350$ mm and $b_w = 300$ mm. The selected shear walls are highlighted in the layout below (Figure III.10).

The maximum forces at the base of the three shear walls are summarized in Table III.32.

Table III.32: Maximum forces at the base of the selected shear walls.

Pier	**Max Abs M_3 (kN·m)**	**Max Abs V_2 (kN)**	**Max Abs P (kN)**
PY11_Lw235	3,258.87	404.33	4,571.51
PY13_Lw235	3,401.36	414.23	4,646.95
PY9_Lw235	**3,853.27**	**474.36**	**4,705.37**

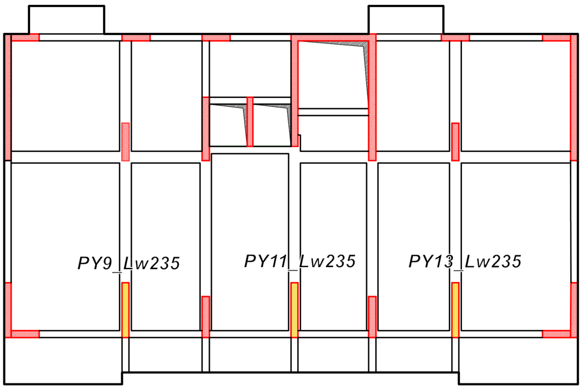

Figure III.10: Selected shear walls for design (highlighted in yellow).

As shown in the table, **PY9_Lw235** (the far-left shear wall) is the most heavily loaded. This is expected, given its location furthest from the central concrete core. Therefore, the design forces from PY9 will be used to size all three of these shear walls conservatively.

In accordance with the RPA (RÃ¨gles Parasismiques AlgÃ©riennes), the design will be governed by the moment and shear envelopes, which will be introduced later in this section.

Geometric Constraints Verification. According to the RPA requirements for shear wall dimensions:

$$l_w \geq \max\left(\frac{h_e}{3};\ 4b_w;\ 1\ \text{m}\right) \tag{III.38}$$

$$l_w = 2350\ \text{mm} \geq 1200\ \text{mm} \quad \textbf{Verified.} \tag{III.39}$$

$$b_w = 30\ \text{cm} \geq \max\left(15\ \text{cm};\ \frac{h_e}{20}\right) \quad \textbf{Verified.} \tag{III.40}$$

Reduced Axial Load Verification. The reduced axial load is verified to ensure it remains below the required limit:

$$\nu_d = \frac{N_d}{B_c \times f_{c28}} = \frac{4705.4}{(2.35 \times 0.3) \times 30 \times 10^3} = 0.22 < 0.4 \quad \textbf{Verified.} \tag{III.41}$$

To determine whether the moment and shear envelopes must be used to size these shear walls, we evaluate the slenderness ratio h_w/l_w. A ratio greater than 2 indicates a slender shear wall (“voile Ã©lancÃ©”), which mandates the use of design envelopes.

$$\frac{h_w}{l_w} = \frac{30.6}{2.35} = 13.02 \gg 2 \tag{III.42}$$

Thus, the design envelopes are required. The forces envelopes are shown in Figure III.11 and will be used for sizing according to the RPA.

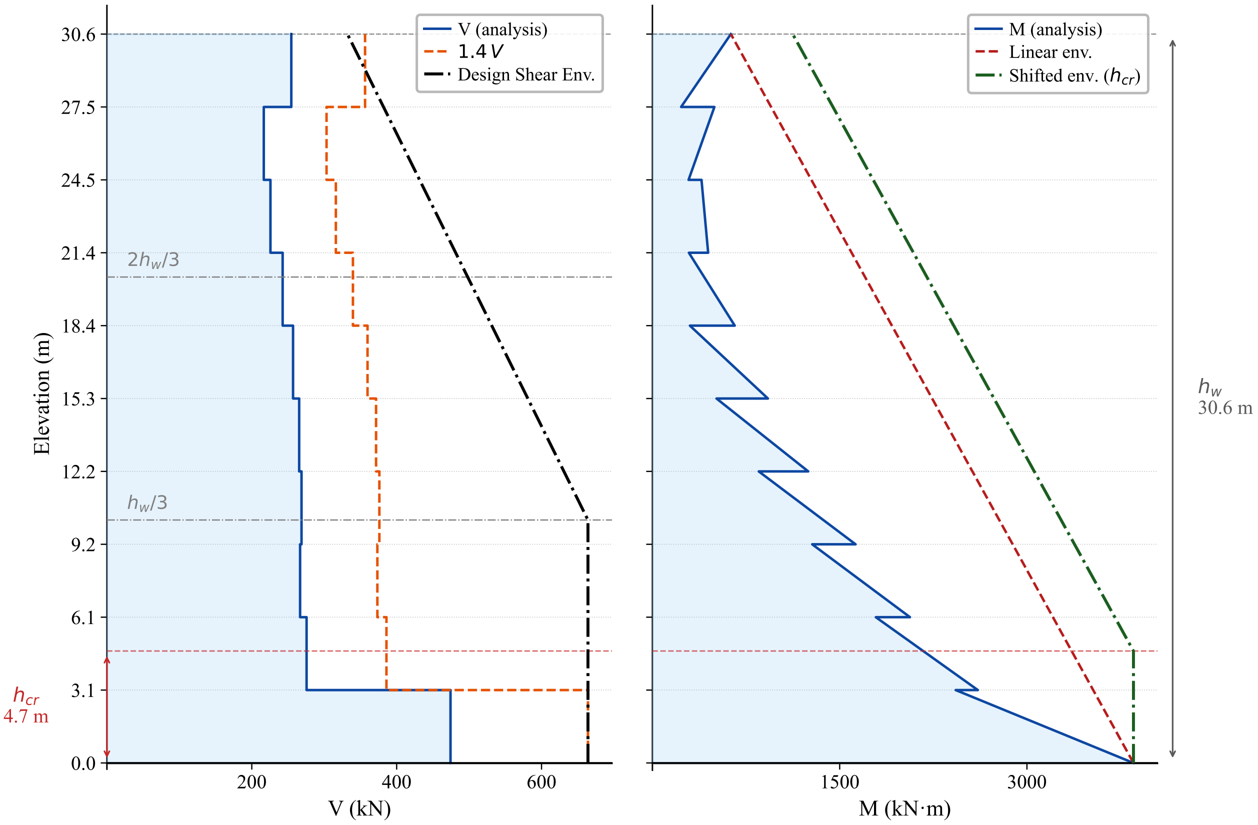

Figure III.11: Design forces envelopes used for shear wall sizing according to RPA.

Next, we determine the critical height (h_{cr}), which empirically encompasses the region susceptible to plastic hinge formation.

$$h_{cr} = \max\left(l_w;\ \frac{h_w}{6}\right) = \max(2.35;\ 5.10) = 5.10\ \text{m} \tag{III.43}$$

Additionally, the critical height must satisfy:

$$h_{cr} \le \begin{cases} 2\,l_w \\ 2\,h_e & \text{for } n > 6 \text{ stories} \end{cases} \tag{III.44}$$

$$h_{cr} = 5.10\ \text{m} \le \min(2 \times 2.35;\ 2 \times 3.05) \tag{III.45}$$

Since 5.10 m $>$ 4.70 m, we adopt $h_{cr} = 4.7$ m.

Confined Boundary Elements: Geometric Conditions. The minimum length of the confined boundary element (l_c) is given by:

$$l_c \geq \max(0.15\, l_w \ ; \ 1.5\, b_w) \tag{III.46}$$

$$l_c \geq \max(0.15 \times 235 \ ; \ 1.5 \times 30) = \max(35.25 \ ; \ 45) = 45 \text{ cm} \tag{III.47}$$

An initial design considered $l_c = 45$ cm. However, a subsequent local ductility check revealed that the calculated compressed length was $l_{c,\text{calculated}} = 71.29$ cm $> l_c$. This indicated that the chosen boundary zone was insufficient to contain the plastic hinge region. Therefore, we adopt a larger boundary element length:

$$l_c = 75 \text{ cm} \tag{III.48}$$

With a concrete cover of 2.5 cm on each side, the confined core dimensions are:

$$l_0 = l_c - 2 \times 2.5 = 70 \text{ cm} \qquad b_0 = b_c - 2 \times 2.5 = 25 \text{ cm} \tag{III.49}$$

Since $l_c = 75$ cm $> \max(2b_w;\ 0.2l_w) = \max(60;\ 47) = 60$ cm, the thickness of the boundary element must satisfy:

$$b_c \geq \frac{h_e}{10} \quad \text{with a strict minimum of 200 mm} \tag{III.50}$$

We choose $b_c = 0.3$ m, as illustrated in Figure III.12.

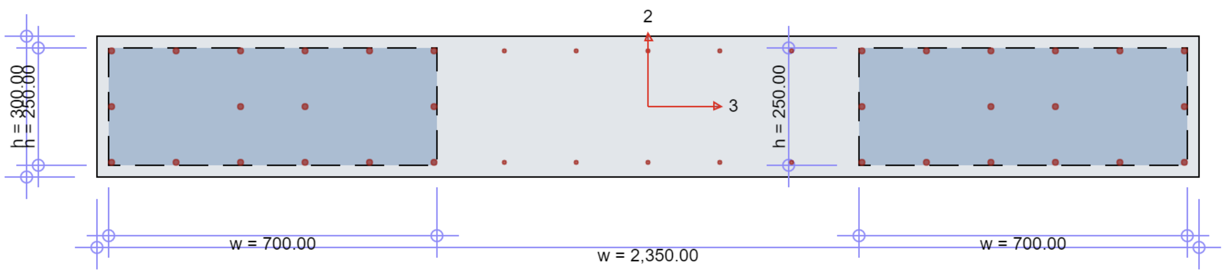

Figure III.12: Shear wall cross-section illustrating the confined zones.

The minimum longitudinal steel area required by the RPA in the confined boundary zones is:

$$A_{s,min} = 0.5\% \times (b_c \times l_c) \tag{III.51}$$

$$A_{s,min} \geq 0.5\% \times (30 \times 75) = 11.25 \text{ cm}^2 \tag{III.52}$$

Through combined axial and bending calculations using CSICOL, we determined that an arrangement of **14HA12** per boundary zone (15.83 cm^2 $> A_{s,min} = 11.25$ cm^2)—yielding a total of 28HA12 for both confined zones—along with **10HA8** in the web (5 per face), produces the interaction results presented in Figure III.13:

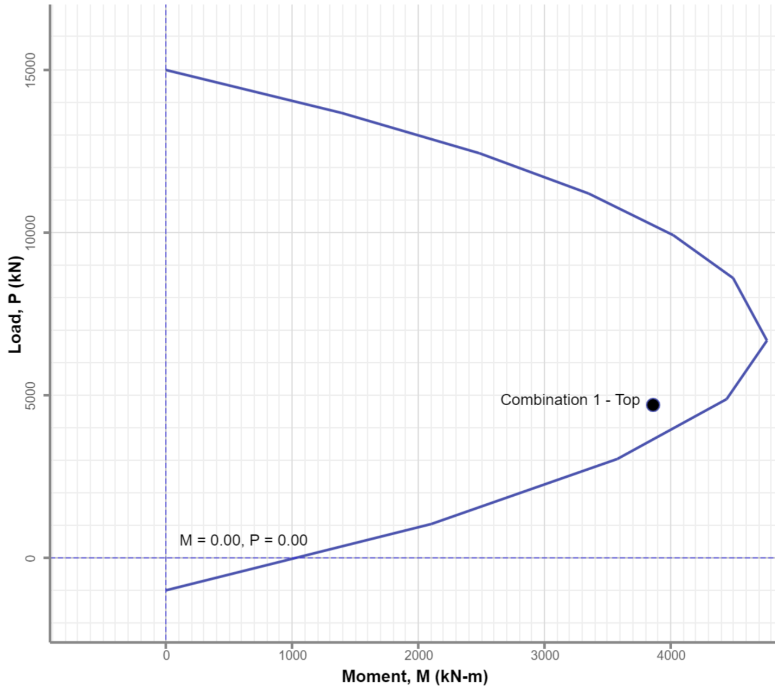

Figure III.13: CSICOL interaction curve and capacity results for the selected reinforcement.

This is a satisfactory design with a maximum capacity ratio of **0.90**.

The design shear force is evaluated as $\bar{V} = 1.4V_u$ according to the RPA 2024:

$$\bar{V} = 1.4 \times 474.36 = 664.10 \text{ kN} \tag{III.53}$$

Stirrup Configuration in the Confined Boundary Elements. The RPA 2024 mandates that the horizontal distance between two consecutively tied vertical bars must not exceed **20 cm**, and all ties must be closed stirrups.

The 14 HA12 bars in each boundary zone are arranged as follows:

- 6 bars on the top face and 6 bars on the bottom face, with a center-to-center spacing of:

$$s_{\text{bars}} = \frac{l_0}{n-1} = \frac{70}{5} = 14 \text{ cm} \tag{III.54}$$

- 1 bar at mid-height on the far-left side ($x = 0$)

- 1 bar at mid-height on the far-right side ($x = 70$ cm)

The adopted transverse reinforcement layout consists of **3 closed hoops per layer**: one outer rectangular hoop and two internal hexagonal hoops, as detailed in Figure III.14.

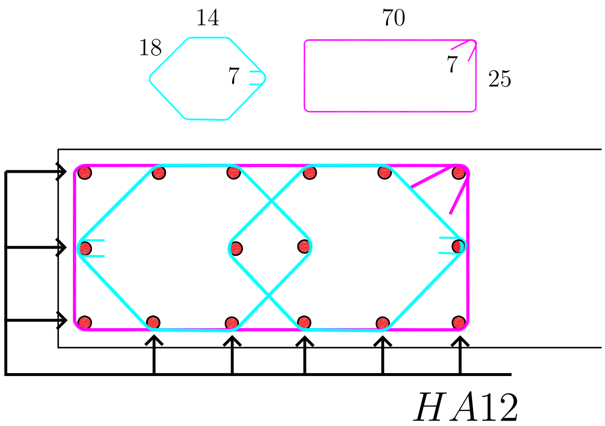

Figure III.14: Confined boundary zone horizontal and vertical reinforcement details.

This arrangement places every vertical bar at a hoop corner, restricting the maximum distance between consecutively tied bars to exactly $s = 14$ cm < 20 cm. **Verified.**

The total length of transverse steel per layer is calculated as follows:

- **Outer rectangular hoop** enclosing the full 70×25 cm core:

$$L_{\text{rect}} = 2 \times (70 + 25) + 2 \times 7 = 204 \text{ cm} \tag{III.55}$$

- **Two hexagonal hoops**, each with two flat sides of 14 cm, four slanted sides of 18 cm, and two anchorage hooks of 7 cm:

$$L_{\text{hex}} = 2 \times 14 + 4 \times 18 + 2 \times 7 = 114 \text{ cm} \tag{III.56}$$

- **Total length per layer:**

$$L = L_{\text{rect}} + 2 \times L_{\text{hex}} = 204 + 2 \times 114 = 432 \text{ cm} \tag{III.57}$$

The vertical spacing of the stirrups must satisfy:

$$s_t \leq \min\left(\frac{b_0}{3};\ 12.5 \text{ cm};\ 6\phi_l\right) \tag{III.58}$$

Where:

- $b_0 = 25$ cm is the width of the confined core
- $\phi_l = 12$ mm is the minimum diameter of the longitudinal steel in the confined zone

$$s_t \leq \min\left(\frac{25}{3};\ 12.5;\ 6 \times 1.2\right)\ \text{cm} \tag{III.59}$$

$$s_t \leq 7.2\ \text{cm} \tag{III.60}$$

We adopt a vertical spacing of $s_t = 7$ cm.

The transverse steel area in the confined boundary elements must satisfy:

$$A_t \geq 0.09 \times s_t \times b_0 \times \frac{f_{c28}}{f_e} \tag{III.61}$$

$$A_t \geq 0.3 \times s_t \times b_0 \times \left(\frac{A_g}{A_c} - 1\right) \times \frac{f_{c28}}{f_e} \tag{III.62}$$

Given $A_g = b_c \times l_c = 30 \times 75 = 2250\ \text{cm}^2$ and $A_c = b_0 \times l_0 = 25 \times 70 = 1750\ \text{cm}^2$, the ratio is $A_g/A_c = 1.286$.

$$A_t \geq \max \begin{cases} 0.09 \times 7 \times 25 \times \dfrac{30}{500} = 0.95\ \text{cm}^2 \\ 0.3 \times 7 \times 25 \times 0.286 \times \dfrac{30}{500} = 0.90\ \text{cm}^2 \end{cases} \tag{III.63}$$

$$A_t \geq 0.95\ \text{cm}^2 \tag{III.64}$$

The outer rectangular hoop provides 2 legs crossing the failure plane, and each hexagonal hoop provides 2 legs, resulting in a total of **6 legs of HA8**:

$$A_t = 6 \times 0.503 = 3.02\ \text{cm}^2 > 0.95\ \text{cm}^2 \quad \checkmark \tag{III.65}$$

Web Reinforcement – Vertical. The vertical web reinforcement diameter limits according to the RPA 2024 are:

$$8\ \text{mm} \leq \phi_{max} \leq \frac{b_w}{8} \tag{III.66}$$

We select $\phi = 8$ mm.

The maximum allowed spacing is:

$$s_v \leq \min(1.5b_w;\ 250\text{ mm};\ 25\phi_{max}) \tag{III.67}$$

$$s_v \leq 200\text{ mm} \tag{III.68}$$

We adopt a spacing of $s_v = 15$ cm.

The length of the web is:

$$l_{\text{web}} = l_w - 2 \times l_c = 235 - 2 \times 75 = 85\text{ cm} \tag{III.69}$$

With $s_v = 15$ cm, we accommodate 5 vertical bars per face (10HA8 total) in the web:

$$A_{sv} = 10 \times 0.503 = 5.03\text{ cm}^2 \tag{III.70}$$

The minimum required vertical reinforcement ratio in the web is 0.2%:

$$A_{v,min} = 0.2\% \times s_v \times b_w = 0.2\% \times 15 \times 30 = 0.9\text{ cm}^2 \tag{III.71}$$

$$5.03\text{ cm}^2 > 0.9\text{ cm}^2 \quad \checkmark \tag{III.72}$$

Shear Stress Verification.

$$\tau_b = \frac{\bar{V}}{b_0 \times d} = \frac{664.10}{0.25 \times (0.9 \times 2.35)} = 1.25\text{ MPa} < 0.2 f_{c28} = 6\text{ MPa} \quad \checkmark \tag{III.73}$$

Web Reinforcement – Horizontal. To resist the shear forces applied to the pier, the horizontal web reinforcement must satisfy the RPA 2024 requirement:

$$\frac{A_h}{s_h} \geq \frac{\bar{V}}{z \times f_e} \tag{III.74}$$

$$A_h \geq \frac{s_h \times \bar{V}}{z \times f_e} \tag{III.75}$$

Using $z = 120$ cm, $s_h = 20$ cm, and $\bar{V} = 664.10$ kN:

$$A_h \geq \frac{0.20 \times 664.10}{0.12 \times 500} = 2.21\text{ cm}^2 \tag{III.76}$$

The minimum required horizontal reinforcement ratio in the web is 0.2%:

$$A_{h,min} = 0.2\% \times s_h \times b_w = 0.2\% \times 20 \times 30 = 1.2 \text{ cm}^2 \tag{III.77}$$

We select **2HA12** at every 20 cm spacing, providing:

$$A_h = 2 \times 1.131 = 2.26 \text{ cm}^2 > 2.21 \text{ cm}^2 \quad \checkmark \tag{III.78}$$

Local Ductility Condition Justification. For shear walls with a rectangular cross-section, the mechanical volumetric ratio of required confinement reinforcement ($_{wd}$) in the boundary elements must exceed 0.12 and satisfy:

$$\alpha_{wd} \geq 30\mu_\phi \times (\nu_d + _v) \times \varepsilon_{sy,d} \frac{b_c}{b_0} - 0.035 \tag{III.79}$$

Where:

$$_{wd} = \frac{\text{Volume of confinement reinforcement}}{\text{Volume of the concrete core}} \cdot \frac{f_{yd}}{f_{cd}} \tag{III.80}$$

Given:

$$\frac{f_{yd}}{f_{cd}} = \frac{f_e \cdot \gamma_b}{f_{c28} \cdot \gamma_c} = \frac{500 \times 1.2}{30 \times 1} = 20 \qquad \varepsilon_{sy,d} = \frac{f_e}{E_s} = \frac{500}{200000} = 2.5 \times 10^{-3} \tag{III.81}$$

Volume of Confinement Reinforcement (V_s):

$$V_s = L \times \left(\pi \cdot \frac{\phi_t^2}{4}\right) \times N_{br} \tag{III.82}$$

Where $\phi_t = 8$ mm (HA8 stirrups) and the previously computed length $L = 432$ cm. N_{br} represents the number of stirrup layers along the critical height h_{cr}:

$$N_{br} = \frac{h_{cr} - 10}{s_t} = \frac{470 - 10}{7} = 65 \tag{III.83}$$

$$V_s = 432 \times \left(\pi \cdot \frac{0.8^2}{4}\right) \times 65 = 432 \times 0.503 \times 65 = 14{,}124 \text{ cm}^3 \tag{III.84}$$

Volume of the Confined Concrete Core (V_c):

$$V_c = h_{cr} \times b_0 \times l_0 = 470 \times 25 \times 70 = 822{,}500 \text{ cm}^3 \tag{III.85}$$

Mechanical Volumetric Ratio:

$$ _{wd}= \frac{V_s}{V_c} \times \frac{f_{yd}}{f_{cd}} = \frac{14{,}124}{822{,}500} \times 20 = 0.343 > 0.12 \quad \checkmark \tag{III.86}$$

Normalized Ratio of Vertical Web Reinforcement ($_v$):

$$ _{v}= \frac{A_{sv}}{(l_w - 2 \times l_c) \cdot b_w} = \frac{5.03}{85 \times 30} = 0.00197 \tag{III.87}$$

Confinement Effectiveness Factor (α):

$$\begin{cases} \alpha_n = 1 - \sum\limits_n \left(\dfrac{b_i^2}{6\, b_0\, h_0} \right) \\ \alpha_s = \left(1 - \frac{s_t}{2b_0}\right)\left(1 - \frac{s_t}{2h_0}\right) \end{cases} \tag{III.88}$$

With the adopted stirrup layout, all 14 bars are situated at hoop corners. The free lengths b_i between consecutively tied bars are:

- Along the top and bottom faces (6 bars, resulting in 5 gaps of 14 cm on each face): $10 \times b_i = 14$ cm
- Along each side face (a mid-height bar divides the 25 cm height into two equal segments): $4 \times b_i = 12.5$ cm

$$\sum_n b_i^2 = 10 \times 14^2 + 4 \times 12.5^2 = 1960 + 625 = 2585 \text{ cm}^2 \tag{III.89}$$

Using $b_0 = 25$ cm and $h_0 = 70$ cm:

$$\alpha_n = 1 - \frac{2585}{6 \times 25 \times 70} = 1 - \frac{2585}{10500} = 0.754 \tag{III.90}$$

$$\alpha_s = \left(1 - \frac{7}{2 \times 25}\right)\left(1 - \frac{7}{2 \times 70}\right) = 0.86 \times 0.95 = 0.817 \tag{III.91}$$

$$\alpha = \alpha_n \cdot \alpha_s = 0.754 \times 0.817 = 0.616 \tag{III.92}$$

Curvature Ductility Factor (μ_ϕ):

$$\mu_\phi = \begin{cases} 2 \cdot \left(\frac{R}{Q_F} \cdot \frac{M_{Ed}}{M_{Rd}} \right) - 1 & \text{if } T_0 \geq T_2 \\ 1 + 2 \cdot \left[\left(\frac{R}{Q_F} \cdot \frac{M_{Ed}}{M_{Rd}} \right) - 1 \right] \cdot \frac{T_2}{T_0} & \text{if } T_0 < T_2 \end{cases} \tag{III.93}$$

We have $R = 4.5$, $Q_F = 1.25$, $T_0 = 0.85$ s, and $T_2 = 0.6$ s. Since $T_0 > T_2$:

The capacity ratio M_{Ed}/M_{Rd} obtained from CSICOL is **0.90**.

$$\mu_\phi = 2 \times \left(\frac{4.5}{1.25} \times 0.90 \right) - 1 = 2 \times 3.24 - 1 = 5.48 \tag{III.94}$$

Neutral Axis Depth (χ_u):

$$\chi_u = (\nu_d {+}_v) \cdot \frac{l_w \cdot b_c}{b_0} = (0.22 + 0.00197) \times \frac{235 \times 30}{25} = 0.22197 \times 282 = 62.60 \text{ cm} \tag{III.95}$$

Ultimate Confined Compressive Strain ($\varepsilon_{cu,c}$):

$$\varepsilon_{cu,c} = 0.0035 + 0.1 \cdot \alpha \cdot_{wd} = 0.0035 + 0.1 \times 0.616 \times 0.343 = 0.02463 \tag{III.96}$$

Calculated Compressed Length of Boundary Elements ($l_{c,\textbf{calculated}}$):

$$l_{c,\text{calculated}} = \chi_u \cdot \left(1 - \frac{\varepsilon_{cu}}{\varepsilon_{cu,c}} \right) \tag{III.97}$$

$$= 62.60 \times \left(1 - \frac{0.0035}{0.02463} \right) = 62.60 \times 0.8579 = 53.70 \text{ cm} \tag{III.98}$$

$$l_{c,\text{calculated}} = 53.70 \text{ cm} > \max(0.15\, l_w;\ 1.5\, b_w) = \max(35.25;\ 45) = 45 \text{ cm} \quad \checkmark \tag{III.99}$$

Furthermore, $l_{c,\text{calculated}} = 53.70$ cm $< l_c = 75$ cm, which confirms that the chosen boundary element length fully contains the compressed region. **Verified.**

Final Local Ductility Check:

$$\alpha_{wd} \geq 30\mu_\phi \times (\nu_d {+}_v) \times \varepsilon_{sy,d} \frac{b_c}{b_0} - 0.035 \tag{III.100}$$

$$0.616 \times 0.343 \geq 30 \times 5.48 \times (0.22 + 0.00197) \times 2.5 \times 10^{-3} \times \frac{30}{25} - 0.035 \tag{III.101}$$

$$0.211 \geq 0.110 - 0.035 \tag{III.102}$$

$$0.211 \geq 0.075 \quad \checkmark \tag{III.103}$$

With all local ductility constraints and stress conditions fully verified, the adopted longitudinal and transverse reinforcement layout ensures that the shear walls can sustain significant inelastic deformations without sudden strength degradation. This robust detailing satisfies the stringent confinement requirements of the RPA 2024, concluding the structural sizing and establishing a resilient baseline model for the subsequent structural health monitoring investigations.

4 SENSOR NETWORK AND FEATURE EXTRACTION

This chapter details the methodology for instrumenting the structure and extracting damage-sensitive features. First, the optimal number and placement of sensors are determined through a Genetic Algorithm (GA) guided by modal information (Section 4.1). The resulting sensor layout is presented (Section 4.2), followed by the identification of the critical structural zones where damage is physically most consequential (Section 4.3). The chapter then describes how structural degradation is numerically simulated within the finite element model (Section 4.4) and concludes with the construction of the flexibility-based damage indicator that serves as the input feature vector for the machine learning model (Section 4.5).

4.1 Sensor Number and Placement Optimization (SNPO)

4.1.1 Problem Statement

A key challenge in vibration-based Structural Health Monitoring (SHM) is determining *where* and *how many* sensors to deploy on a structure. An excessive number of sensors increases cost and data-processing complexity, while too few sensors may fail to capture the modal behaviour needed for damage detection. The Sensor Number and Placement Optimization (SNPO) problem seeks the minimal set of sensor locations that preserves the ability to distinguish the structure's mode shapes.

4.1.2 Modal Assurance Criterion (MAC)

The distinguishability of mode shapes at a given sensor configuration is quantified through the **Modal Assurance Criterion** (MAC). For two mode shape vectors ϕ_i and ϕ_j, the MAC is defined as:

$$\mathrm{MAC}_{ij} = \frac{\left|\phi_i^\top \phi_j\right|^2}{\left(\phi_i^\top \phi_i\right)\left(\phi_j^\top \phi_j\right)} \tag{IV.1}$$

where $\mathrm{MAC}_{ij} \in [0,1]$. A value of 1 indicates identical mode shapes, while a value close to 0 indicates that the two modes are linearly independent. An ideal sensor configuration produces a MAC matrix that is close to the identity matrix, meaning diagonal entries are equal to 1 and all off-diagonal entries are close to 0.

4.1.3 Genetic Algorithm Formulation

The SNPO is inherently a combinatorial optimisation problem. From a pool of N_{cand} candidate sensor locations distributed across the structure, the algorithm must select an optimal subset. A **Genetic Algorithm (GA)** is employed because of its ability to efficiently explore large, discrete search spaces without requiring gradient information.

Chromosome encoding. Each individual solution in the GA population is represented as a fixed-length integer vector of size N_{cand}. Each gene contains either the index of a selected candidate sensor or the value -1 to indicate an inactive or unused sensor slot. This encoding allows the GA to simultaneously optimise both the *number* and the *placement* of sensors.

Fitness function. The fitness function evaluates how well a candidate sensor configuration distinguishes the first n_m mode shapes of the structure. Given a candidate solution with n_s active sensors, the mode shape tensor $\Phi \in \mathbb{R}^{n_m \times 3 \times n_s}$ (containing translational displacements in three degrees of freedom) is reshaped to $\Phi_{\text{flat}} \in \mathbb{R}^{n_m \times 3n_s}$ and the MAC matrix is computed. The fitness is defined as:

$$f = \frac{1}{\sqrt{\sum_{\substack{i,j=1 \\ i \neq j}}^{n_m} \text{MAC}_{ij}}} \cdot \frac{1}{1 + n_s/N_{\text{cand}}} \tag{IV.2}$$

The first factor rewards configurations that minimise off-diagonal MAC values, which leads to better mode distinguishability. The second factor acts as a *sparsity penalty* that encourages solutions with fewer active sensors.

GA operators. The GA is configured with the following operators and parameters:

- **Population size:** 100 individuals, initialised with a custom routine that randomly activates a variable number of gene slots per individual.
- **Parent selection:** Steady-State Selection (`sss`), retaining the best parent across generations.
- **Crossover:** Single-point crossover.
- **Mutation:** Random mutation applied to 20% of genes per offspring.
- **Number of generations:** 100.

The GA operates on $n_m = 12$ mode shapes extracted from the undamaged finite element model.

4.1.4 Algorithm Overview

The complete SNPO procedure is summarised in Algorithm 1.

Algorithm 1 Sensor Number and Placement Optimization (SNPO)

Require: Candidate sensor pool (coordinates and IDs), mode shape tensor Φ
Ensure: Optimal sensor subset $\mathscr{S}^*$
Extract mode shapes: Run modal analysis on the undamaged FE model and retrieve the first $n_m = 12$ mode shapes at all N_{cand} candidate locations.
Build mode shape tensor: Reshape the extracted displacements into $\Phi \in \mathbb{R}^{n_m \times 3 \times N_{\text{cand}}}$.
Initialise GA population: Generate 100 individuals, each a vector of length N_{cand} with a random number of active sensor indices and the remainder set to -1.
for generation $g = 1$ **to** 100 **do**
  for all individuals in population **do**
    Extract active sensor indices from the chromosome.
    Sub-select mode shapes: $\Phi_{\text{sub}} \leftarrow \Phi_{\text{active}}$.
    Compute the MAC matrix from Φ_{sub} (Eq. IV.1).
    Evaluate fitness f (Eq. IV.2).
  end for
  Apply selection, crossover, and mutation operators.
end for
Return the best individual $\mathscr{S}^*$ and its corresponding sensor IDs.

4.2 Sensor Network Layout

The GA-based SNPO procedure converged to an optimal configuration of **20 sensors** distributed across the 10 storey levels of the structure. The selected sensor locations are the joint nodes that best preserve mode shape distinguishability, as measured by the MAC-based fitness function (Eq. IV.2).

Because the optimisation is performed on the *true mode shapes* of the undamaged structure (extracted directly from the calibrated finite element model) the resulting layout inherently captures the dominant modal deformation patterns. Sensors are preferentially placed at locations of high modal displacement amplitude or at points where different modes exhibit contrasting displacement directions, since these locations contribute the most to minimising off-diagonal MAC values.

The optimised sensor network layout is presented in Figure IV.1. Each subplot corresponds to one floor level of the structure. Grey dots represent the full candidate sensor pool, and red dots indicate the sensors selected by the GA.

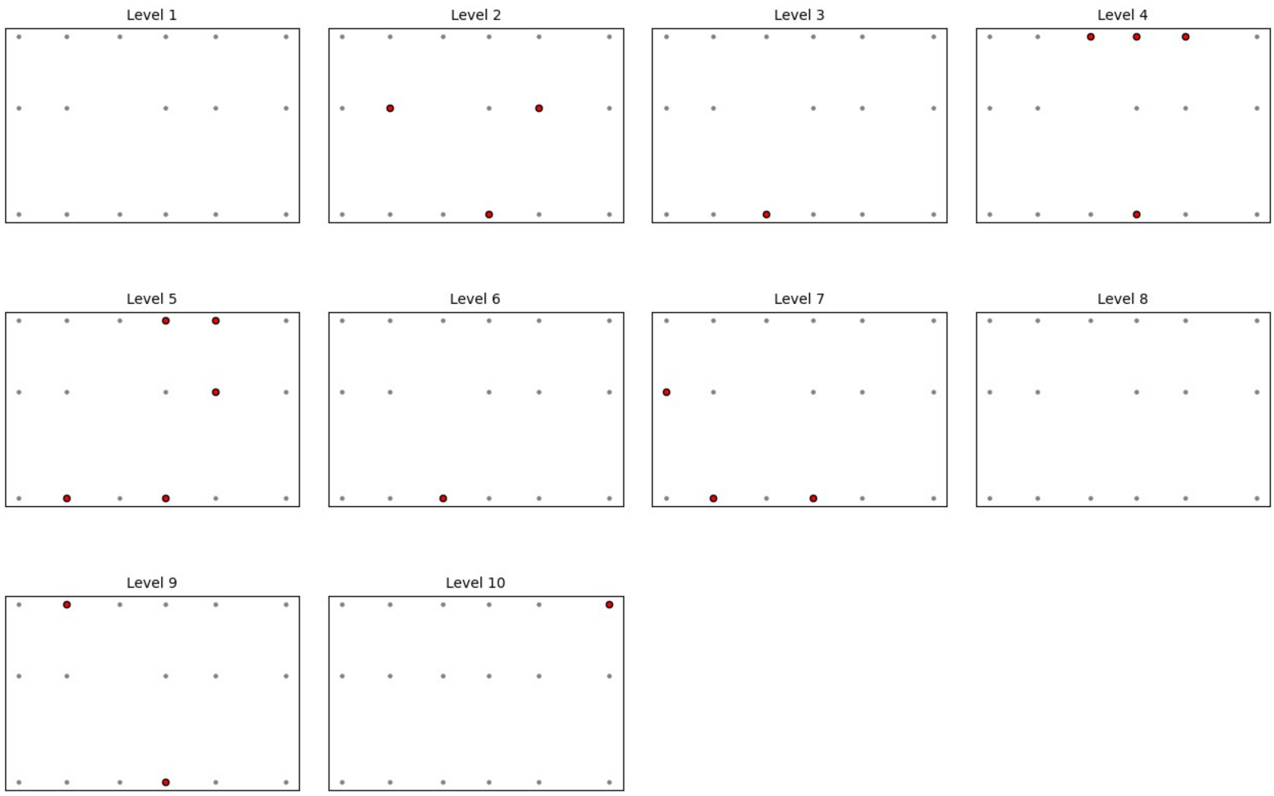

Figure IV.1: Optimised sensor placement across the 10 storey levels of the structure. Grey dots: candidate sensor pool. Red dots: sensors selected by the GA. The layout was obtained by optimising mode shape distinguishability (MAC) using the true undamaged mode shapes from the FE model.

The distribution of sensors across levels is non-uniform, reflecting the modal characteristics of the structure. Lower storeys (e.g. Levels 1 and 3) receive no sensors because their modal displacements are small relative to the upper storeys, contributing negligibly to mode differentiation. Conversely, levels with pronounced modal activity, particularly the mid-height and upper storeys, receive multiple sensors to capture the spatial variation of the dominant modes.

4.3 Identification of Critical Damage Zones

To ensure the machine learning dataset reflects physically realistic seismic degradation, the structural damage was constrained to the most heavily loaded boundary elements within the plastic hinge region (h_{cr}). Rather than applying damage to arbitrary, isolated 2D wall panels that contribute minimally to the global stiffness matrix, three critical macro-assemblies were identified: the **central U-core** (Zone 1) and the two **extreme perimeter corners** (Zones 2 and 3) (see Figure IV.2).

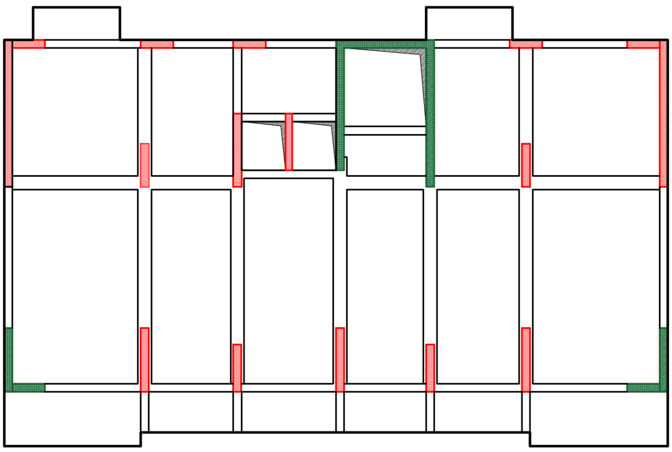

Figure IV.2: The selected assemblies as damage zones (in green)

4.3.1 Validation Through Base Shear Distribution

To mathematically validate the selection of these assemblies as the primary targets for damage simulation, a linear base shear distribution analysis was performed using the pier forces from the finite element model. Because complex 3D assemblies such as U-cores experience significant orthogonal shear forces due to torsional coupling under unidirectional seismic loading, the contribution of each zone was evaluated using the **resultant shear force vector**:

$$V_{\text{res}} = \sqrt{V_x^2 + V_y^2} \tag{IV.3}$$

The total resultant base reactions under the two equivalent static seismic load cases are:

- E_x direction: $V_{\text{res}}^{(E_x)} = \sqrt{9663.1^2 + 746.1^2} = 9691.8$ kN
- E_y direction: $V_{\text{res}}^{(E_y)} = \sqrt{746.1^2 + 12662.4^2} = 12684.4$ kN

The base shear distribution across the three critical macro-assemblies is summarised in Table IV.1.

Table IV.1: Resultant base shear distribution across critical macro-assemblies.

Structural Element	$V_{\mathbf{res}}^{(E_x)}$ **(kN)**	**% of E_x**	$V_{\mathbf{res}}^{(E_y)}$ **(kN)**	**% of E_y**
Zone 1 (U-Core)	4919.4	50.7%	4186.8	33.0%
Zone 2 (Left Corner)	1271.1	13.1%	645.5	5.1%
Zone 3 (Right Corner)	1239.3	12.8%	521.9	4.1%
Total Captured	**7429.8**	**76.6%**	**5354.2**	**42.2%**
Total Base Reaction	*9691.8*	*100.0%*	*12684.4*	*100.0%*

4.3.2 Interpretation

As demonstrated in Table IV.1, these three isolated assemblies account for a dominant **76.6%** of the entire structure's lateral resistance under the E_x seismic combination. The central U-core alone anchors over half of the primary building stiffness, while the two extreme perimeter corners provide essential torsional resistance.

By defining these macro-assemblies as the designated damage zones, any simulated stiffness degradation will result in a substantial, global shift in the fundamental modal frequencies. This ensures that the generated flexibility-based damage indicators contain a robust and physically meaningful signal-to-noise ratio. It effectively mitigates the risk of *modal masking*, a phenomenon that occurs when minor, non-critical wall panels undergo localised damage that is insufficiently detectable through global modal parameters.

4.4 Simulation of Structural Degradation

4.4.1 Physical Basis for Stiffness Reduction

The three critical zones identified in Section 4.3 are composed of **ductile reinforced concrete elements**, such as shear walls and boundary elements, that are designed to undergo controlled plastic deformation during seismic events. In ductile elements, cyclic inelastic loading leads to progressive micro-cracking, bond degradation, and concrete crushing. The macroscopic consequence of this accumulated damage is a measurable **reduction in the effective Young's modulus** E of the material, which directly reduces the element's stiffness contribution to the global structural system.

Accordingly, damage is simulated in the finite element model by reducing the Young's modulus of the concrete material assigned to each zone. For a given zone k with undamaged modulus E_0, a *severity factor* $s_k \in [0, 0.85]$ is applied such that the damaged modulus becomes:

$$E_k^{\text{damaged}} = E_0 \cdot (1 - s_k) \tag{IV.4}$$

where $s_k = 0$ represents the undamaged state and $s_k = 0.85$ corresponds to an 85% stiffness loss. The undamaged Young's modulus is $E_0 = 32{,}836.6$ MPa, corresponding to C30/37 concrete as defined in the model.

4.4.2 Damage Scenario Generation

To create a comprehensive training dataset for the machine learning model, a parametric study was conducted by systematically varying the severity factors across all three zones. The severity values are sampled from a discrete grid:

$$s_k \in \{0.00,\ 0.05,\ 0.10,\ \ldots,\ 0.85\} \tag{IV.5}$$

with a step size of $\Delta s = 0.05$, yielding 18 possible severity levels per zone. The full combinatorial space across three zones amounts to $18^3 = 5{,}832$ possible combinations. From this space, **5,000 unique combinations** were randomly sampled to form the master damage array.

Each row of the master array defines a damage scenario $\mathbf{s} = [s_1, s_2, s_3]$ specifying the severity factor for Zone 1 (U-Core), Zone 2 (Left Corner), and Zone 3 (Right Corner), respectively.

4.5 Feature Extraction: Flexibility-Based Damage Indicator

4.5.1 Modal Flexibility Matrix

The core feature extraction mechanism relies on the **modal flexibility matrix**, which approximates the structure's static flexibility using its dynamic (modal) properties. For a structure with n_m modes, natural frequencies $_i = 2\pi f_i$, and mode shape matrix $\Phi \in \mathbb{R}^{n_{\text{DOF}} \times n_m}$ (where $n_{\text{DOF}} = 3 \times 20 = 60$ for

20 tri-axial sensors), the modal flexibility matrix is defined as:

$$\mathbf{F} = \Phi \, \mathrm{diag}\left(\frac{1}{{}^2_1}, \frac{1}{{}^2_2}, \ldots, \frac{1}{{}^2_{n_m}}\right) \Phi^\top \tag{IV.6}$$

The flexibility matrix $\mathbf{F} \in \mathbb{R}^{n_{\mathrm{DOF}} \times n_{\mathrm{DOF}}}$ has the physical interpretation that element F_{ij} represents the displacement at DOF i due to a unit force applied at DOF j. Importantly, because each term is weighted by $1/{}^2_i$, the lower-frequency modes dominate the flexibility matrix. This means that a relatively small number of modes can yield a converged and accurate approximation of the total flexibility.

4.5.2 Modal Convergence and Computational Cost

Determining the appropriate number of modes n_m to include in the flexibility calculation is a critical optimisation step. While incorporating more modes incrementally improves the accuracy of the flexibility matrix, it also significantly increases the computational cost of the eigenvalue analysis. For a dataset comprising thousands of simulated scenarios, this cost scales up drastically.

To find the optimal balance, a modal convergence study was performed. The relative error of the flexibility matrix was evaluated for different numbers of included modes, and compared against the computation time required for the analysis. The results are presented in Figure IV.3.

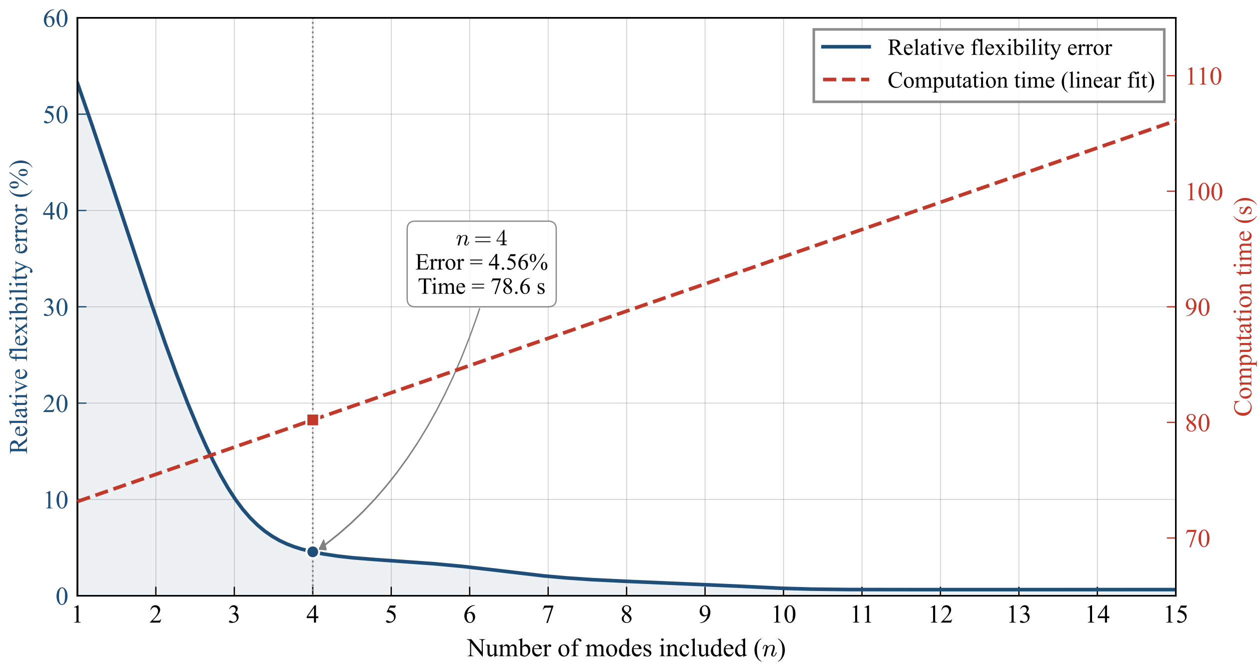

Figure IV.3: Trade-off between modal flexibility convergence error and computational cost. The analysis reveals a distinct elbow at $n_m = 4$.

As illustrated in Figure IV.3, the relative flexibility error drops sharply as the first few modes are included. By the fourth mode, the error diminishes to just 4.56%. Beyond this point, the accuracy gains become marginal, whereas the computation time continues to rise steadily. Consequently, $n_m = 4$ was selected as the optimal number of modes for the parametric study. This choice maintains a high degree of fidelity in capturing the structural behaviour while limiting the simulation time to approximately 78.6 seconds per scenario, thereby ensuring that generating the 5,000-scenario dataset remains computationally feasible.

4.5.3 Damage Indicator Construction

For each damage scenario **s**, the damage indicator vector is constructed by comparing the *damaged* flexibility matrix $\mathbf{F}^{\mathrm{d}}$ against the *undamaged* (baseline) flexibility matrix $\mathbf{F}^0$. The undamaged baseline is computed once from the intact structure (all severity factors set to zero) and stored for reuse.

The damage indicator at each degree of freedom is defined as the **maximum absolute column-wise difference**:

$$\Delta F_{\max,i} = \max_j \left| F_{ij}^{\mathrm{d}} - F_{ij}^{0} \right|, \quad i = 1, \ldots, n_{\mathrm{DOF}} \tag{IV.7}$$

This produces a vector $\Delta F_{\max} \in \mathbb{R}^{60}$ for each damage scenario, where each element quantifies the maximum change in flexibility observed at a particular sensor DOF. The resulting vector serves as the input feature vector for the neural network.

4.5.4 Rationale

The $\Delta F_{\max}$ indicator offers several advantages for SHM applications:

- **Sensitivity to stiffness changes:** Since flexibility is inversely proportional to stiffness ($\mathbf{F} \approx \mathbf{K}^{-1}$), any reduction in Young's modulus directly increases the corresponding flexibility values, making the indicator highly sensitive to damage.
- **Spatial localisation:** Each element of the $\Delta F_{\max}$ vector is associated with a specific sensor DOF, preserving spatial information about where the flexibility change is most pronounced.
- **Baseline comparison:** By computing the difference against the undamaged state, the indicator isolates the *change* caused by damage, removing the influence of the structure's inherent flexibility distribution.

The complete dataset thus consists of 5,000 input-output pairs. Each input is a 60-dimensional $\Delta F_{\max}$ vector, and each corresponding output is the three-dimensional severity vector $\mathbf{s} = [s_1, s_2, s_3]$.

5 AI ARCHITECTURE AND TRAINING RESULTS

5.1 Limitations of the Isolated Predictor in a Population Context

In conventional structural diagnostics, a supervised regression network is trained end-to-end to map a sensor measurement vector directly to a damage state. Given a complete, noise-free input $X \in \mathbb{R}^d$, such a network learns a parametric function P_ϕ such that

$$\hat{Y} = P_\phi(X), \qquad \hat{Y} \in \mathbb{R}^3, \tag{V.1}$$

where $\hat{Y}$ contains the predicted severity for each of the three structural damage zones.

While such a predictor can achieve satisfactory accuracy on the structure it was trained on, the difficulty arises when one attempts to scale it across a *population* of nominally identical buildings. In population-based SHM, what is referred to as a strongly-homogeneous population consists of structures that are pair-wise mechanically equivalent, with material, geometric, and physical parameters treated as random draws from a shared compact unimodal base-distribution [24]. Even within such a population, ambient vibration test results and the modal quantities derived from them will vary from one member to the next, owing to the natural scatter of construction materials and the influence of local environmental and operational conditions. This inter-structure variability manifests as a high-noise regime in which a predictor trained on structure A has no reliable basis for inferring the damage state of structure B, even when the two are nominally equivalent. The mapping from flexibility indicators to damage severity that the predictor learned is tied to the particular signal characteristics of its training source, and those characteristics do not transfer cleanly.

A further practical concern is sensor degradation over time. As channels fail or lose connectivity, the input dimensionality perceived by the network falls below the size it was designed to receive, and the isolated predictor, having no mechanism to handle missing entries, produces unreliable or invalid outputs. This brittleness under partial instrumentation is not a minor implementation detail; it is a fundamental limitation of the direct-mapping paradigm in any long-term monitoring deployment.

5.2 The Denoising Autoencoder as a Physics-Aware Spatial Correlator

The key observation underlying the proposed architecture is that sparse sensing is not a missing-data problem in the classical statistical sense; it is a spatial de-aliasing problem. The dynamic flexibility indicators extracted at any sensor node are not independent quantities. Because the floor slabs, columns, and shear walls of the structure form a physically coupled mechanical system, the modal response at any given degree of freedom is mathematically constrained by the responses at all neighbouring degrees of freedom through the global stiffness and mass matrices. Once the structural, environmental, and operational variability across the population is viewed as a noise-robustness challenge rather than a domain-shift problem, it becomes clear that the data occupy a latent manifold whose intrinsic dimensionality is far lower than the raw sensor count would suggest.

A Denoising Autoencoder (DAE) is designed precisely to exploit this kind of structured redundancy. Rather than training on clean inputs, the DAE is trained under deliberate corruption, forcing the network to discover and internalise the physical coupling relations that make reconstruction possible even from a degraded observation.

5.2.1 Stochastic Input Masking and Noise Injection

Let $X \in \mathbb{R}^d$ denote the pristine flexibility-indicator vector for a given damage scenario, where $d = n_{\text{dof}} = 60$ (20 optimal sensor locations $\times$ 3 DOFs per location). As introduced in Section 4.5.3, this vector explicitly comprises the maximum change in flexibility (ΔF_{max}) serving as the damage indicator at each of the optimal node locations derived from the optimal sensor placement in Chapter 4. Mathematically, the input vector X is defined as:

$$X = \begin{bmatrix} \Delta F_{\text{max},1} \\ \vdots \\ \Delta F_{\text{max},i} \\ \vdots \\ \Delta F_{\text{max},n_{\text{dof}}} \end{bmatrix} \tag{V.2}$$

To bridge the gap between an isolated structural model and a population-level deployment, an additive noise vector $\varepsilon \in \mathbb{R}^d$ is introduced. Rather than solely simulating sensor measurement uncertainties, this noise term is sampled from a zero-mean Gaussian distribution $\varepsilon \sim \mathcal{N}(0, \sigma^2 I)$ to act as a direct mathematical surrogate for inter-structure variability.

As established in Section 2.5, the cumulative effects of material scatter, geometric tolerances, and environmental fluctuations across a homogeneous population manifest statistically as Gaussian perturbations in the feature space. To rigorously justify this, consider the measured flexibility F at a specific structural degree of freedom. Let the theoretical, idealised flexibility derived from the pristine "Form" be F_0. The actual measured flexibility deviates from F_0 due to a collection of N independent, small physical perturbations across the population. Let these physical variabilities be denoted as Δ_i, which include factors such as:

- Deviations in concrete compressive strength.

- Geometrical cross-section tolerances.
- Differential thermal expansion from seasonal temperature gradients.
- Unmodeled micro-cracking due to natural concrete shrinkage.

Using a first-order Taylor series expansion, the total variation in measured flexibility $\Delta F = F - F_0$ can be approximated as the linear sum of these independent variations:

$$\Delta F \approx \sum_{i=1}^{N} \frac{\partial F}{\partial \Delta_i} \Delta_i \tag{V.3}$$

Let the weighted contribution of each variable be $X_i = \frac{\partial F}{\partial \Delta_i} \Delta_i$. Each X_i acts as an independent random variable with its own mean μ_i and variance σ_i^2. While the underlying distributions of these individual physical parameters are rarely Gaussian, the Central Limit Theorem (illustrated in Figure V.1) dictates that their sum, $S_N = \sum_{i=1}^{N} X_i$, converges to a Normal distribution as N increases:

$$S_N \sim \mathcal{N}\left(\sum_{i=1}^{N} \mu_i, \sum_{i=1}^{N} \sigma_i^2\right) \tag{V.4}$$

Because the input data is standardised in the machine learning pipeline (centering the mean at zero), the effective noise applied to the idealised Form reduces cleanly to zero-mean Gaussian noise.

To further simulate sparse instrumentation, a binary dropout mask $m \in \{0, 1\}^d$ is drawn independently for each training sample, with each element set to zero with probability p_{drop} and to one otherwise. The corrupted input presented to the network is then:

$$\tilde{X} = (X + \varepsilon) \odot m \tag{V.5}$$

By training the network under this specific corruption regime, the DAE is forced to learn a population-invariant latent space. The noise injection requires the Encoder to actively ignore the scatter that differentiates individual structures within a population, isolating only the underlying physical damage signal.

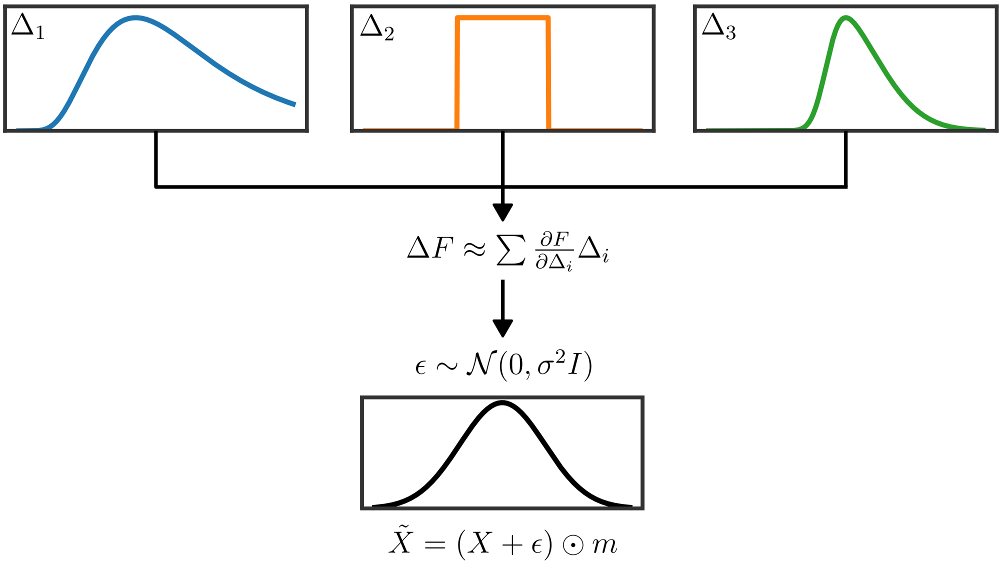

Figure V.1: Visual representation of the Central Limit Theorem demonstrating the convergence of independent structural perturbations to a Normal distribution.

5.2.2 Encoder: Compression into a Latent Physics State

The corrupted vector $\tilde{X}$ is passed through an Encoder network E_θ, which compresses it into a low-dimensional latent representation

$$Z = E_\theta(\tilde{X}), \qquad Z \in \mathbb{R}^k, \tag{V.6}$$

with $k = 16$. The Encoder is a three-layer feedforward network with `Dense–BatchNorm–ReLU` blocks of widths 46, 32, and 16, with ℓ_2 regularisation applied to all weight matrices. The bottleneck dimension $k \ll d$ is small enough that the Encoder cannot memorise individual channels; it is forced instead to learn the inter-DOF correlations that allow any missing channel to be inferred from the surviving ones, which is precisely the physical knowledge the architecture is designed to capture.

5.2.3 Decoder: Reconstruction of the Complete Spatial Field

A symmetric Decoder D_ψ maps the latent code back to an estimate of the *pristine* flexibility vector:

$$\hat{X} = D_\psi(Z), \qquad \hat{X} \in \mathbb{R}^d. \tag{V.7}$$

The Decoder mirrors the Encoder in width ($16 \to 32 \to 46 \to 60$), with a linear activation on the final layer, consistent with the unbounded range of the standardised input features. The training target for the Decoder is the pristine vector X rather than its corrupted counterpart $\tilde{X}$. Specifically, the objective function relies on MSE$(\hat{X}, X)$ instead of MSE$(\hat{X}, \tilde{X})$, since this is the central piece of the "denoising" capability in our DAE. This distinction is consequential: by penalising the Decoder for failing to recover what a missing channel *should* have measured, the network receives a considerably stronger learning signal, one that drives the Encoder toward genuinely internalising the structural physics rather than simply passing through the surviving channels (see Figure V.2).

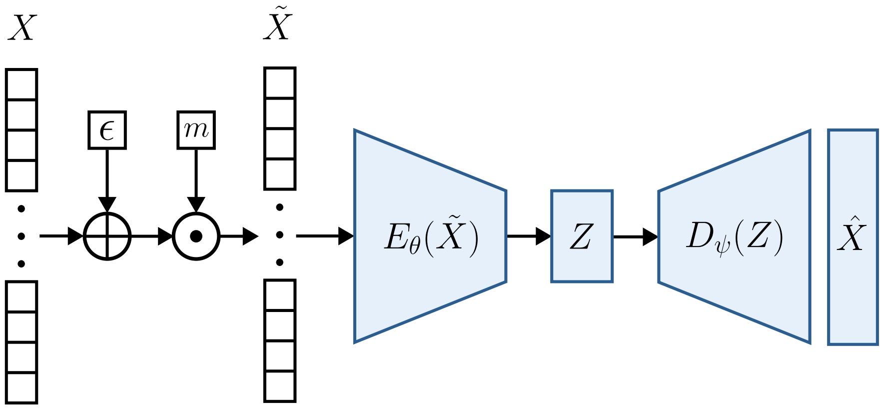

Figure V.2: Illustration of the data corruption process and the complete Denoising Autoencoder architecture (highlighted in light blue).

5.2.4 Phase-1 Model Pre-Training and Baseline Parameter Search

To comprehensively evaluate the Denoising Autoencoder's (DAE) reconstruction capabilities under various degradation scenarios, a full grid-search experiment was conducted. The DAE was trained under a self-supervised objective across a 6 Ã— 6 combinatorial grid of sensor masking (dropout) rates $p_{\text{drop}} \in \{0.0, 0.10, 0.20, 0.30, 0.40, 0.50\}$ and Gaussian measurement noise levels (from 0.0 to 0.5 standard deviations).

To quantify uncertainty, 20 independent models were trained for every configuration, with each model trained for up to 50 epochs using early stopping (patience 10). The aggregated test-set performance metrics comprising Mean MSE, Standard Deviation, and R^2 scores across all 720 trained models are summarised in Table V.1

Table V.1: Model Performance (Mean MSE $\pm$ Std MSE and R^2 Score) across Dropout (DR) and Noise Rates

DR	**Noise**											
	0.0		**0.1**		**0.2**		**0.3**		**0.4**		**0.5**	
	MSE ($\pm$ Std)	R^2	**MSE ($\pm$ Std)**	R^2	**MSE ($\pm$ Std)**	R^2	**MSE ($\pm$ Std)**	R^2	**MSE ($\pm$ Std)**	R^2	**MSE ($\pm$ Std)**	R^2
0.0	0.0036 ± 0.0003	0.9960	0.0046 ± 0.0006	0.9949	0.0061 ± 0.0004	0.9932	0.0091 ± 0.0006	0.9899	0.0125 ± 0.0008	0.9861	0.0168 ± 0.0009	0.9813
0.1	0.0054 ± 0.0006	0.9940	0.0063 ± 0.0010	0.9930	0.0080 ± 0.0008	0.9912	0.0113 ± 0.0022	0.9875	0.0136 ± 0.0011	0.9850	0.0177 ± 0.0014	0.9803
0.2	0.0429 ± 0.0464	0.9526	0.0331 ± 0.0323	0.9635	0.0404 ± 0.0471	0.9554	0.0316 ± 0.0057	0.9653	0.0346 ± 0.0037	0.9619	**0.0369 $\pm$ 0.0058**	**0.9593**
0.3	0.1181 ± 0.0749	0.8699	0.1354 ± 0.0834	0.8499	0.1263 ± 0.0777	0.8602	0.1605 ± 0.0945	0.8226	0.1466 ± 0.1006	0.8376	0.1132 ± 0.0615	0.8753
0.4	0.3342 ± 0.0872	0.6295	0.3316 ± 0.0804	0.6326	0.3151 ± 0.0909	0.6514	0.3538 ± 0.0945	0.6075	0.3806 ± 0.0931	0.5781	0.3628 ± 0.0962	0.5980
0.5	0.4403 ± 0.0866	0.5126	0.4324 ± 0.1114	0.5203	0.4660 ± 0.0872	0.4840	0.4570 ± 0.0857	0.4939	0.4721 ± 0.0919	0.4764	0.4607 ± 0.1100	0.4895

As observed in Table V.1, the architecture demonstrates a pronounced asymmetry in its robustness to the two distinct degradation modes. The model is exceptionally resilient to additive Gaussian measurement noise; even when subjected to the maximum noise level of 0.5 without any sensor dropout, the network retains a high predictive capacity with an R^2 score of 0.9813. In stark contrast, sensor dropout represents a significantly harsher perturbation to the system. At a dropout rate of 50% with zero noise, the R^2 score plummets to 0.5126, indicating that the complete loss of spatial correlation channels degrades the network's reconstruction ability much faster than channel-uncorrelated noise.

To isolate the effect of sensor masking and pinpoint the optimal pre-training operating point, a focused drop-rate sweep was analyzed, as depicted in Figure V.3. The validation reconstruction MSE boxplots (Figure V.3a) illustrate that both the median reconstruction error and the inter-run variance increase exponentially (plotted on a logarithmic scale) as the masking rate grows.

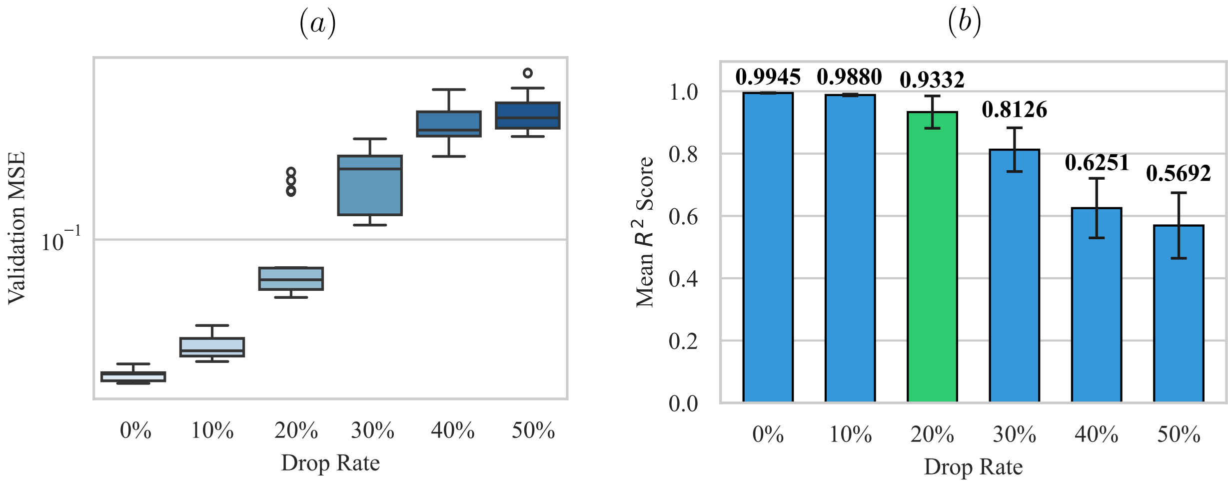

Figure V.3: Phase-1 drop-rate sweep. **a)** validation reconstruction MSE (log scale) over training epochs for each masking rate. **b)** best achieved validation MSE per rate; the selected operating point is highlighted.

The mean reconstruction R^2 scores (Figure V.3b) provide a clear, quantitative criterion for parameter selection. At low dropout rates of 0% and 10%, the reconstruction task is insufficiently challenging, with R^2 scores remaining near-perfect (above 0.9880). This low-corruption regime risks allowing the network to simply pass surviving channels through without forcing the Encoder to genuinely map the underlying physical structural correlations. Conversely, at dropout rates of 30% and beyond, performance degrades too sharply (falling to an R^2 of 0.8126 and below), meaning the essential structural signal becomes irretrievably lost.

Therefore, a dropout rate of 20% emerges as the optimal baseline parameter. At this inflection point, the model is significantly challenged to internalize the spatial physics of the structure, yet it still maintains a highly robust mean R^2 of 0.9332. Consequently, the joint configuration comprising a

20% dropout rate and a 0.5 noise level (highlighted in Table V.1, yielding an MSE of 0.0369 ± 0.0058 and an R^2 of 0.9593) is established as the target operating point. This configuration perfectly balances the aggressive corruption required to learn a population-invariant latent space with the signal retention necessary for accurate downstream severity prediction.

5.3 Dual-Branch Architecture and Pseudo-Transfer Learning

After Phase-1 pre-training, the Encoder E_θ has learned a latent space that encodes the modal physics of the structure in a form already robust to moderate sensor dropout and aggressive measurement noise.

The DAE, however, is a generative model: it can reconstruct the sensor field, but it cannot *diagnose* structural damage. A second functional branch is therefore attached to the same latent representation, transforming the architecture into a dual-output system capable of simultaneously healing the sensor field and predicting damage severity (Figure V.4). The shared latent code Z is the architectural junction between these two tasks, and it is what makes the design coherent rather than merely composite.

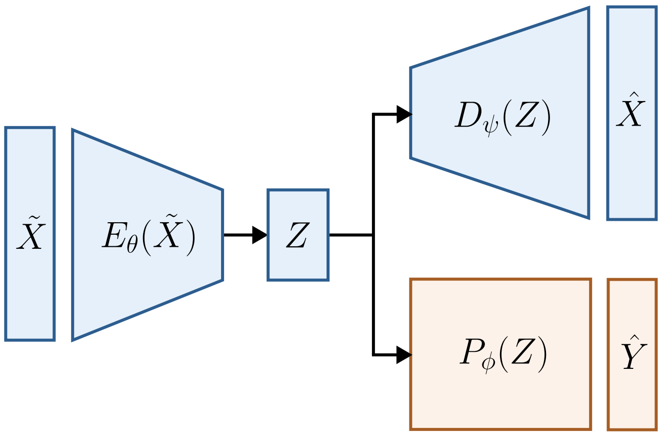

Figure V.4: The complete Dual-Branch DAE architecture. The shared latent space connects the self-supervised reconstruction task (Decoder) with the supervised diagnostic task (Predictor).

5.3.1 The Predictor Branch

A Predictor network P_ϕ maps the shared latent code Z to the three-dimensional severity vector:

$$\hat{Y} = P_\phi(Z), \qquad \hat{Y} \in \mathbb{R}^3, \tag{V.8}$$

where each component of $\hat{Y}$ is a continuous severity estimate in $[0,1]$ for one of the three structural zones. The Predictor is a compact four-layer MLP ($16 \rightarrow 16 \rightarrow 8 \rightarrow 8 \rightarrow 3$) with `ReLU` hidden activations and a `sigmoid` output layer, consistent with the bounded range of the severity targets.

The choice of an MLP for this branch is deliberate but not mandatory. Because the Predictor operates on a clean, physics-informed latent code rather than raw sensor data, the regression task it faces is substantially simpler than the original mapping from raw indicators to damage states; the Encoder has already performed the dimensionality reduction and noise suppression. Alternative prediction heads, gradient-boosted trees, Random Forest regressors, or higher-capacity nonlinear networks, can be attached to the same trained Encoder without disturbing the shared representation, simply by fitting them to the Encoder's output. This modularity provides a systematic upgrade path decoupled from the latent geometry itself.

5.3.2 Pseudo-Transfer Learning via the Shared Latent Space

The architecture realises a form of implicit transfer learning across the population without explicit domain adaptation, auxiliary domain labels, or a separate fine-tuning phase. The mechanism is as follows.

During Phase-1 training, the stochastic masking operator m samples, with positive probability, every possible sparse sub-configuration of the full sensor array. The Encoder is therefore trained to map any masked version of X to approximately the same point in z-space as the pristine X itself. This invariance is not imposed by an explicit regularisation term; it emerges organically from the reconstruction objective. The Decoder can only recover the pristine field X from a masked input if the Encoder has compressed the mask-invariant physical content, and discarded the mask-specific artefacts, into z. The latent code is thus forced to represent the underlying damage state of the structure rather than any particular sensor configuration.

When the trained system is subsequently deployed on a Type-B structure whose permanent sensor layout corresponds to one such masked sub-configuration, the Encoder maps its limited observations to the same latent manifold on which the Predictor was trained. The Predictor, drawing from this invariant representation, inherits the Encoder's robustness to missing sensors without having been explicitly exposed to sparse data during its own supervised training. The empirical confirmation of this mechanism, that the latent code z under sensor corruption remains tightly correlated with its clean counterpart, is presented in Section 5.6.3.

5.4 Phase-2 Joint Optimisation

Once the DAE has been pre-trained and the optimal corruption parameters selected, all three components, Encoder E_θ, Decoder D_ψ, and Predictor P_ϕ, are unfrozen and trained jointly in Phase 2. The full forward pass for a given input X is

$$z = E_\theta\big((X+\varepsilon)\odot m\big), \qquad \hat{X} = D_\psi(z), \qquad \hat{Y} = P_\phi(z). \tag{V.9}$$

5.4.1 Asymmetrically Weighted Objective Function

Two loss terms are defined. The *reconstruction loss* $\mathscr{L}_{\text{recon}}$ measures the fidelity of the recovered flexibility field:

$$\mathscr{L}_{\text{recon}} = \frac{1}{d}\sum_{i=1}^{d}\big(x_i - \hat{x}_i\big)^2. \tag{V.10}$$

The *prediction loss* $\mathscr{L}_{\text{pred}}$ measures the regression error of the severity estimates:

$$\mathscr{L}_{\text{pred}} = \frac{1}{3}\sum_{j=1}^{3}\big(y_j - \hat{y}_j\big)^2. \tag{V.11}$$

These are combined into a single scalar objective with asymmetric weighting:

$$\mathscr{L}_{\text{total}} = 0.1\,\mathscr{L}_{\text{recon}} + 0.9\,\mathscr{L}_{\text{pred}}. \tag{V.12}$$

The weighting reflects the structural hierarchy of the two tasks. Reconstruction is intrinsically easier: its target X is high-dimensional and continuous, and the Encoder already carries a strong prior for spatial correlation from Phase-1. Assigning a dominant coefficient of 0.9 to the prediction loss forces the joint optimisation to prioritise damage-discriminative geometry in z, while the small reconstruction coefficient of 0.1 is sufficient to prevent the spatial-correlator behaviour established in Phase-1 from being overwritten during fine-tuning. The result is a latent space that is simultaneously a good spatial reconstructor and a well-structured damage severity manifold.

5.4.2 Training Protocol

Phase-2 training proceeds for up to 300 epochs with early stopping on validation prediction loss (patience 30) and learning-rate reduction on plateau (factor 0.5, patience 15, minimum 10^{-6}). The Adam optimiser is used with an initial learning rate of 10^{-3}. A 70/15/15 train/validation/test split is applied to the 5 000-scenario dataset, with `StandardScaler` normalisation fitted exclusively on the training partition and applied without leakage to the validation and test sets.

The Phase-2 training curves are shown in Figure V.5. The Phase-1 reconstruction loss (panel a) drops sharply within the first ten epochs and stabilises near zero, confirming that the Encoder internalises the inter-DOF coupling rapidly before the fine-tuning phase begins. In Phase-2, both prediction loss and total loss converge smoothly without signs of overfitting: the train and validation curves track closely throughout, a particularly encouraging result given the relatively compact 5 000-scenario dataset.

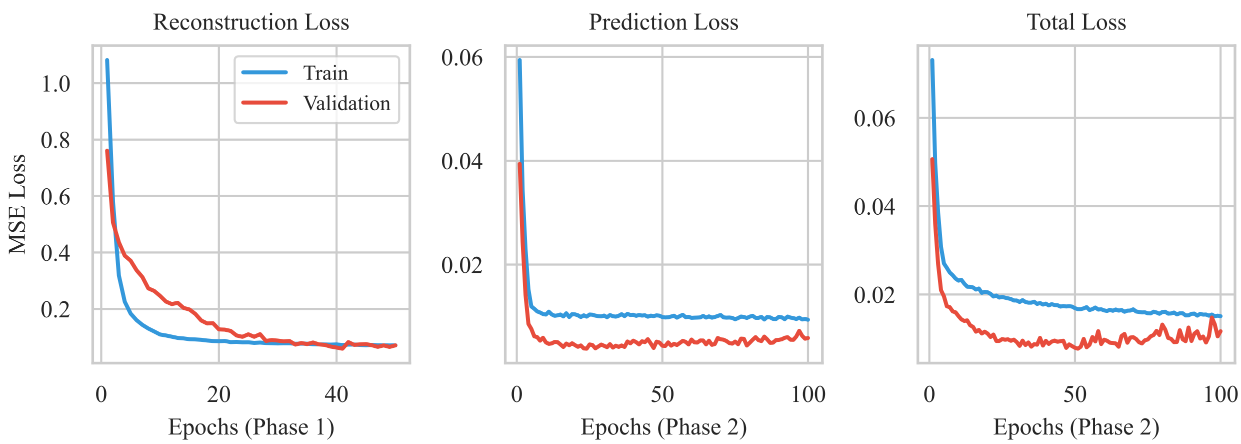

Figure V.5: Training curves for both phases. **a)** Phase-1 reconstruction MSE loss, showing rapid convergence of the Encoder–Decoder pair. **b)** Phase-2 prediction MSE. **c)** Phase-2 total weighted loss (Eq. V.12). Training (indigo) and validation (amber) curves shown.

5.5 Test-Set Results

The trained system is evaluated on the held-out test set (750 scenarios, unseen during both training phases).

5.5.1 Reconstruction Fidelity

The reconstruction branch recovers the complete 60-dimensional flexibility-indicator field from masked inputs, confirming the spatial correlator hypothesis: the structural coupling embedded in the flexibility matrix is sufficiently regular that a 16-dimensional bottleneck can capture it under realistic sensor dropout.

5.5.2 Damage Severity Prediction

Figure V.6 presents the predicted versus true severity scatter plots for the three structural damage zones on the held-out test set. All three panels show tight alignment with the identity diagonal and the vast majority of predictions fall within the ±10% bound, confirming strong generalisation to unseen damage scenarios across the full severity range.

Per-zone performance metrics are reported in Table V.2. Zones 1 and 2, corresponding to the U-core and the back-right corner shear wall, achieve R^2 values of 0.952 and 0.960 respectively, with low and stable MSE. Zone 3 (top-left corner) is the most demanding zone, yielding $R^2 = 0.935$; this modest reduction relative to the other zones is consistent with the greater geometric eccentricity of the TL corner element, whose damage signature is more susceptible to being aliased by the global torsional response of the structure. Across all zones, the prediction variance is low and systematic, with no evidence of severity-range bias.

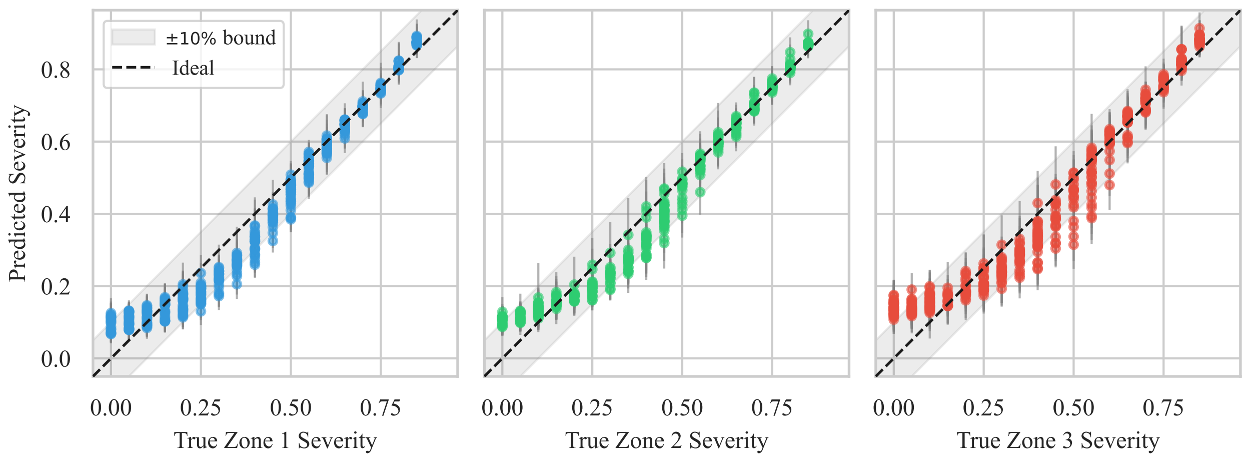

Figure V.6: Predicted vs. true damage severity on the held-out test set for each of the three structural zones. **a)** Zone 1 (U-core), **b)** Zone 2 (BR Corner), **c)** Zone 3 (TL Corner). Box distributions at each discrete severity level show the spread across the 750 test scenarios. The dashed diagonal is the ideal predictor; the shaded band marks the ±10% tolerance.

Table V.2: Test-set prediction performance for the dual-branch model.

Metric	Zone 1 (U-core)	Zone 2 (BR Corner)	Zone 3 (TL Corner)
MSE (Mean)	0.003430	0.003091	0.005226
MSE (Std Dev)	±0.000477	±0.000330	±0.000385
R^2	0.952	0.960	0.935

5.6 Test-Time Robustness and Latent Space Analysis

The operational viability of the trained system depends on its ability to maintain diagnostic accuracy under conditions that deviate from the clean, fully-instrumented deployment environment. This section evaluates the system's behaviour under two independent degradation modes, sensor dropout and additive Gaussian noise, and then interrogates the latent space geometry to explain the observed response.

5.6.1 Test-Time Sensor Dropout

In this protocol, a random fraction $p_{\text{drop}}^{\text{test}} \in \{0.0, 0.10, 0.20, 0.30, 0.40, 0.50\}$ of the 60 input channels is zeroed at test time, irrespective of the masking applied during training. The evaluation is repeated over $N = 20$ independent runs per level to obtain stable estimates of mean performance and variance.

The results, presented in Figure V.7, show gracefully stratified degradation. At $p_{\text{drop}}^{\text{test}} = 0.0$, the ensemble achieves a mean $R^2 = 0.9420$ and a median severity MAE below 0.05. As dropout increases to 0.20, matching the rate used during Phase-1 training, R^2 remains above 0.91 and the MAE interquartile range expands only modestly, reflecting the successful internalisation of inter-DOF correlations during pre-training. Beyond $p_{\text{drop}}^{\text{test}} = 0.30$, degradation accelerates; at 50% dropout, the mean R^2 falls to 0.6619 and the MAE median exceeds 0.11. Crucially, the variance across the 20 runs remains low even at this extreme level: the model fails consistently rather than catastrophically, a property of considerable importance for structural safety applications where unpredictable failure modes are more dangerous than predictable, gradual accuracy loss.

5.6.2 Test-Time Gaussian Noise

In the second protocol, the test-set inputs are perturbed by additive Gaussian noise:

$$\tilde{X}^{\text{test}} = X + \varepsilon, \qquad \varepsilon \sim \mathcal{N}\big(0,\, (\sigma_{\text{noise}} \cdot \sigma_X)^2 \cdot I\big), \tag{V.13}$$

where σ_X is the per-feature standard deviation of the training data and $\sigma_{\text{noise}} \in \{0.0, 0.10, \ldots, 0.50\}$ is the relative noise level, calibrated to the actual dynamic range of each flexibility-indicator channel.

Recall from Section 5.2.4 that Gaussian noise was established not merely as a sensor corruption model but as the mathematical surrogate for inter-structure variability within the population. The Central Limit Theorem argument of Section 5.2.1 showed that the aggregate effect of material scatter, geometric tolerances, and environmental fluctuations across a strongly-homogeneous population manifests in feature space as zero-mean Gaussian perturbations. The noise level $\sigma_{\text{noise}} = 0.50$ adopted at the target operating point (Table V.1, highlighted cell at DR = 0.20) was therefore not

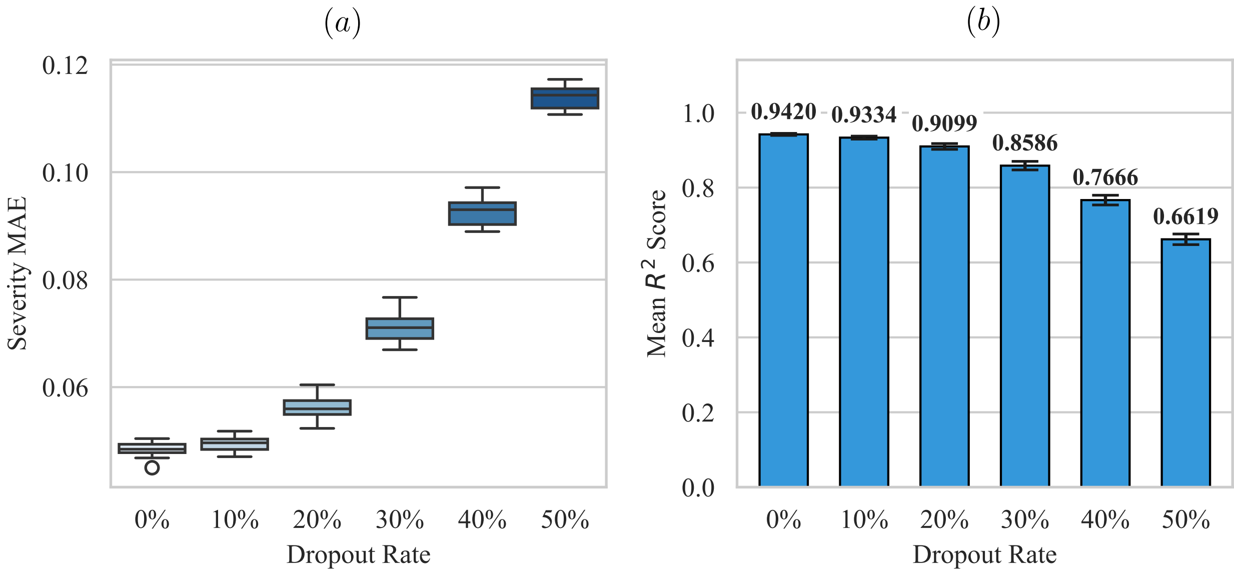

Figure V.7: Test-time sensor dropout robustness ($N = 20$ runs per level). **(a):** box plot of severity MAE across dropout rates 0%–50%. **(b):** mean test-set R^2 per dropout rate with ± 1 standard deviation error bars. The model retains $R^2 > 0.91$ up to 20% dropout, matching the Phase-1 training masking rate.

selected for reconstruction convenience; it was selected to be the dominant training challenge, deliberately exceeding any realistic single-sensor measurement error so that the Encoder is forced to treat inter-structure variability as a condition it operates under by design, not an exceptional case it must tolerate.

The test-time noise sweep thus functions as a direct evaluation of the system's *population generalisation capacity*: each noise level σ_{noise} corresponds to a different effective spread of the homogeneous population, and the question the sweep answers is whether the pipeline degrades gracefully as that spread increases beyond its training envelope.

As shown in Figure V.8, the answer is clearly affirmative. At zero noise, the ensemble achieves a mean $R^2 = 0.9420$. This value degrades only to 0.9403 at 10% noise, 0.9335 at 20%, and 0.9258 at 30%, a total loss of 0.016 across the first three noise levels, which is within the run-to-run variance at baseline. Even at the extreme $\sigma_{\text{noise}} = 0.50$, where the perturbation reaches half the signal's own standard deviation, matching and equalling the most aggressive training configuration, the mean R^2 remains at 0.8917 and the MAE median stays below 0.066. The total R^2 degradation across the full noise range is 0.050, approximately one-fifth of the 0.280 observed under the equivalent dropout sweep.

This resilience is a direct consequence of the Phase-1 and Phase-2 training regime. The grid search of Table V.1 already revealed a striking pattern at DR = 0.20: reconstruction performance is essentially flat across all noise levels, with R^2 values ranging from 0.9526 (no noise) to 0.9593 (noise = 0.50), a spread narrower than the inter-run standard deviation. The Encoder trained under this regime learned to suppress zero-mean stochastic perturbations before they reach the bottleneck, treating them as irrelevant to the latent code. Phase-2 joint training, which continued under the same $\sigma_{\text{noise}} = 0.50$ corruption schedule, reinforced this suppression in the final end-to-end system. The result is a Predictor that is insensitive to the very type of variability that makes population-based SHM hard: the building-to-building scatter that was the motivation for the DAE design from the outset.

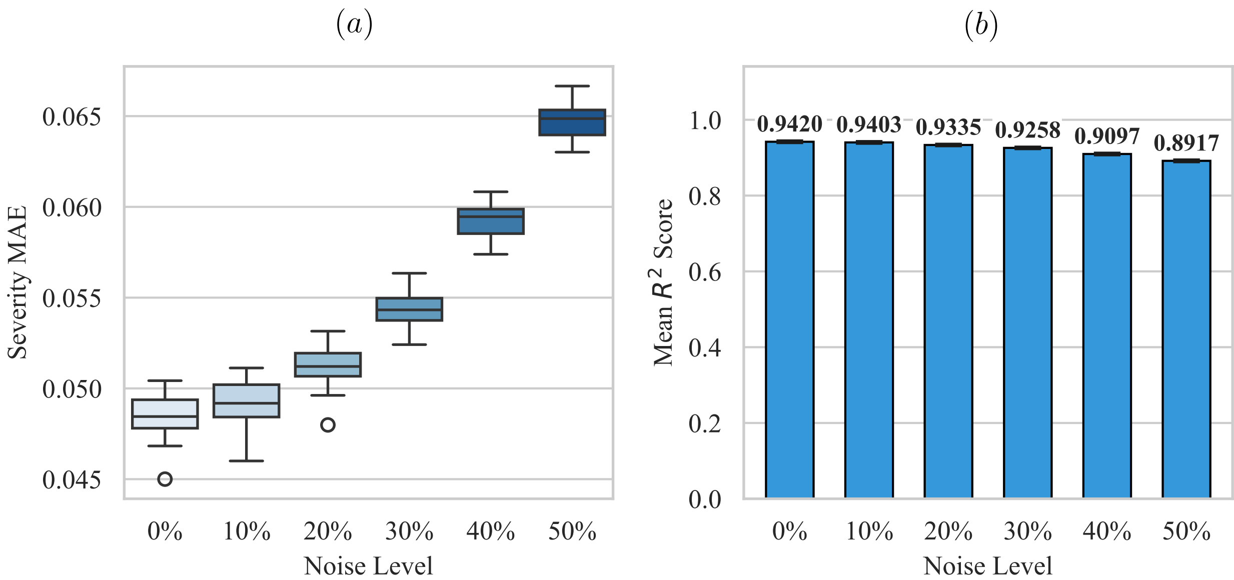

Figure V.8: Test-time Gaussian noise robustness ($N = 20$ runs per level). **(a):** box plot of severity MAE across relative noise levels 0%–50%. **(b):** mean test-set R^2 per noise level. The near-flat R^2 profile across the full sweep confirms that the $\sigma_{\text{noise}} = 0.50$ training regime has rendered the pipeline effectively insensitive to inter-structure variability across the tested population spread. Total R^2 degradation (0.050) is approximately one-fifth of that observed under the equivalent dropout sweep (0.280).

5.6.3 Latent Space Stability: Why the Pipeline Behaves This Way

The quantitative gap between dropout sensitivity and noise immunity established in Sections 5.6.1 and 5.6.2 has a precise geometric explanation in the latent space, and the cross-correlation analysis presented here makes that explanation directly visible.

For each test sample, the Encoder is run twice: once on the clean input X to obtain z_{clean}, and once on the corrupted input $\tilde{X}^{\text{test}}$ to obtain z_{corr}. The 16×16 cross-correlation matrix between the paired latent vectors is computed across the test set ($N = 405$ samples), and its mean diagonal, the

Mean Diag. metric, serves as a scalar summary of latent identity preservation: a value of 1.0 means corruption has no effect on the encoding; a value approaching 0 indicates complete decorrelation.

Gaussian noise: a latent code that corruption cannot reach. Figure V.9 presents the cross-correlation matrices under additive Gaussian noise. The Mean Diag. is 0.9987 at 10% noise and remains above 0.9720 even at the 50% level, the highest stability values recorded across any perturbation mode tested. The block structure of the correlation matrix is almost perfectly preserved up to 30% noise (Mean Diag. = 0.9886), at levels already producing a measurable increase in prediction MAE. This confirms that the latent representation is not merely numerically close to its clean counterpart: it is *semantically identical* to it. The four latent clusters, three zone-specific damage subspaces and one global stiffness mode, are entirely undisturbed by a perturbation that reaches half the signal amplitude.

The mechanism is statistical. Zero-mean Gaussian noise is channel-uncorrelated; as the corrupted signal propagates through the Encoder's dense layers, the noise contribution is averaged across all 60 input channels before reaching the 16-dimensional bottleneck. By the same Central Limit argument invoked in Section 5.2.1 to justify the Gaussian noise model in the first place, the expected noise contribution at the bottleneck scales as $\sigma_{\text{noise}}/\sqrt{d}$, which at $d = 60$ amounts to a suppression factor of approximately 7.7$\times$ relative to the per-channel noise amplitude. The training regime at $\sigma_{\text{noise}} = 0.50$ was calibrated to match and exceed this suppressed level, ensuring the Encoder never encountered a noise regime in deployment that it had not seen at training. This is why the noise robustness curve is essentially flat: the pipeline was not just tested against inter-structure variability, it was *designed* around it.

Sensor dropout: spatial information that cannot be recovered. Figure V.10 shows the equivalent matrices under sensor dropout. The Mean Diag. is 0.9901 at 10% dropout, comparable to the noise case, but decreases monotonically and more steeply, reaching 0.8936 at 50% dropout versus 0.9720 under the equivalent noise level. The contrast is physically interpretable. Dropout removes entire sensor channels, destroying the spatial correlation signal that the Encoder relies on to infer each channel's contribution to the bottleneck. No amount of averaging across surviving channels can recover the information carried by a channel that is simply absent; the CLT suppression mechanism has no equivalent here. The latent code therefore drifts from its clean counterpart in proportion to the fraction of spatial information destroyed, and the prediction performance degrades accordingly.

The block structure remains visible across all dropout panels, confirming that even under severe sensor loss the Encoder does not collapse to a random mapping: the zone-specific latent clusters persist, even as their alignment with the clean-input clusters weakens. This is the geometric signature

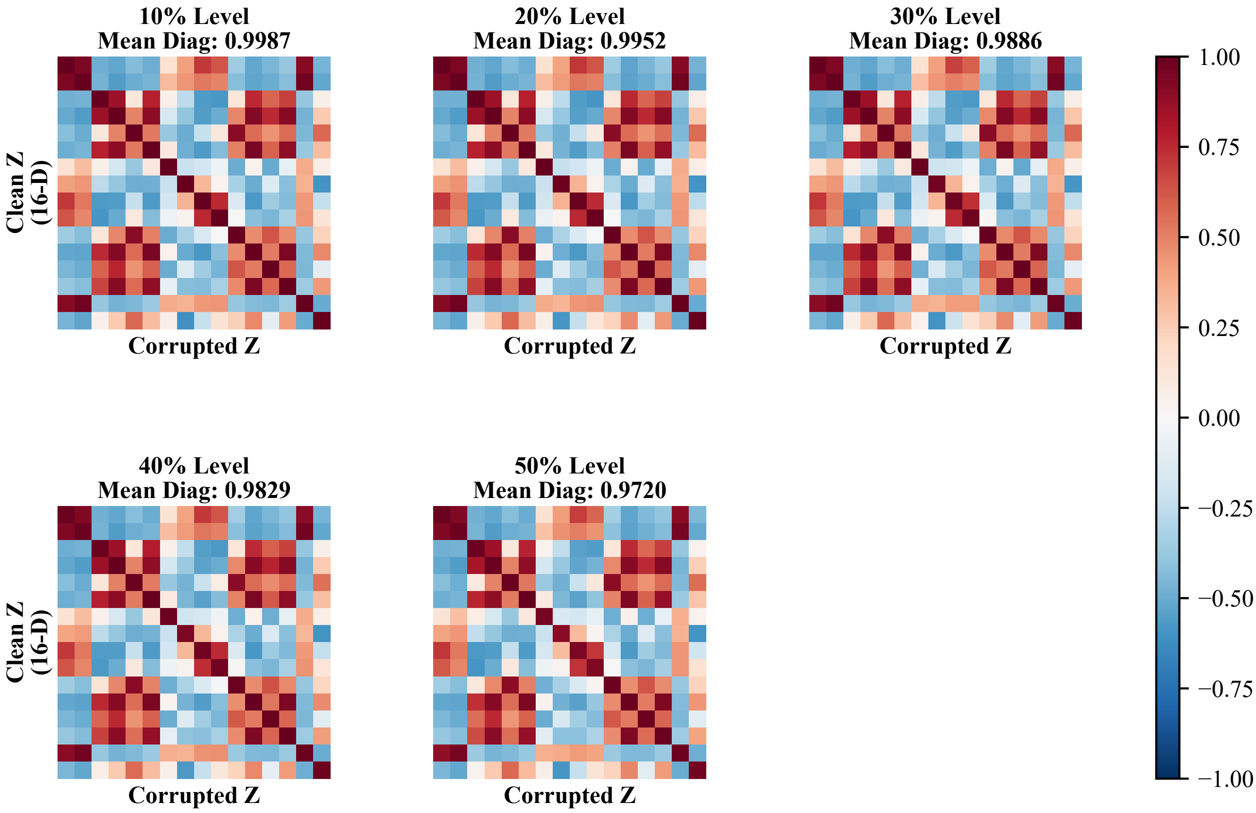

Figure V.9: Latent space cross-correlation between clean and Gaussian-noise-corrupted encodings (test set, $N = 405$). Each panel shows the 16×16 correlation matrix at a different noise level. Mean diagonal values above 0.97 across all five panels confirm that the Encoder's bottleneck is effectively unreachable by zero-mean stochastic perturbations, regardless of their amplitude. The preserved block structure indicates that the semantic organisation of the latent space, three zone-specific damage clusters and a global stiffness mode, is intact even under the most aggressive noise tested.

of graceful degradation: the model loses precision but retains the semantic organisation of the latent space.

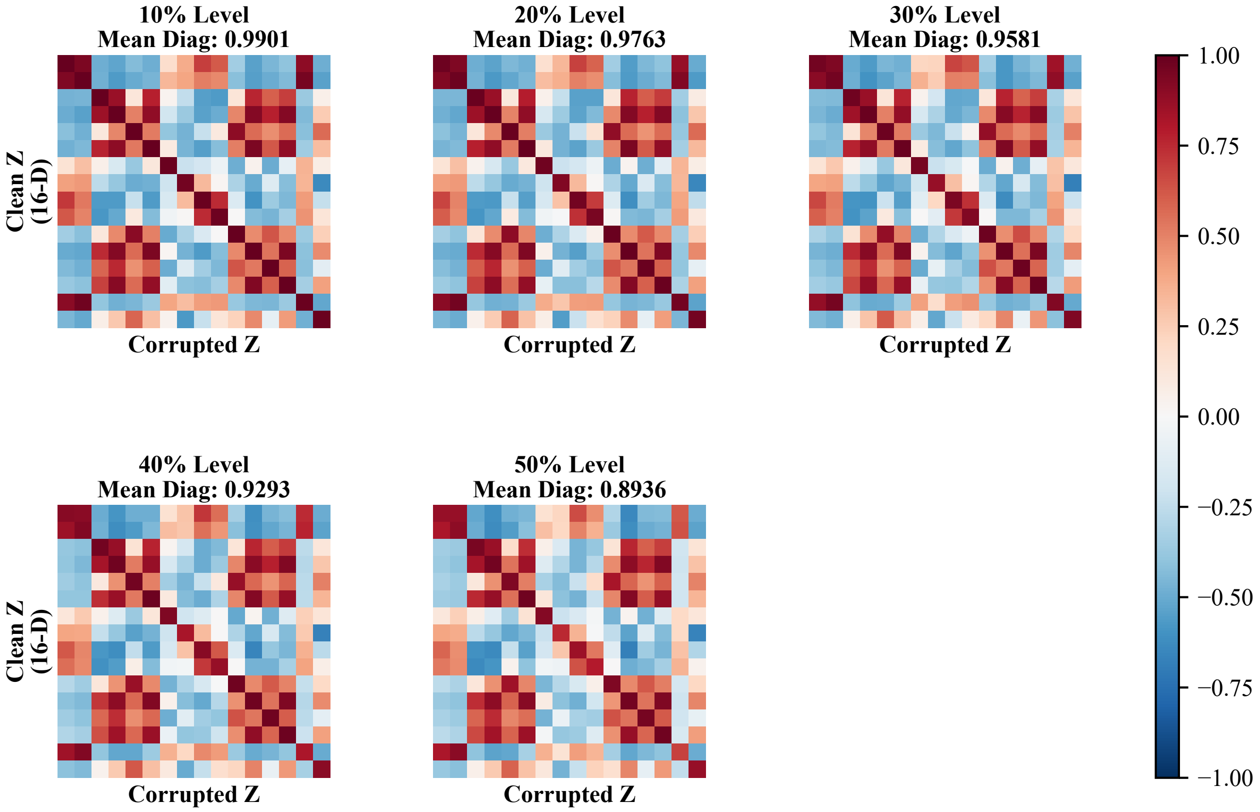

Figure V.10: Latent space cross-correlation between clean and sensor-dropout-corrupted encodings (test set, $N = 405$). Each panel shows the 16×16 correlation matrix at a different dropout level. The monotonic decrease in Mean Diag. from 0.9901 to 0.8936 reflects the irreversible loss of spatial correlation information as sensor channels are removed. The persistent block structure indicates that latent cluster organisation is maintained despite missing sensors, confirming graceful rather than catastrophic degradation.

Together, Figures V.9 and V.10 provide the empirical confirmation of the pseudo-transfer mechanism introduced in Section 5.3.2: under the sensor sub-configurations that govern realistic Type-B deployment (up to 20% sensor loss), the latent code of a sparsely instrumented structure is nearly indistinguishable from that of a fully instrumented one. The Predictor, trained on clean latent codes, therefore operates on effectively equivalent inputs when deployed across the population, without retraining, without domain adaptation, and without any architectural modification.

5.6.4 Operational Implications

The robustness results support three practical conclusions for PBSHM deployment.

Sensor availability is the critical failure mode. The model degrades approximately five times faster under sensor dropout than under equivalent levels of Gaussian noise ($\Delta R^2 = 0.280$ versus 0.050 across the 0%–50% range). For deployment planning, this implies that ensuring sensor *availability*, minimising failure rates through redundancy and maintenance, is substantially more important than improving signal conditioning quality. Sensor placement optimisation in future iterations should therefore weight reliability as a primary objective alongside modal observability.

A practical instrumentation threshold exists. The R^2 curve under sensor dropout exhibits an inflection between 20% and 30% dropout. Below 20% sensor loss, performance degrades slowly and the latent space remains highly stable (Mean Diag. ≥ 0.97). Above 30%, degradation accelerates markedly. This defines a concrete operational guideline: a Type-B structure instrumented with at least 70% of the reference sensor count can be expected to receive reliable damage severity estimates without retraining. Structures with fewer than 14 active channels from the 20-sensor reference grid should be flagged for human review.

Latent stability as an online confidence signal. The monotonic decrease in Mean Diag. across both perturbation axes provides a computationally cheap, model-internal early-warning signal. A deployed system could compute the cross-correlation between the current latent code z and a library of clean reference codes obtained from a commissioning survey, and issue a confidence flag whenever the mean diagonal falls below a threshold, 0.93, corresponding to approximately 30% dropout or 50% noise, is a natural choice from the sweep data. This self-assessment capability is available at zero additional cost from the existing latent representation and offers a principled path toward uncertainty-aware SHM without requiring explicit probabilistic modelling of the measurement process.

GENERAL CONCLUSION

This thesis set out to answer a single practical question: can the structural health of an entire network of standardised reinforced concrete buildings be monitored reliably from a minimal, economically viable instrumentation setup, without calibrating a dedicated diagnostic model to each individual structure? The answer developed across four chapters is affirmative, and the argument rests on a chain of decisions that are worth tracing in full.

The starting point was the seismic context of northern Algeria, where mass housing programmes have produced dense residential districts composed of hundreds of nominally identical G+9 shear-wall buildings, all exposed to the same tectonic hazard and all potentially requiring rapid post-earthquake assessment. The fundamental insight that shapes the entire pipeline is that this very uniformity, normally seen as an administrative convenience rather than a scientific resource, is precisely what Population-Based SHM is designed to exploit. Because the buildings within a given estate share the same structural system, geometry, and design code, the variability that distinguishes one from another arises from many independent sources simultaneously: batch-to-batch scatter in concrete strength, construction tolerances, differential settlements, seasonal temperature gradients, and local soil conditions. The Central Limit Theorem guarantees that the combined effect of these sources on the extracted modal features converges to additive Gaussian noise around the baseline Form. This transforms what might otherwise be an uncontrolled source of epistemic uncertainty into a formally tractable modelling assumption, and it is the justification on which the entire machine learning strategy is built.

Chapter 3 established the baseline structural model. The G+9 building in Staoueli, designed to RPA 2024 and BAEL 91/99, was classified as plan and elevation irregular, assigned a shear-wall behaviour coefficient of $R = 4.5$, and verified against seismic base shear, inter-story drift, and P-Δ stability requirements. The critical slab and beam elements were designed through full limit-state calculations, providing a structurally credible reference model from which all subsequent damage simulations are derived. This grounding in Algerian design practice is not incidental; it ensures that the damage scenarios generated in Chapter 4 are physically realistic representations of the degradation modes that seismic loading would actually produce in this structural typology.

Chapter 4 addressed the instrumentation problem. A Genetic Algorithm guided by the Modal Assurance Criterion identified a sparse but informationally optimal network of 20 tri-axial sensors from a pool distributed across the ten storey levels. The three critical damage zones, the central U-core and the two perimeter corners, were selected on the basis of their dominant contribution to lateral resistance (76.6% of total base shear under the governing seismic case), ensuring that any simulated stiffness degradation produces a globally detectable signal rather than a locally masked one. The maximum column-wise flexibility change $\Delta F_{\max}$ was then established as the damage-sensitive feature vector, a 60-dimensional quantity that combines the interpretability of flexibility-based indicators with the practicality of sparse OMA-compatible measurements. Four modes were shown to be sufficient for a converged flexibility estimate, reducing the per-scenario computation time to 78.6 seconds and making the 5 000-scenario dataset generation feasible.

Chapter 5 developed and validated the AI pipeline. The Denoising Autoencoder was presented not as a data-processing convenience but as the architectural translation of the PBSHM insight: because inter-structure variability manifests as additive Gaussian noise in the feature space, a network trained under aggressive noise injection and stochastic sensor masking is forced to learn a latent code that represents the damage state of the structure independently of which building in the population it is observing and independently of how many sensors remain active. The Phase-1 grid search over 720 configurations confirmed that the optimal pre-training operating point is a dropout rate of 20% combined with a noise level of 0.5 standard deviations, the configuration that maximally challenges the Encoder without destroying the essential structural signal. These two parameters are not independent choices: the 20% dropout defines the sensor redundancy budget below which the spatial correlator begins to fail, and the 0.5 noise level defines the population spread over which the system is designed to generalise.

Phase-2 joint optimisation, with the asymmetric 0.9/0.1 prediction-to-reconstruction loss weighting, fine-tuned the entire system toward damage severity estimation while preserving the spatial-correlator behaviour established in Phase-1. The held-out test set of 750 unseen scenarios yielded R^2 values of 0.952, 0.960, and 0.935 for the U-core, back-right corner, and top-left corner zones respectively, confirming strong generalisation across the full severity range.

The robustness evaluation then asked the decisive question for deployment: how does the system behave when conditions in the field deviate from the clean training environment? The answer reveals an important asymmetry. Under test-time Gaussian noise, the operational surrogate for inter-structure variability, the R^2 degrades from 0.942 to 0.892 across the full 0%–50% noise range, a total loss of 0.050 that falls within the bounds of run-to-run variance at low perturbation levels. The latent space cross-correlation analysis explains why: zero-mean stochastic noise averages out across the 60 input channels as the signal propagates through the Encoder's dense layers, leaving the 16-dimensional bottleneck effectively unreachable by amplitude perturbations up to half the signal's own standard deviation. The semantic cluster organisation of the latent space, three zone-specific damage subspaces and a global stiffness mode, is intact even at the most aggressive noise level tested. Under sensor dropout, the picture is different but still controlled: the R^2 falls more steeply, reaching 0.662 at 50% dropout, but the variance across 20 independent runs remains low at every level, confirming graceful rather than catastrophic degradation. The practical implication is that a Type-B building instrumented with at least 70% of the 20-sensor reference network can be diagnosed reliably without retraining; below 14 active channels, a human review flag is warranted.

Taken together, these results validate the core scientific contribution of this thesis: the explicit and measurable link between the statistical structure of a strongly-homogeneous building population and the training mechanics of a Denoising Autoencoder. The latent space learned from a single baseline finite element model, perturbed by noise calibrated to the population's variability spread, generalises to other members of the population without domain adaptation, without auxiliary labels, and without retraining. The pseudo-transfer mechanism is not an approximation or a heuristic; it is the direct consequence of training the Encoder to be representation-robust in the first place, and the cross-correlation matrices of Chapter 5 demonstrate it geometrically.

Several limitations remain and define the natural path forward. The 5 000-scenario dataset, while sufficient for the present validation, was generated from a single deterministic finite element model; extending the pipeline to a stochastic ensemble of models that explicitly samples the population's material and geometric scatter would close the loop between the CLT assumption and the training data. The damage model, based on uniform Young's modulus reduction within macro-assemblies, is a first-order approximation of the nonlinear, hysteretic degradation that reinforced concrete elements actually undergo under cyclic seismic loading; higher fidelity damage models would sharpen the feature extraction. The sensor placement optimisation currently weights modal observability exclusively; incorporating sensor reliability as an objective, motivated directly by the finding that dropout is the dominant failure mode, would produce networks that are more robust by design rather than by training. Finally, deploying the system on real ambient vibration data from an existing AADL estate would constitute the most meaningful validation, one that neither a laboratory experiment nor a simulation study can fully replace.

What the present work has established is the theoretical and computational framework within which that deployment becomes principled rather than speculative. The Algerian mass housing estate, long regarded as a logistical challenge for post-earthquake assessment, emerges here as a genuinely favourable environment for population-based monitoring: its uniformity is a resource, its variability is quantifiable, and its scale is precisely the regime in which a shared latent representation pays its greatest dividend.

6 BIBLIOGRAPHY

[1] Luiz Tadeu, Rafaelle Finotti, Flávio De, and Alexandre Cury. "The Trajectory of Data-Driven Structural Health Monitoring: A Review from Traditional Methods to Deep Learning and Future Trends for Civil Infrastructures". In: *Computer Modeling in Engineering & Sciences* 146.2 (2026). ISSN: 1526-1492, 1526-1506. DOI: 10.32604/cmes.2026.075433.

[2] Tarutal Ghosh Mondal and Genda Chen. "Artificial Intelligence in Civil Infrastructure Health Monitoring—Historical Perspectives, Current Trends, and Future Visions". In: *Frontiers in Built Environment* 8 (Sept. 2022). ISSN: 2297-3362. DOI: 10.3389/fbuil.2022.1007886.

[3] John J. Moughty and Joan R. Casas. "A State of the Art Review of Modal-Based Damage Detection in Bridges: Development, Challenges, and Solutions". In: *Applied Sciences* 7.5 (May 2017), p. 510. ISSN: 2076-3417. DOI: 10.3390/app7050510.

[4] Ahmet Can Altunışık, Fatih Yesevi Okur, Sebahat Karaca, and Volkan Kahya. "Vibration-Based Damage Detection in Beam Structures with Multiple Cracks: Modal Curvature vs. Modal Flexibility Methods". In: *Nondestructive Testing and Evaluation* 34.1 (Jan. 2019), pp. 33–53. ISSN: 1058-9759. DOI: 10.1080/10589759.2018.1518445.

[5] A. K. Pandey and M. Biswas. "Damage Detection in Structures Using Changes in Flexibility". In: *Journal of Sound and Vibration* 169.1 (Jan. 1994), pp. 3–17. ISSN: 0022-460X. DOI: 10.1006/jsvi.1994.1002.

[6] Federico Ponsi, Elisa Bassoli, and Loris Vincenzi. "Mitigation of Model Error Effects in Neural Network-Based Structural Damage Detection". In: *Frontiers in Built Environment* 8 (Jan. 2023). ISSN: 2297-3362. DOI: 10.3389/fbuil.2022.1109995.

[7] Jing Li, Baisheng Wu, Q. C. Zeng, and C. W. Lim. "A Generalized Flexibility Matrix Based Approach for Structural Damage Detection". In: *Journal of Sound and Vibration* 329.22 (Oct. 2010), pp. 4583–4587. ISSN: 0022-460X. DOI: 10.1016/j.jsv.2010.05.024.

[8] Xi Peng, Qiuwei Yang, Fengjiang Qin, and Binxiang Sun. "Structural Damage Detection Based on Static and Dynamic Flexibility: A Review and Comparative Study". In: *Coatings* 14.1 (Jan. 2024), p. 31. ISSN: 2079-6412. DOI: 10.3390/coatings14010031.

[9] Minkyu Kim and Junho Song. "Near-Real-Time Identification of Seismic Damage Using Unsupervised Deep Neural Network". In: *Journal of Engineering Mechanics* 148.3 (Mar. 2022), p. 04022006. DOI: 10.1061/(ASCE)EM.1943-7889.0002066.

[10] Zhiyan Sun et al. "Optimal Sensor Placement for Structural Health Monitoring: A Comprehensive Review". In: *Journal of Sensor and Actuator Networks* 14.2 (Apr. 2025), p. 22. ISSN: 2224-2708. DOI: 10.3390/jsan14020022.

[11] Djamila Cherid, Nouredine Bourahla, Mohamed Said Laghoub, and Anis Mohabeddine. "Sensor Number and Placement Optimization for Detection and Localization of Damage in a Suspension Bridge Using a Hybrid ANN-PCA Reduced FRF Method". In: *International Journal of Structural Integrity* 13.1 (Oct. 2021), pp. 133–149. ISSN: 1757-9864. DOI: 10.1108/IJSI-07-2021-0075.

[12] Sahar Hassani and Ulrike Dackermann. "A Systematic Review of Optimization Algorithms for Structural Health Monitoring and Optimal Sensor Placement". In: *Sensors* 23.6 (Jan. 2023), p. 3293. ISSN: 1424-8220. DOI: 10.3390/s23063293.

[13] Estefanía Chaves, Alberto Barontini, Nuno Mendes, Víctor Compán, and Paulo B. Lourenço. "Methodologies and Challenges for Optimal Sensor Placement in Historical Masonry Buildings". In: *Sensors (Basel, Switzerland)* 23.23 (Nov. 2023), p. 9304. ISSN: 1424-8220. DOI: 10.3390/s23239304.

[14] Marc Lizana Vilaseca and Joan Ramon Casas Rius. "Optimal Sensor Placement Methods and Criteria in Dynamic Testing: Comparison and Implementation on a Pedestrian Bridge". In: *Proceedings of the International Conference on Structural Health Monitoring of Intelligent Infrastructure. Advanced Research and Real-World Applications. SHMII-10, Porto, Portugal, 30 June-2 July 2021*. 2021, pp. 1065–1072. HDL: 2117/365903.

[15] Ting-Hua Yi, Hong-Nan Li, and Ming Gu. "Optimal Sensor Placement for Structural Health Monitoring Based on Multiple Optimization Strategies". In: *The Structural Design of Tall and Special Buildings* 20.7 (2011), pp. 881–900. ISSN: 1541-7808. DOI: 10.1002/tal.712.

[16] Wei Liu, Wei-cheng Gao, Yi Sun, and Min-jian Xu. "Optimal Sensor Placement for Spatial Lattice Structure Based on Genetic Algorithms". In: *Journal of Sound and Vibration* 317.1 (Oct. 2008), pp. 175–189. ISSN: 0022-460X. DOI: 10.1016/j.jsv.2008.03.026.

[17] Austin Downey, Chao Hu, and Simon Laflamme. "Optimal Sensor Placement within a Hybrid Dense Sensor Network Using an Adaptive Genetic Algorithm with Learning Gene Pool". In: *Structural Health Monitoring* 17.3 (May 2018), pp. 450–460. ISSN: 1475-9217. DOI: 10.1177/1475921717702537.

[18] B. K. Jung, J. R. Cho, and W. B. Jeong. "Sensor Placement Optimization for Structural Modal Identification of Flexible Structures Using Genetic Algorithm". In: *Journal of Mechanical Science and Technology* 29.7 (July 2015), pp. 2775–2783. ISSN: 1976-3824. DOI: 10.1007/s12206-015-0606-z.

[19] Dana Nasr, Reina El Dahr, Joseph Assaad, and Jamal Khatib. "Comparative Analysis between Genetic Algorithm and Simulated Annealing-Based Frameworks for Optimal Sensor Placement and Structural Health Monitoring Purposes". In: *Buildings* 12.9 (Sept. 2022), p. 1383. ISSN: 2075-5309. DOI: 10.3390/buildings12091383.

[20] Vagelis Plevris and George Papazafeiropoulos. "AI in Structural Health Monitoring for Infrastructure Maintenance and Safety". In: *Infrastructures* 9.12 (Dec. 2024), p. 225. ISSN: 2412-3811. DOI: 10.3390/infrastructures9120225.

[21] Shams Forruque Ahmed et al. "Unveiling the Frontiers of Deep Learning: Innovations Shaping Diverse Domains". In: *Applied Intelligence* 55.7 (Mar. 2025), p. 573. ISSN: 1573-7497. DOI: 10.1007/s10489-025-06259-x.

[22] Jack Poole. "Transfer Learning for Population-Based SHM". PhD thesis. University of Sheffield, May 2025.

[23] J. Poole et al. "Active Transfer Learning for Structural Health Monitoring". In: *Mechanical Systems and Signal Processing* 241 (Dec. 2025), p. 113260. ISSN: 0888-3270. DOI: 10.1016/j.ymssp.2025.113260.

[24] L.A. Bull et al. "Foundations of Population-Based SHM, Part I: Homogeneous Populations and Forms". In: *Mechanical Systems and Signal Processing* 148 (Feb. 2021), p. 107141. ISSN: 08883270. DOI: 10.1016/j.ymssp.2020.107141.

[25] J. Gosliga, P. A. Gardner, L. A. Bull, N. Dervilis, and K. Worden. "Foundations of Population-Based SHM, Part II : Heterogeneous Populations – Graphs, Networks, and Communities". In: *Mechanical Systems and Signal Processing* 148 (Feb. 2021). ISSN: 0888-3270. DOI: 10.1016/j.ymssp.2020.107144.

[26] P. Gardner, L. A. Bull, J. Gosliga, N. Dervilis, and K. Worden. "Foundations of Population-Based SHM, Part III: Heterogeneous Populations – Mapping and Transfer". In: *Mechanical Systems and Signal Processing* 149 (Feb. 2021), p. 107142. ISSN: 0888-3270. DOI: 10.1016/j.ymssp.2020.107142.

[27] G. Tsialiamanis et al. "Foundations of Population-Based SHM, Part IV: The Geometry of Spaces of Structures and Their Feature Spaces". In: *Mechanical Systems and Signal Processing* 157 (Aug. 2021), p. 107692. ISSN: 0888-3270. DOI: 10.1016/j.ymssp.2021.107692.

[28] Daniel S. Brennan, Julian Gosliga, Elizabeth J. Cross, and Keith Worden. "Foundations of Population-Based SHM, Part V: Network, Framework and Database". In: *Mechanical Systems and Signal Processing* 223 (Jan. 2025), p. 111602. ISSN: 0888-3270. DOI: 10.1016/j.ymssp.2024.111602.

[29] Marcus Omori Yano, Eloi Figueiredo, Samuel da Silva, Alexandre Cury, and Ionut Moldovan. "Transfer Learning for Structural Health Monitoring in Bridges That Underwent Retrofitting". In: *Buildings* 13.9 (Sept. 2023), p. 2323. ISSN: 2075-5309. DOI: 10.3390/buildings13092323.

[30] P. A. Gardner, L. A. Bull, N. Dervilis, and K. Worden. "On the Application of Heterogeneous Transfer Learning to Population-Based Structural Health Monitoring". In: *Data Science in Engineering, Volume 9*. River Publishers, 2022.

[31] Tina A. Dardeno, Lawrence A. Bull, Nikolaos Dervilis, and Keith Worden. "Transfer Learning via Intermediate Structures". In: *e-Journal of Nondestructive Testing* 29.07 (July 2024). DOI: 10.58286/29727.

[32] Daniel S. Brennan, Julian Gosliga, Paul Gardner, Robin S. Mills, and Keith Worden. "On the Application of Population-Based Structural Health Monitoring in Aerospace Engineering". In: *Frontiers in Robotics and AI* 9 (Nov. 2022). ISSN: 2296-9144. DOI: 10.3389/frobt.2022.840058.

[33] G. Tsialiamanis et al. "On an Application of Graph Neural Networks in Population-Based SHM". In: *Data Science in Engineering, Volume 9*. River Publishers, 2022.

[34] Centre National du Génie Parasismique (CGS). *Règlement Parasismique Algérien RPA 2024*. Alger, Algérie, 2024.

[35] Anil K. Chopra. *Dynamics of structures: theory and applications to earthquake engineering*. Fifth edition in SI units, global edition. Prentice-Hall international series in civil engineering and engineering mechanics. Harlow: Pearson, 2020. 960 pp. ISBN: 978-1-292-24918-6.

[36] Mario Paz and Young Hoon Kim. *Structural dynamics: theory and computation*. Sixth edition. Cham: Springer, 2019. 634 pp. ISBN: 978-3-319-94742-6.

[37] Pankaj K. Agarwal and Manish Shrikhande. *Earthquake resistant design of structures*. 5. Pr. New Delhi: Prentice-Hall of India Pvt. Ltd, 2008. 660 pp. ISBN: 978-81-203-2892-1.